The Impact of Chalcogenide Ligands on the Photoexcited States of Cadmium Chalcogenide Quantum Dots

by

Kyle J. Schnitzenbaumer

B.S., Illinois Wesleyan University, 2007

A thesis submitted to the

Faculty of the Graduate School of the

University of Colorado in partial fulfillment

of the requirement for the degree of

Doctor of Philosophy

Department of Chemistry & Biochemistry

2015

ProQuest LLC.
789 East Eisenhower Parkway
P.O. Box 1346
Ann Arbor, MI 48106 - 1346

This thesis entitled:
The Impact of Chalcogenide Ligands on the Photoexcited States of Cadmium Chalcogenide Quantum Dots
written by Kyle J. Schnitzenbaumer
has been approved for the Department of Chemistry & Biochemistry

_____
(Gordana Dukovic)

_____
(David M. Jonas)

Date _____

The final copy of this thesis has been examined by the signatories, and we
Find that both the content and the form meet acceptable presentation standards
Of scholarly work in the above mentioned discipline.

Schnitzenbaumer, Kyle J. (Ph.D., Chemistry)

The Impact of Chalcogenide Ligands on the Photoexcited States of Cadmium Chalcogenide Quantum Dots

Thesis directed by Assistant Professor Gordana Dukovic

Quantum dots (QDs) are the foundation of many optoelectronic devices because their optical and electronic properties are synthetically tunable. The inherent connection between synthetically controllable physical parameters, such as size, shape, and surface chemistry, and QD electronic properties provides flexibility in manipulating excited states. The properties of the ligands that passivate the QD surface and provide such synthetic control, however, are quite different from those that are beneficial for use in optoelectronic devices. In these applications, ligands that promote charge transfer are desired. To this end, significant research efforts have focused on post-synthetic ligand exchange to shorter, more conductive ligand species. Surface ligand identity, however, is a physical parameter intimately tied to QD excited state behavior in addition to charge transfer. A particularly interesting group of ligands, due to the extraordinarily thin ligand shell they create around the QD, are the chalcogenides S^{2-}, Se^{2-}, and Te^{2-}. While promising, little is known about how these chalcogenide ligands affect QD photoexcited states. This dissertation focuses on the impact of chalcogenide ligands on the excited state dynamics of cadmium chalcogenide QDs and associated implications for charge transfer. This is accomplished through a combination of theoretical (Chapters 2, 3, and 6) and experimental (Chapters 2, 4, 5 and 6) methods. We establish a theoretical foundation for describing chalcogenide capped QD photoexcited states and measure the dynamics of these excited states using transient absorption spectroscopy. The presented results highlight the drastic effects surface modification can have on QD photoexcited state dynamics and provide insights for more informed design of optoelectronic systems.

Acknowledgements

> "It is true that those we meet can change us, sometimes so profoundly that we are not the same afterwards."
>
> - Yann Martel, Life of Pi

Among those to whom I owe a great deal of thanks are:

- My advisor, Gordana Dukovic, for encouraging me to pursue my intellectual curiosities.
- The members of the Dukovic group, past and present, for providing a supportive and collaborative environment in which to work, especially Bryan Tienes, Amanda Grennell, Katherine Shinopoulos, David Garfield, Kyureon Lee, Tais Labrador, Hayden Hamby, James Utterback, Orion Pearce, Kim See, Farrah Qureshi, Mike Martin, Russell Perkins, Sophie Green, Yinggang Lu, and Chi-Hung Chuang.
- My lab mate for the past six years, Molly Wilker, for being a better friend and coworker than I could have ever asked for.
- The collaborators I have had the pleasure of working with and learning from, especially Dan Hickstein, Jennifer Ellis, Wei Xiong, and Margaret Murnane.
- The professors who graciously agreed to serve on my dissertation committee, David Jonas, Henry Kapteyn, Veronica Bierbaum, and Robert Parson.
- Those in the Chemistry Department who have helped keep everyday operations running smoothly, including Marshall Wilkinson, Nate Campbell, Susan Hendrickson, Lauryl Hyde Boni, Lora Ruffin, and Alan Foster.
- My parents, Bernadette and George, for encouraging me to learn about the world around me and fostering the independence necessary for me to do so.
- My partner in all things, Jamie Snyder, for her love and support.

- The friends with whom I have had the joy of sharing a home, especially Russell Muren, Paul Donohoo-Vallett, Pearl Donohoo-Vallett, and Natalie Koster.
- Those I have shared some portion of my graduate school experience with, for serving as friends, colleagues, and mentors, especially Austin Spencer, Jasen Stephany, Paul Teichen, Joe Ostrowski, Nick Demarais, Josh Hewitt, Dmitry Baranov, and Jen Gifford.
- The friends who have made the recreational pursuits of soccer, poker, softball, broomball, and exploring the mountains so rewarding, especially Sam Spencer, Sarah Stephany, Rick Grahn, Jenny Erwin, Luke Erickson, Brian Wiesenauer, Mark Moran, and Laura Johnson.
- The educators and mentors from whom I learned how to learn and learned how to teach, especially Denis Kazelas, Owen Glennon, Randall Coe, Tim Rettich, Stephen Hoffmann, Jim House, Kathy House, Gabe Spalding, Dewayne Lawson, Bridget Trogden, Manning Weir, and Luke Harrington.
- My students, past, present, and future, for the privilege of learning alongside you.

Table of Contents

Tables

Figures

Copyright

"Normal science consists in the actualization of that promise … by increasing the extent of the match between those facts and the paradigm's predictions, and by further articulation of the paradigm itself. Few people who are not actually practitioners of a mature science realize how much mop-up work of this sort a paradigm leaves to be done or quite how fascinating such work can prove in the execution. And these points need to be understood. Mopping-up operations are what engage most scientists throughout their careers."

- Thomas Kuhn

Chapter 1. Introduction

> "I do not know what I may appear to the world; but to myself I seem to have been only like a boy playing on the seashore, and diverting myself in now and then finding of a smoother pebble or a prettier shell than ordinary, whilst the great ocean of truth lay all undiscovered before me."
>
> - Sir Isaac Newton

1.1 Motivation

1.1.1 Solar energy harvesting

The entirety of the research discussed in this dissertation is motivated by the emergence of solar energy as a potential means of providing the world with renewable energy. Anthropogenic climate change is largely driven by greenhouse gas emissions, and renewable energy sources provide the promise of energy free of greenhouse gas emission.[1] The sun's capacity to provide renewable, clean energy completely dwarfs that of all other options, including nuclear, wind, hydroelectric, and biofuel. More energy strikes the Earth in the form of sunlight in an hour than the entire world consumes in a year.[2] The potential for abundant, renewable energy is quite literally raining down on us every day. Efforts to harness this immense amount of energy are both wide-ranging and incredibly interdisciplinary. This dissertation represents my contributions towards developing a more efficient means of harvesting solar energy.

1.1.2 Photochemistry vs. photophysics

Major research efforts focus on the development of photovoltaic and photocatalytic

systems.[3-8] While photovoltaics convert solar energy directly into electricity, photocatalytic systems convert solar energy into stored, potential energy by driving otherwise energetically unfavorable reactions. The products of these reactions, like the elemental hydrogen and oxygen obtained from a water splitting reaction, can then be utilized for their stored chemical energy. The gamut of photovoltaic and photocatalytic systems is immensely varied and incredibly complex. Each individual system contains a multitude of components that must work in concert together, but each system relies upon the same initial steps. Any successful photovoltaic or photocatalytic process begins with (i) the absorption of a photon by a material to generate a photoexcited state and (ii) the subsequent transfer of a photogenerated charge carrier out of that material.

The efficiencies of these two processes, being the initial steps of the overall process, play a critical role in determining the efficiency of the system as a whole. Thus the overall device quantum efficiency, QE, will be dictated in part by the fraction of incident light absorbed (I_{abs}/I_0) and the efficiency of the initial charge transfer event (QE_{et}). Because QE is essentially the product of the efficiencies of each step, the efficiency of these two steps provides a maximum ceiling for what successive steps can hope to achieve. For any system to be used in photovoltaic or photochemical applications, strong light absorption and efficient charge transfer characteristics are necessary. As will be discussed in the next section, the cadmium chalcogenide materials this dissertation focuses on are incredibly efficient light absorbers. One of the central goals of systems utilizing these materials then is to increase the quantum efficiency of charge transfer.

In these systems, the charge transfer event provides the carrier that ultimately contributes to an electrical circuit or photochemical redox reaction. For this reason we refer to charge transfer as a photochemical process. Eqn. 1.1 frames the quantum efficiency of electron transfer, QE_{et}, in terms of the rate constant of electron transfer, k_{et}. QE_{et} depends on the comparison of the rate of electron transfer with the total decay rate of the excited state. The photoexcited state can decay either

through the desired photochemical pathway, k_{et}, or through any number of alternative pathways. These intrinsic decay channels, whose rate we denote k_{QD}, exist even in the absence of charge transfer, and we therefore refer to them as photophysical processes.

$$QE_{et} = \frac{k_{et}}{k_{et} + k_{QD}} \qquad \text{Eqn. 1.1}$$

One obvious method for promoting efficient charge transfer is increasing the rate of electron transfer, k_{et}. Equally important to QE_{et}, however, is the rate at which the system's photoexcited state decays, k_{QD}. Figure 1.1 plots QE_{et} as a function of the ratio k_{et}/k_{QD} along a logarithmic axis. When the electron transfer rate is equal to the intrinsic decay rate (k_{et}/k_{QD} =1), QE_{et}=0.5. A ten-fold increase in either rate over the other leads to a QE_{et} of either 10% or 90%, a notably drastic effect. Because QE_{et} is dictated by the *interplay* between k_{et} and k_{QD}, it is desirable to ultimately characterize *both* the photochemistry and photophysics of a system.

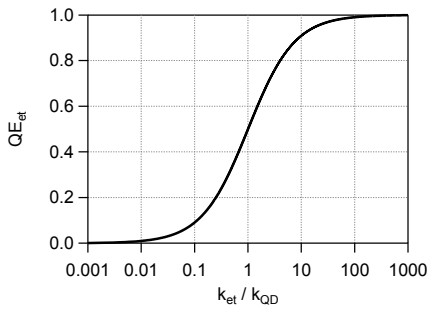

Figure 1.1: Interplay between k_{et} and k_{QD}. Quantum efficiency of electron transfer (QE_{et}) as a function of the ratio between the rate of electron transfer, k_{et}, and the intrinsic excited state decay rate, k_{QD}. Note that the x-axis is plotted on a logarithmic scale. Just as increasing k_{et} leads to a higher QE_{et}, so too does decreasing k_{QD}. The range of $0.1 < k_{et}/k_{QD} < 10$ accounts for QE_{et} spanning 10% to 90%, demonstrating how relatively minor adjustments to either k_{et} or k_{QD} can have a significant impact on efficiency.

1.2 Background

1.2.1 Nanocrystalline materials

Colloidal semiconductor nanocrystals are extremely small pieces of crystalline material. Typically composed of 1,000 – 10,000 atoms, measuring 1 – 10 nanometers in size, and having well-defined absorption energies, nanocrystals can be considered giant, artificial atoms. The absorption of light by nanocrystals is governed by a unique combination of material properties and size-induced confinement effects. When bulk materials absorb a photon of the correct energy, a pair of charge carriers is formed, a photoexcited electron and the resulting positively charged vacancy, referred to as a hole.[9] These oppositely charged carriers are electrostatically bound to each other and, similarly to the proton and electron in a hydrogen atom, can be characterized by the exciton Bohr radius (a_0), the most probable distance separating the two. When the size of the material is decreased to a_0, the photoexcited carriers begin to exhibit quantum mechanical behavior.[10-11]

The class of materials this dissertation focuses on, cadmium chalcogenide nanocrystals (i.e. CdSe and CdTe), have several characteristics that make them particularly attractive for use in solar energy harvesting applications.[6] They absorb in the visible region, enabling them to utilize a significantly larger portion of the solar spectrum than UV-absorbing materials. As mentioned above, chalcogenide nanocrystals are also very strong light absorbers, with molar absorptivities on the order of $10^5 – 10^7$ M^{-1} cm^{-1}. These values are 10 – 100 times larger than the strongest absorbing molecular dyes. The band edges, redox potentials, and absorption spectra of cadmium chalcogenides are readily tunable using easily controlled synthetic parameters, such as size, shape, and composition. On the nanometer scale, where the size of the nanocrystal largely dictates its light absorption characteristics, photoexcited carriers have facile access to surfaces where they can be utilized.

1.2.2 Quantum dots

The most common example of this unique combination of nanocrystalline properties is the quantum dot (QD), a spherical nanocrystal (Figure 1.2a). Quantum dots exhibit tunable absorption spectra based on their size due to the quantum-confined nature of the photoexcited charge carriers that are generated upon absorption of a photon.[10-11] The size-tunability of these absorption energies allows for tuning one material's absorption spectra simply by changing the size of the nanocrystal, which is a readily controllable synthetic parameter. The size-induced quantum confinement effect that occurs in all spatial dimensions for a quantum dot leads to the photoexcited carriers in band edge states being delocalized over the entire QD rather than being localized on a single atom or cluster of atoms. This is beneficial for many applications as it enables easier extraction of the charge carriers. Unlike bulk semiconductors, carriers in QDs need not diffuse to reach surface states to become available for charge transfer or catalysis.

The optical properties of quantum dots are thus directly related to their physical properties. For quantum dots, whose size is smaller than a_0, the quantum dot size defines the spatial distribution of the exciton. The carriers in a quantum dot can be described as particles in a sphere, a variation on the quantum mechanical particle in a box. Similar to the particle in a box, where a smaller box leads to a larger spacing between energy levels, smaller quantum dots exhibit larger spacing between energy levels. Through this quantum confinement effect, simply changing the size of the QD leads to changes in band gap energy. The ability to tune the optical and electronic properties of quantum dots simply by adjusting their size provides flexibility in manipulating their excited states.[12-13]

For this reason, nanocrystals hold immense potential for use in solar energy harvesting applications. Colloidal nanocrystals, and quantum dots in particular, have been employed in a wide variety of photovoltaic and photocatalytic systems.[3-8, 14-16] Quantum dot based solar cells have been the focus of extensive research with great success to date and the potential to overcome the

theoretical efficiency limit of 31% for single-junction photovoltaics. Quantum dots and other nanocrystals, coupled with a variety of cocatalysts, have also been used to drive photochemical fuel generation such as water splitting and CO_2 reduction.

1.2.3 Nanocrystalline heterostructures

While nanocrystals have been actively researched since the 1980s, there have been remarkable advances in synthetic methods in the last decade. These advances have allowed for the ability to combine multiple materials in one nanostructure.[12, 17-19] These systems, due to the presence of more than one crystalline material while still exhibiting the effects of quantum confinement, are referred to as nanocrystal heterostructures. While a wide variety of heterostructure materials and geometries exist, the most relevant for this dissertation is the core/shell heterostructure, which consists of a QD core surrounded by a spherically symmetric shell of another semiconductor material.

The most promising aspect of heterostructures is the ability to funnel charge carriers into particular regions of the structure. Depending on the desired application, both the electron and hole can be funneled into the same (Type I) or separate (Type II) regions of the heterostructure.[12, 18-19] This is accomplished through the band edge potentials of the materials incorporated in the heterostructure. When the band edges of one material straddle those of the other, the heterostructure demonstrates a Type I band alignment. In this configuration, the minimum energy of both the electron and hole are located in the same region of the heterostructure (Figure 1.2b). When the band edges of the two materials are staggered in a Type II band alignment, the electron and hole localize into separate regions of the heterostructure (Figure 1.2c). The range of geometries and material combinations made possible through the synthesis of nanocrystalline heterostructures further enhances the ability to manipulate photoexcited state behavior.

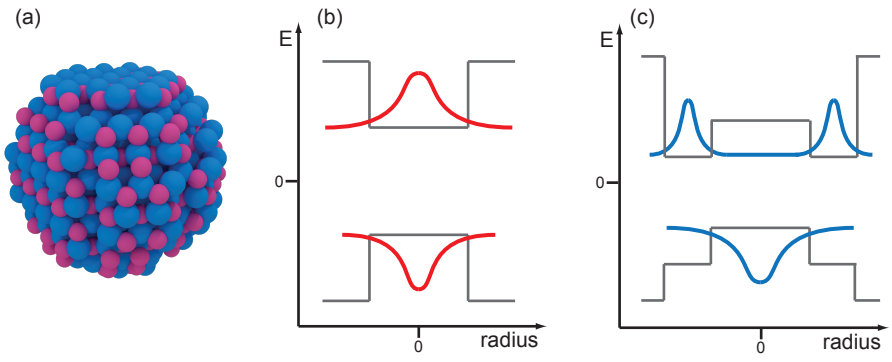

Figure 1.2: Nanocrystalline materials. (a) Illustration of a CdSe quantum dot, a spherical nanocrystal. The purple spheres represent Cd^{2+} ions, and the blue spheres represent Se^{2-} ions. Image courtesy of Daniel D. Hickstein. (b) Schematic of a Type I band alignment, wherein both the electron and hole wave functions (red) are localized in the same region of the nanostructure. (c) Schematic of a Type II band alignment, wherein the electron and hole wave functions (blue) are localized in separate regions of the nanostructure.

1.2.4 Surface capping ligands

Crystalline materials, such as CdSe and CdTe, do not find thermodynamic minima at the nanoscale. Larger, extended structures are more thermodynamically favorable. To prevent crystals from growing into the bulk form, these nanocrystal surfaces are passivated with ligand molecules.[20-21] Ligands bind to exposed cations on the nanocrystal surface in a manner akin to coordination complexes. These ligand molecules play an integral role in quantum dot syntheses by kinetically governing the nanocrystal growth. Both nanocrystal shape and crystal structure can be controlled through the use of different ligand molecules during synthesis.[20-23]

Most relevant for the work discussed in this dissertation, ligands, which comprise the layer between the nanocrystal and its surroundings, dictate a nanocrystal's interactions with its environment.[24-25] These interactions include solubility, and of particular relevance for photovoltaic and photochemical applications, photochemical charge transfer rates between a nanocrystal and its surroundings. Shorter, more electronically conductive ligands have been proven to lead to faster charge transfer rates.[24, 26-33] Other work has demonstrated that nanocrystal surface chemistry, dictated largely by the nanocrystal-ligand interaction, plays a critical role in photophysics as well.[24-25, 34]

Ligands, even though they represent a single layer on the outer edge of a nanocrystal, therefore play a significant and integral role in both charge transfer and photophysics.

1.2.5 Post-synthetic ligand exchange

The role ligands play in colloidal nanocrystal syntheses requires certain molecular characteristics. Ligands typically chosen for synthetic purposes are large, aliphatic molecules with head groups that can act as Lewis bases. The high boiling points that arise from strong dispersion forces allow them to remain in solution at the high temperatures required for crystal growth, the large size of the molecules allows for kinetically mediated crystal growth, and the Lewis basicity promotes ligand-cation interaction. The downside of these ligands is that the very qualities that make them beneficial for synthetic purposes hinder charge transfer. The aliphatic nature of these ligands provide an insulating barrier between the nanocrystal and its environment, and the large size can prevent charge acceptors from getting close to the nanocrystal surface. The native, aliphatic ligands used in this dissertation are n-octadecylphosphonic acid (ODPA) and n-octadecylamine (ODA), whose structures are provided in Figure 1.3.

The characteristics of these aliphatic ligands are drastically different than those desired from a charge transfer standpoint. Here, we desire a decreased barrier between the nanocrystal and its environment, both physically and energetically. To this end, significant research efforts have focused on exchanging large, aliphatic ligands with shorter, more conductive species.[4, 35-48] Many of these ligands have been shown to improve carrier transport in devices.[4, 36-37, 40, 43-44, 47-49] One particularly promising class of ligands are the chalcogenides S^{2-}, Se^{2-}, and Te^{2-}.[40, 50] They are appealing for the extraordinarily thin single atomic layer ligand shell they create around the QD. They are also significantly more conductive than aliphatic carbon chains. Both of these factors lead to increased electronic coupling. Because the large, aliphatic ligands play such a critical role in QD synthesis, it is beneficial to exchange the ligands after crystal growth is completed. These post-synthetic ligand

exchanges are simple solution-phase, room temperature reactions driven by the new ligand's higher affinity for exposed cations on the QD surface than the native ligand.

This dissertation focuses on the impact of chalcogenide ligands on the photophysics and photochemistry of QDs, an important yet largely unknown aspect of this promising family of ligands. In order to isolate the effect of altering the ligand identity, the photophysical behavior they induce must be compared to that of native, aliphatic ligand passivated QDs. Because of the difference in solubility between QD passivated by chalcogenide ligands and the native alkyl-phosphonate and alkyl-amine ligands, comparison with an aliphatic ligand that provides solubility in polar solvents is desired. For this purpose, we also explore the impact of post-synthetic ligand exchange to 3-mercaptopropionic acid (MPA). This ligand is an excellent choice for this comparison due to its ability to solubilize QDs in polar solvents and smaller molecular size while retaining an aliphatic ligand shell around the QD. It thereby serves as an intermediate between the long chain aliphatic ODA and ODPA ligands and the single-atom chalcogenide ligands. The use of MPA-capped nanocrystals in both photovoltaic and photochemical QD systems makes understanding the impact of MPA on charge transfer and photophysics desirable as well.

Figure 1.3 provides a schematic illustration of the different QD-ligand systems investigated throughout this dissertation. To isolate the effect of exchanging n-octadecylphosphonic acid (ODPA) capped CdTe QDs and n-octylamine (ODA) capped CdSe QDs to 3-mercaptopropionic acid (MPA), S^{2-}, Se^{2-}, and Te^{2-} capped QDs, we compare QDs of the same size with the various ligand shells. This point is highlighted in Figure 1.3, where all QDs are the same size, yet the varying ligand identities provide different ligand shell widths. This prevents the convolution of both ligand and QD-size effects. The color scheme used in Figure 1.3 is used throughout this dissertation to differentiate among native, aliphatic (grey), mercapto-carboxylate MPA (black), S^{2-} (red), Se^{2-} (blue), and Te^{2-} (green) ligand identities. Throughout the text, these will be referred to as QD-ODPA, -

ODA, -MPA, -S, -Se, and -Te, respectively.

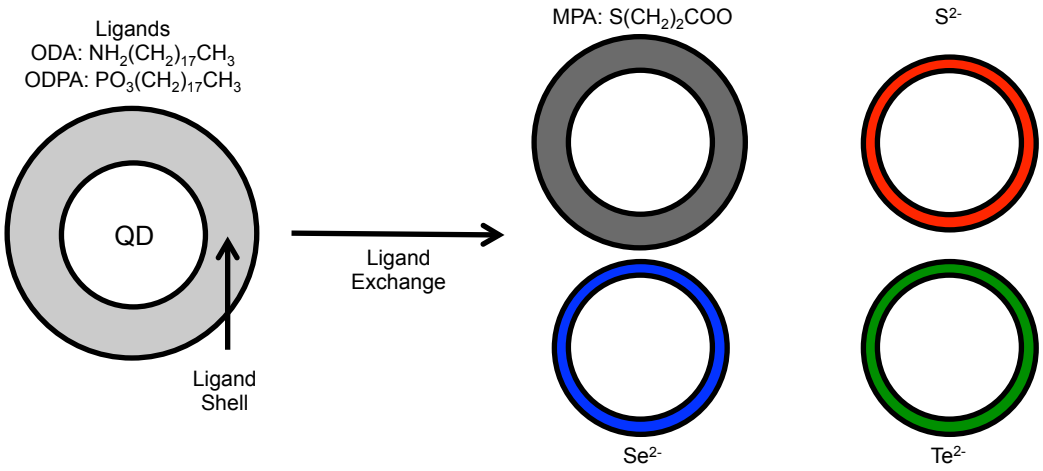

Figure 1.3: Schematic of QD-ligand systems. Native, aliphatic ligands (grey) are exchanged for the mercapto-carboxylic acid ligand MPA (black) and the chalcogenide ligands S^{2-} (red), Se^{2-} (blue), and Te^{2-} (green). The resulting QD-ligand systems are referred to throughout this dissertation as QD-ODPA, -ODA, -MPA, -S, -Se, and -Te. Comparisons among QDs that differ only in ligand identity employ this color-coding.

1.2.6 Ultrafast broadband transient absorption spectroscopy

Transient absorption (TA) spectroscopy is a powerful technique for measuring the dynamics of photophysical and photochemical processes.[6, 24, 34, 51] In this pump-probe technique, a pump pulse of light is used to photoexcite a sample. This pulse is followed some time later by a probe pulse of light that measures pump-induced changes in absorption. Altering the time delay between the pump and probe pulses allows one to monitor the dynamics of the photoexcited state. Since photoexcited states can evolve quickly, ultrafast time resolution is desired. To achieve this, the pump and probe pulses are typically on the order of 100 femtoseconds (10^{-13} s) in duration. This time resolution allows for the monitoring of electron dynamics on a subpicosecond time scale, such as the state-to-state relaxation discussed in Chapter 4 and Chapter 5 and the QD to molecular acceptor electron transfer discussed in Chapter 6.

Rather than probing a sample with a single wavelength of light, a broadband probe can be used and a TA spectrum measured for each value of pump-probe delay. This allows for spectral resolution in addition to kinetic information. To focus on the spectral features due to the excited state, transient absorption is reported as a change in absorption, ΔA, as opposed to the absorption, A, associated with steady state absorption. The measured ΔA effectively subtracts out any contributions to the signal due to the ground state and is therefore indicative of the sample's photoexcited state.

1.3 Summary and Goals

To fully understand the benefits and drawbacks of a particular ligand or family of ligands, their impact on both photochemistry *and* photophysics must be examined. This dissertation broadens our understanding of the impact of chalcogenide ligands on the photophysics of cadmium chalcogenide quantum dots and implications for charge transfer. This is accomplished primarily through two means: (i) establishing a theoretical foundation that applies to chalcogenide ligand passivated QDs and (ii) measuring photophysical rates associated with chalcogenide ligand passivated QDs.

Chapter 2 describes the methods, both theoretical and experimental, used throughout this dissertation to accomplish these objectives. Chapter 3 details the application of the effective mass approximation model to chalcogenide capped CdTe QDs. Through comparison of experimental and calculated results, it is shown that these systems can be treated as core/shell nanoheterostructures. Comparisons between aliphatic and chalcogenide ligand impacts on charge transfer are explored using this model. Chapter 4 focuses on the measurement of chalcogenide ligand capped CdSe QD photophysics using transient absorption spectroscopy. Substantial differences in the photophysical

behavior of aliphatic and chalcogenide capped QDs are observed and discussed. Chapter 5 provides a detailed comparison among the photophysics of CdTe QD, CdTe/CdSe core/shell nanoheterostructures, and Se^{2-} capped CdTe QD. This chapter explores the effect of CdTe QD surface modification, both through the growth of a thin CdSe shell and Se^{2-} ligand exchange. Chapter 6 focuses on two projects from collaborative work with the Kapteyn & Murnane research group. The first highlights the use of the theoretical construct described in Chapter 2 and Chapter 3 to explain experimental observations of CdSe QDs in the gas phase. The second highlights the comparison of charge transfer from CdSe QD in the gas and solution phases, using the spectroscopic techniques outlined in Chapter 2, thereby isolating the role of solvent molecules on the electron transfer process. Chapter 7 provides an overview of the work presented here and suggests avenues of future research.

Chapter 2. Methods

> "Fundamentals. You've got to get the fundamentals down, because otherwise the fancy stuff isn't going to work."
>
> - Randy Pausch

2.1 Summary of Techniques

The work in this dissertation focuses on exploring the impact of ligand identity on the photophysics of cadmium chalcogenide QDs and their implications for charge transfer. Much of this dissertation therefore focuses on particular QD materials, ligand identities, and experimental techniques that are common to multiple chapters. This chapter begins by describing the methods used to synthesize CdTe and CdSe QDs and perform post-synthetic ligand exchange reactions. The techniques, both experimental and theoretical, used to explore the impacts of ligand exchange are also presented in this chapter. Broadly speaking, these techniques can be considered the primary means through which the photochemical and photophysical characteristics of the materials are investigated in the remaining chapters of this dissertation. The measurement of rates, ranging from rates of photoexcited state decay to rates of electron transfer, is performed using broadband probe transient absorption (TA) spectroscopy. This chapter describes our TA setup as well as the experimental conditions employed. The single-band effective mass approximation model used to describe chalcogenide capped QDs is also presented in this chapter.

2.2 Experimental

2.2.1 Quantum dot syntheses

Synthesis of CdTe QDs. Colloidal octadecylphosphonic acid (ODPA) capped CdTe quantum dots with zinc blende crystal structure were synthesized under air-free conditions with minor modifications to previously published procedures.[23, 52] 0.2 mmol of Cadmium Oxide (CdO) and 0.4 mmol ODPA in 5 mL octadecene (ODE) were heated to 100 °C and dried under vacuum. Separately, 0.1 mol of Te was dissolved in 1.0 mL tri-n-octylphosphine (TOP). The CdO/ODE mixture was heated to 280 °C and 1mL of TOP:Te solution was injected. Growth temperatures were maintained at 265 °C. Varying growth times between 2 and 90 min allowed for growth of CdTe QDs with radii ranging from 1.37 to 2.24 nm. Growth was arrested by rapidly cooling the reaction mixture using a mineral oil bath. High quality colloidal dispersions of phosphonic-acid capped CdTe QDs were isolated from the cooled reaction mixture by precipitation with isopropanol. Alternating washes of octylamine and nonanoic acid, with precipitation by methanol and redissolving with toluene, were used until optically clear solutions were obtained.

Synthesis of CdTe/CdSe core/shell QDs. Colloidal CdTe/CdSe core/shell QDs were synthesized using a procedure based on previously published methods.[23, 53-54] A mixture of 0.05 mol CdO, 0.1 mmol ODPA, and 5 mL ODE were heated to 90 °C and degassed under vacuum for 30 min. Following heating at 280 °C for 1 hour to generate the Cd-ODPA precursor, the solution was once again degassed. A solution of 0.05 mmol Te dissolved in 1.0 mL TOP was quickly injected into the Cd-ODPA solution at 280 °C. The CdTe growth was allowed to proceed for 20 minutes at 255 °C. The CdTe reaction mixture was then rapidly cooled to 150 °C using a mineral oil bath, arresting CdTe growth. After removing an aliquot of the CdTe QD cores, a mixture of 0.25 mmol cadmium acetate and 0.25 mmol Se dissolved in 1.0 mmol ODE was injected dropwise to initiate growth of the CdSe shell. The reaction temperature was maintained at 150 °C to prevent homogeneous

nucleation of CdSe. After allowing the reaction to proceed for 6 min, the reaction mixture was cooled, precipitated, and purified in a similar manner to that outlined above for CdTe QDs.

CdSe Quantum Dots. Octadecylamine capped CdSe QDs with radii of 2.8nm were obtained commercially from NN Laboratories. A dilution of this stock solution with toluene was performed to obtain solutions of the appropriate concentrations for further study and ligand exchange reactions.

2.2.2 Post-synthetic ligand exchange

Mercapto-carboxylic acid ligand exchanges were performed based upon literature procedures.[40, 55-57] In order to avoid the complication of oxidative effects, all ligand exchanges were performed in an oxygen- and water-free Ar atmosphere (<20 ppm O_2 and H_2O). 3-Mercaptopropionic acid (MPA) ligand exchanges were performed following a previously described procedure.[55-57] The MPA ligand exchange solution was prepared by dissolving 8.5 mmol MPA in ~18 mL methanol. The pH of the resulting solution was adjusted to 11-12 using tetramethylammonim hydroxide (TMAH) to ensure deprotonation of MPA. Approximately 1mL of this solution was added to a small volume of ODA-capped CdSe QDs in toluene or CdTe-ODPA QDs in hexane or toluene and agitated until the solution was optically clear. The MPA capped QDs, precipitated by addition of toluene and centrifugation, were redissolved in formamide (FA).

Sulfide, selenide, and telluride ligand exchanges were performed following a previously reported procedure.[40] ODA-capped CdSe QDs or CdTe-ODPA QDs in toluene were added to a solution of 0.045 M Na_2X (X = S, Se, Te) in FA. This biphasic mixture was agitated until the toluene layer appeared colorless (~5-10 min), indicating migration of QDs to the polar phase. The CdSe-X or CdTe-X QDs, precipitated by addition of acetonitrile and centrifugation, were redissolved in FA.

2.2.3 Transient absorption spectrometer

The ultrafast transient absorption spectrometer (Figure 2.1) used all TA experiments presented in this dissertation is a combination of commercially available systems: a regenerative amplified Ti:sapphire laser (Solstice, Spectra Physics), an optical parametric amplifier (TOPAS-C, Light Conversion), and the Helios spectrometer (Ultrafast Systems). The entire system is driven by the Solstice, which produces 800 nm, ~100 fs pulses at a 1 kHz repetition rate. A fraction of this output is directed to the TOPAS-C, which is capable of generating wavelengths ranging from 190 to 3000 nm. This TOPAS-C output is directed to the Helios, passed through a depolarizer, and focused into the sample for use as the pump pulse.

Another fraction of the Solstice output is directed into the Helios for use as the probe pulse. The probe pulse is delayed relative to the pump (Δt) using a motorized delay stage (3.3 ns maximum delay) and focused into a sapphire plate (WLG in Figure 2.1) to generate a broadband spectrum approximately ranging from 430 to 750 nm. Alternatively, an electronically delayed pulse of white light can be used for pump-probe delays of up to 400 microseconds, although this longer time window is not utilized in this dissertation. After white light generation, the probe pulse is split into two lines. One is focused into the sample, where it overlaps with the pump beam. The other bypasses the sample and is used as a reference (I_{ref}) to correct for any shot-to-shot variations in the probe white light generation. A chopper operating at 500 Hz blocks every other pump pulse. The transient absorption signal ΔA is calculated from the probe intensity (I_{probe}) transmitted through the sample on sequential pulses in the presence and absence of the pump according to

$$\Delta A(\lambda,\Delta t) = \log\left(\frac{I(\lambda)_{probe(pump\_off)}}{I(\lambda,\Delta t)_{probe(pump\_on)}}\right) - \log\left(\frac{I(\lambda)_{ref(pump\_off)}}{I(\lambda)_{ref(pump\_on)}}\right) \qquad \text{Eqn. 2.1}$$

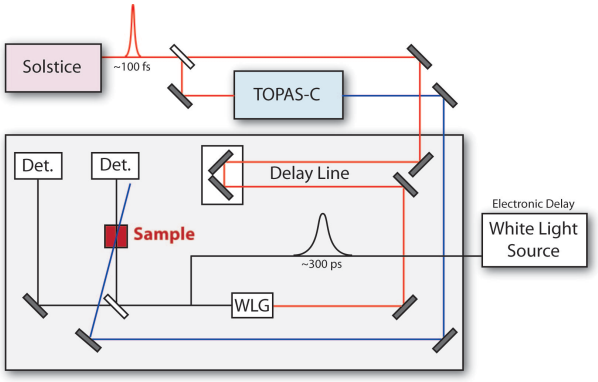

Figure 2.1: Transient absorption spectrometer schematic. A small fraction of the Solstice output is used to generate a white light probe pulse while the remainder is used to drive the generation of various pump pulse wavelengths in the TOPAS-C. The probe pulse traverses a motorized delay stage to generate pump-probe delays of up to 3.3 nanoseconds.

2.2.4 Transient absorption experimental conditions

The TA experiments described in the following chapters were all performed under similar experimental conditions. All samples are measured in 2mm quartz cuvettes sealed under an Argon atmosphere to prevent oxidative effects. Vigorous stirring using a magnetic stir bar, rotating approximately 320 rpm in the plane perpendicular to beam propagation, was employed to refresh the sample whenever illuminated.

The use of a broadband probe allows for the measurement of TA spectra at each pump-probe time delay. Figure 2.2 shows an example set of TA data for CdTe-ODPA QDs. The color image is constructed of the series of TA spectra ordered as a function of pump-probe time delay. The ΔA values associated with each color are given by the color scale. The upper panel represents a single TA spectrum, in this case taken at a 150 fs delay, as indicated by the horizontal grey dashed line on the color image. In this manner, an individual TA spectrum for any time delay can be viewed. The panel on the right corresponds to the ΔA values at a particular wavelength, in this case 570 nm as indicated by the vertical red dashed line on the color image. Extracting the TA kinetics at a single wavelength in this manner provides information about the evolution of a particular TA feature over time.

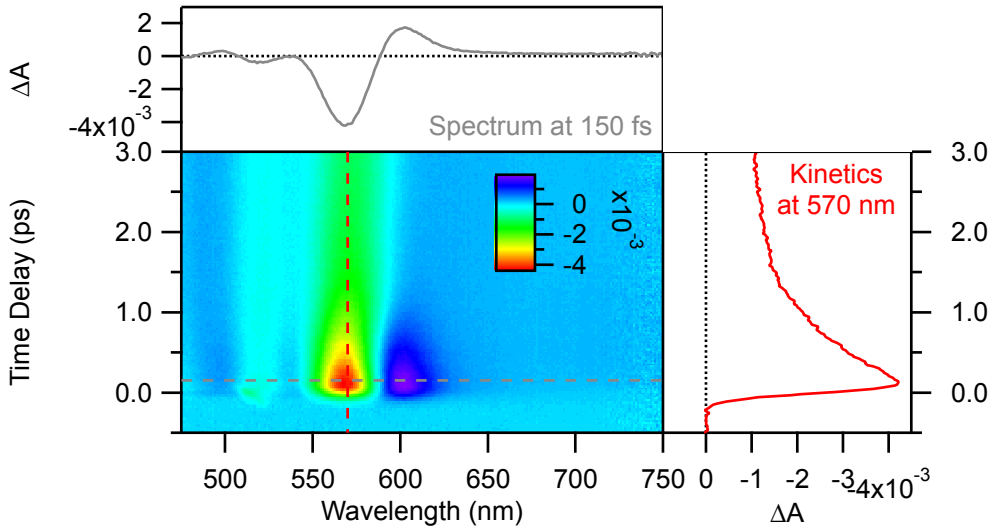

Figure 2.2: Example of spectrally resolved transient absorption data. Example TA data of CdTe-ODPA QDs collected using the experimental setup described above. The color map shows the value of ΔA (color scale) at each value of pump-probe time delay and wavelength. The upper panel shows ΔA as a function of wavelength for a particular time delay. This single spectrum, here at a time delay of 150 fs corresponding to the dashed grey line on the color map, highlights the TA spectral features in a given sample. The panel on the right shows ΔA as a function of pump-probe time delay for a particular wavelength. This kinetic trace, here at 570 nm corresponding to the dashed red line, demonstrates the evolution of a particular spectral feature in a given sample. Black dotted lines denote ΔA of zero.

While there are numerous reports of interesting multi-excitonic behavior in QDs,[3, 58-61] this dissertation focuses on singly excited QDs. This eliminates complications arising from multi-excitonic processes in photophysical measurements. To avoid multiple excitations per QD, the power of the pump pulse at the sample position was carefully monitored. TA kinetics were measured at a series of increasing pump powers. When kinetics show no indication of Auger recombination, typically an additional decay on the 1 – 100 ps timescale depending on QD material,[62-63] it indicates that the majority of QDs probed are singly excited. In the absence of power-dependent kinetics, we therefore conclude that ΔA signals are predominantly single-exciton. We rationalized this experimentally determined power-independent regime using an estimation of the exciton distribution for a given set of experimental conditions assuming a Poisson distribution of excitons per QD. Based on the pump beam spot size at the sample position and the absorptivity of the sample at the chosen pump wavelength, the average number of excitons generated per QD was

estimated for a certain pump power.[64-65] This estimation was also used to ensure similar distributions of excitons in a sample when exciting different excitonic transitions.

One of the significant benefits of this TA setup is the ability to tune the wavelength of the pump pulses using the TOPAS-C. This ability allows for the use of a state selective experimental approach.[66-68] In this approach, the pump pulses are tuned to be resonant with a particular transition in the absorption spectrum of the sample. This approach has a couple of notable benefits. With the ability to generate particular excitonic states in a sample, it is possible to evaluate carrier relaxation to the band edge. Similarly, it is possible to eliminate unwanted processes, such as carrier relaxation, simply by tuning the pump wavelength to excite the lowest energy transition in a sample. Both of these approaches will be applied to CdSe and CdTe QDs and explored in more detail in Chapter 4 and Chapter 5, respectively.

Another notable benefit of using the TOPAS-C to generate the pump pulses for TA experiments using the Helios spectrometer is the time resolution that can be achieved. Due to the utilization of up to 5 nonlinear processes in the TOPAS-C to generate the desired pump wavelength from 800 nm input pulses, significant compression of the pulse can occur. This can decrease pulse durations from 100 fs down to 65 – 85 fs. This shortening by only 15 – 35 fs means that pump pulses are shorter than half the vibrational period of the phonon modes in the crystalline QD materials studied in this dissertation. The pump pulses can therefore trigger these phonon modes, which then modulate subsequent absorption. This phenomenon is explored in significantly more detail in Section 5.3.6. By coupling it with the TOPAS-C, we are able to demonstrate the first observation of coherent exciton-phonon coupling in QDs using the commercially available Helios spectrometer.

When comparing spectra or kinetics on the subpicosecond to picosecond timescale, as done in this dissertation, chirp and time zero corrections are a necessary component of accurate TA data

analysis. Temporal chirp of the probe pulse arises from the group velocity mismatch among the redder and bluer wavelengths of the white light probe pulse. As the various wavelengths pass through optics and the sample, they travel at different speeds and are delayed relative to each other. Time zero (t_0), where there is maximal overlap between the pump and probe pulses, is therefore different for each probe wavelength.

Information to perform the chirp and t0 correction is obtained by collecting TA data on neat solvent under the conditions used for collecting TA data on the QD sample.[51, 69-70] To minimize any experimental variations between the solvent scan and data collection on the sample, the solvent scan is run immediately preceding the QD data collection (Figure 2.3a).

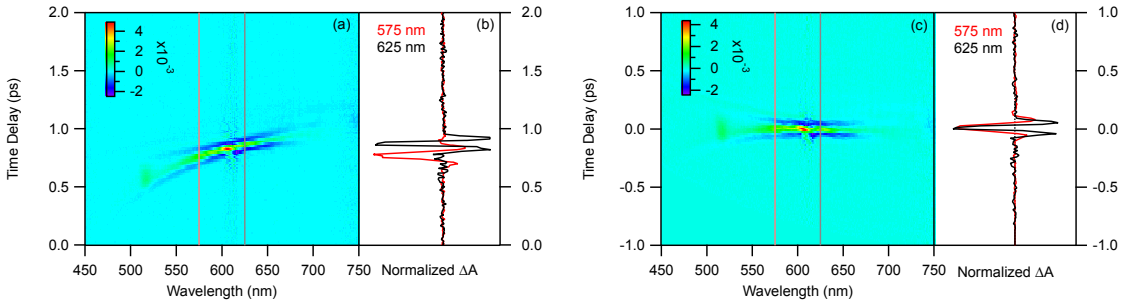

Figure 2.3: Example of chirp and t_0 correction. (a) As-measured transient absorption data for neat toluene in a 2 mm quartz cuvette. (b) Kinetic traces of two probe wavelengths, 575 and 625 nm, highlighted by the vertical grey and red lines. As can be seen from the offset of the kinetic trace peaks, t_0 for the two wavelengths are separated by 120 fs. (c) The transient absorption data in (a) following the chirp and t_0 correction. Both 575 and 625 nm probe wavelengths now share the same t_0.

Probing solvent molecules exhibiting a nonlinear optical response to the high intensity pump pulse generates the signals observed in pure solvent.[69-71] This solvent response is due to the combination of stimulated Raman emission and impulsive stimulated Raman scattering. Figure 2.3a demonstrates these signals for neat toluene in a 2 mm quartz cuvette. The solvent response kinetics (Figure 2.3b) at a particular probe wavelength λ is fit to the sum of a Gaussian and its first and second derivatives.[70-71] This Gaussian is then taken to be the pump-probe cross-correlation function. Its peak corresponds to t_0, and its width describes the instrumental response function (IRF) of the experiment at probe wavelength λ. This method of measuring the IRF is preferred over other

alternatives because it provides an IRF most reflective of our experimental conditions with minimal modification to the experimental setup. IRF timescales for the experiments reported here fall in the range of 65 – 200 fs, depending on the pulse characteristics and the extent of pump-probe detuning for each measurement.[51, 70-71]

To use a solvent scan to correct for the chirp of the probe continuum and associated difference in t_0, kinetic slices are fit for several probe wavelengths. The t_0 values extracted from these fits are used to characterize the chirp of the probe pulse. The TA data is then chirp-corrected to remove this artifact (Figure 2.3c), such that all probe wavelengths exhibit the same t_0 (Figure 2.3d). Solvent scans of this nature were used to characterize the experimental IRF and perform t_0 and chirp correction for all TA experiments discussed in this dissertation.

2.3 Theoretical – Single Band Effective Mass Model*

Single band effective mass calculations[54, 72-74] were used to model the QD-ligand systems discussed in Chapter 3 as well as interpret photoemission data of QDs in the gas-phase in Chapter 6. These calculations are based on a particle in a spherically symmetric potential well. By incorporating multiple layers of material, the spherically symmetric potentials become more complicated than the simple particle in an infinite well. To model electrons and holes in semiconductor materials, the effective mass approximation (EMA) is used. Ultimately, these calculations are evaluated numerically for an electron in a "conduction band well" and a hole in a "valence band well." Upon defining the potentials and effective masses in each spherically symmetric region, the electron and hole wave

---

* This section is adapted with permission from a published work:

- Schnitzenbaumer, Kyle J.; Dukovic, Gordana. "Chalcogenide-Ligand Passivated CdTe Quantum Dots Can Be Treated As Core/Shell Semiconductor Nanostructures" *J. Phys. Chem. C.* **2014**, 118, 28170 – 28178. © 2014 American Chemical Society.

functions and probability densities, electron and hole confinement energies (E_e and E_h), probabilities of finding carriers in each region, electron/hole coulomb interaction energy (E_c), electron/hole overlap integral (θ_{eh}), and band gap energy ($E_g^{(QD+L)} = E_g^{(bulk)} + E_e + E_h + E_c$) are calculated. The following sections describe the stepwise implementation of this calculation: initial parameter input, determining the mathematical form of the wave functions, finding carrier confinement energies, solving for wave function coefficients, calculation of probabilities, calculation of e^-/h^+ overlap integral, calculation of coulomb interaction energy, and calculation of band gap energy.

2.3.1 Initial parameter input

It is feasible to use a similar model for any number of spherically symmetric regions, though we focus on the 3-region case here. Region 1 is the QD core, region 2 is a shell around the QD core, and region 3 is the environment surrounding the QD/shell. Each region has a certain radial size, potential value, carrier effective masses, and dielectric constant. The input parameters used in the calculations are described in the appropriate chapters.

For a majority of the calculation, the electron and hole are treated as independent particles. The problem is defined as two separate potentials with two separate particles: an electron in a potential well defined by the conduction bands of the materials and a hole in a potential well defined by the valence bands. Only after finding the wave functions for the electron and hole separately do we consider their interaction with one another. Figure 2.4 provides a schematic of the physical and energetic input parameters. For each carrier, V_1 (potential in region 1), V_2, V_3, m_1 (effective mass in region 1), m_2, and m_3 are defined based upon the materials for regions 1, 2, and 3. Δ_{VB} (and likewise Δ_{CB}) is defined as the difference between the potential of region 1, V_1, and region 2, V_2. Similarly, $\Delta_{solvent,VB}$ ($\Delta_{solvent,CB}$) is defined as the difference between the potential of region 1, V_1, and region 3, V_3. The values of r_1 and r_2 define the size of the QD core and the width of the ligand shell,

respectively, which are the same for both carriers. Note that r_1 and r_2 are referred to as r_{QD} and r_{QD+L}, respectively, in Figure 2.4 and throughout Chapter 3.

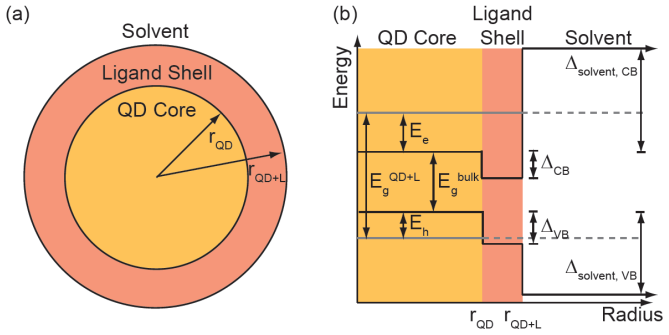

Figure 2.4: Schematic depiction of physical and energetic parameters for the EMA model calculations. (a) The physical parameters are r_{QD}, the radius of the QD core, and r_{QD+L}, the radius of the QD core plus the width of the ligand shell layer. (b) The energetic parameters are the bulk band gap energy of the QD core material (E_g^{bulk}), the bulk band offsets between the QD core and ligand shell materials ($\Delta_{CB/VB}$), and the bulk band offsets between the QD core and solvent materials ($\Delta_{solvent,CB/VB}$). The confinement energies of the electron and hole (E_e and E_h), as well as the Coulomb interaction energy between them, are used to calculate the band gap energy of the composite core/shell structure (E_g^{QD+L}). Adapted with permission from Schnitzenbaumer, Kyle J.; Dukovic, Gordana. *J. Phys. Chem. C.* **2014**, 118, 28170 – 28178. © 2014 American Chemical Society.

2.3.2 Determining the mathematical form of the wave functions

As we describe the methods used to perform the calculations in Sections 2.3.2 through 2.3.5, the focus will be on only one carrier, the electron; the same process is then repeated for the hole. The methodology for these calculations has been previously described[72] and is outlined here for clarity. For the Schrodinger equation

$$\left[-\frac{\hbar^2}{2}\nabla\frac{1}{m(r)}\nabla + V(\vec{r})\right]\Psi(\vec{r}) = E\Psi(\vec{r}) \qquad \text{Eqn. 2.2}$$

we treat mass as a radially dependent parameter.

The separation of radial and angular coordinates due to the spherically symmetric potential $V(\vec{r}) = V(r)$ leads to

$$\Psi_{nlm}(r,\theta,\phi) = R_{nlm}(r)Y_{lm}(\theta,\phi) \qquad \text{Eqn. 2.3}$$

Here the focus is only on 1S states. The spherical harmonic $Y_{0,0}(\theta, \phi)$ therefore gives a constant factor of $1/(4\pi)^{1/2}$ and we drop the subscripts on R(r). The assumption to deal with only 1S states

provides physical insight into the states in which the carriers spend the overwhelming majority of their excited state lifetimes and serves to simplify the calculation. While the single-band approach used here works well for band-edge states, a multi-band approach would be preferred for describing states above the band edge.[75]

With stepwise potentials

$$V(r) = \begin{cases} V_1 \text{ for } 0 \le r \le r_1 \\ V_2 \text{ for } r_1 \le r \le r_2 \\ V_3 \text{ for } r_2 < r < \infty \end{cases} \quad \text{Eqn. 2.4}$$

The radial eigenfunctions consist of 3 parts, one for each region.

$$R(r) = \begin{cases} R_1 \text{ for } 0 \le r \le r_1 \\ R_2 \text{ for } r_1 \le r \le r_2 \\ R_3 \text{ for } r_2 < r < \infty \end{cases} \quad \text{Eqn. 2.5}$$

The solutions to the Schrodinger equation with a stepwise, spherically symmetric potential are linear combinations of Bessel functions.[72, 76-77] These radial eigenfunctions take on different functional forms in each region depending on how the particle's energy compares with the potential within that region. This is the deciding factor in determining the behavior of the carrier wave functions in each region.

If E > V in region q, $R_q(r)$ is a combination of a spherical Bessel and Neumann function.

$$R_q(r) = A_q j(k_q r) + B_q n(k_q r) \quad \text{Eqn. 2.6}$$

$$k_q = \sqrt{\frac{2m_q(E_e - V_q)}{\hbar^2}} \quad \text{Eqn. 2.7}$$

If E < V in region q, then $R_q(r)$ is a linear combination of two Hankel functions with imaginary arguments.

$$R_q(r) = A_q h^{(1)}(ik_q r) + B_q h^{(2)}(ik_q r) \qquad \text{Eqn. 2.8}$$

$$k_q = \sqrt{\frac{2m_q(V_q - E_e)}{\hbar^2}} \qquad \text{Eqn. 2.9}$$

With three regions, many different combinations, and therefore many different forms for the wave functions are possible. Due to the parameters of the systems studied here, there are only three relevant cases encountered, Case I ($E_e > V_1$, $E_e < V_2$, $E_e < V_3$), Case II ($E_e > V_1$, $E_e > V_2$, $E_e < V_3$), and Case III ($E_e < V_1$, $E_e > V_2$, $E_e < V_3$).

Regardless of which case describes a system, there are two requirements that allow for simplification of the basic forms of the wave functions. (1) The wave function must be finite and well behaved (cannot be divergent) at r = 0, and (2) the wave function must tend towards zero as r approaches infinity. These two requirements always leave four unknown weighting coefficients: A_1 in R_1, A_2 and B_2 in R_2, and A_3 in R_3. After simplification of the $R_q(r)$ equations above, the following is a summary of the forms of the wave function for the three cases of interest.

Table 2.1: Mathematical forms of carrier wave functions for various cases of input parameters.

	$R_1(r)$	$R_2(r)$	$R_3(r)$
Case I	$R_1(r) = \frac{A_1 \sin(k_1 r)}{k_1 r}$	$R_2(r) = \frac{(A_2 + B_2)\sinh(k_2 r) + (B_2 - A_2)\cosh(k_2 r)}{k_2 r}$	$R_3(r) = -A_3 \frac{e^{-k_3 r}}{k_3 r}$
Case II	$R_1(r) = \frac{A_1 \sin(k_1 r)}{k_1 r}$	$R_2(r) = \frac{A_2 \sin(k_2 r)}{k_2 r} - \frac{B_2 \cos(k_2 r)}{k_2 r}$	$R_3(r) = -A_3 \frac{e^{-k_3 r}}{k_3 r}$
Case III	$R_1(r) = \frac{A_1\left(e^{k_1 r} - e^{-k_1 r}\right)}{k_1 r}$	$R_2(r) = \frac{A_2 \sin(k_2 r)}{k_2 r} - \frac{B_2 \cos(k_2 r)}{k_2 r}$	$R_3(r) = -A_3 \frac{e^{-k_3 r}}{k_3 r}$

2.3.3 Finding confinement energy

Confinement energy (E_e) is then found for the set of input parameters. At this stage, for the Cases I, II, or III above, the form of the wave function in each region is known (Table 2.1). The boundary conditions requiring continuity and current conservation[78-79] are

$$R_q(r_q) = R_{q+1}(r_q) \qquad \text{Eqn. 2.10}$$

and

$$\frac{1}{m_q}\frac{dR_q(r)}{dr}\bigg|_{r=r_q} = \frac{1}{m_{q+1}}\frac{dR_{q+1}(r)}{dr}\bigg|_{r=r_q} \qquad \text{Eqn. 2.11}$$

Application of these boundary conditions yields 4 equations and 4 unknown coefficients (for N regions, this still holds true; 2N-2 equations for 2N-2 unknown coefficients due to the additional requirements on q=1 and q=N). The only unknown aside from the unknown coefficients is the confinement energy E_e (which is buried inside the k_q expressions in $R_q(r)$).

Solving for E_e is done by building a system of linear equations using the above boundary conditions applied to the forms of the wave functions in each region for the specific case being used.

$$\begin{pmatrix} \gamma 11 & \gamma 12 & \gamma 13 & \gamma 14 \\ \gamma 21 & \gamma 22 & \gamma 23 & \gamma 24 \\ \gamma 31 & \gamma 32 & \gamma 33 & \gamma 34 \\ \gamma 41 & \gamma 42 & \gamma 43 & \gamma 44 \end{pmatrix} \begin{pmatrix} A_1 \\ A_2 \\ B_2 \\ A_3 \end{pmatrix} = 0 \qquad \text{Eqn. 2.12}$$

where γ11, γ12, γ13, and γ14 are determined from the application of Eqn. 2.10 to the boundary of regions 1 and 2; γ21, γ22, γ23, and γ24 are determined from the application of Eqn. 2.11 to the boundary of regions 2 and 3; γ31, γ32, γ33, and γ34 are determined from the application of (Condition 2) to the boundary of regions 1 and 2; and γ41, γ42, γ43, and γ44 are determined from the application of (Condition 2) to the boundary of regions 2 and 3.

The solution to this matrix is nontrivial only if the determinant of this matrix is zero. By setting the determinant to zero, an equation of only one variable, E_e, exists. This is solved numerically, with the value of E_e approximated to within 10^{-5} eV.

2.3.4 Solving for wave function coefficients

Regardless of which case used and, therefore, what each individual matrix element γ_{xx} is, expressing all the coefficients in terms of A_1 goes as follows.

$$B_2 = \left(\frac{\frac{\gamma 11}{\gamma 12} - \frac{\gamma 31}{\gamma 32}}{\frac{\gamma 33}{\gamma 32} - \frac{\gamma 13}{\gamma 12}} \right) A_1 \qquad \text{Eqn. 2.13}$$

$$A_2 = \frac{-\gamma 11 A_1 - \gamma 13 B_2}{\gamma 12} \qquad \text{Eqn. 2.14}$$

$$A_3 = \frac{-\gamma 22 A_2 - \gamma 23 B_2}{\gamma 24} \qquad \text{Eqn. 2.15}$$

Normalization of the overall wave function then allows us to determine the wave function coefficients. Starting with the usual normalization condition,

$$\int \left| \Psi_e(r,\theta,\phi) \right|^2 d\tau = 1 \qquad \text{Eqn. 2.16}$$

the function $\Psi_{nlm}(r,\theta,\phi) = R_n(r) Y_{lm}(\theta,\phi)$ is inserted and expressed in polar coordinates to give

$$\int_{\phi=0}^{2\pi} \int_{\theta=0}^{\pi} \int_{r=0}^{\infty} \left| R_e(r) Y_{0,0}(\theta,\phi) \right|^2 r^2 \sin(\theta) dr d\theta d\phi = 1 \qquad \text{Eqn. 2.17}$$

Simplifying by using the fact that the spherical harmonic $Y_{0,0}(\theta,\phi)$ is already normalized, the expression becomes

$$\int_{r=0}^{\infty} \left| R_e(r) \right|^2 r^2 dr = 1 \qquad \text{Eqn. 2.18}$$

Using the piecewise function for $R_e(r)$ determined by the appropriate case for E_e gives

$$\int_{r=0}^{r1} |R_1(r)|^2 r^2 dr + \int_{r=r1}^{r2} |R_2(r)|^2 r^2 dr + \int_{r=r2}^{\infty} |R_3(r)|^2 r^2 dr = 1 \qquad \text{Eqn. 2.19}$$

where the coefficients in $R_1(r)$, $R_2(r)$, and $R_3(r)$ have all been expressed in terms of A_1. The normalization condition is solved for A_1, which is then subsequently used to find A_2, B_2, and A_3. There are now no longer any unknowns in our expression for the wave function $R_e(r)$, which can then be plotted.

2.3.5 Calculation of probabilities

The probability of finding the carrier in a particular region q is the probability density in region q divided by the probability density in all regions. Because the wave function has already been normalized, this denominator is simply 1.

$$P(q) = \frac{\int |R_q(r)|^2 r^2 \, d\tau}{\int |R_1(r)|^2 r^2 \, dr + \int |R_2(r)|^2 r^2 \, dr + \int |R_3(r)|^2 r^2 \, dr} = \frac{\int |R_q(r)|^2 r^2 \, d\tau}{1} \qquad \text{Eqn. 2.20}$$

2.3.6 Calculation of electron/hole overlap

To find the confinement energy of the hole, Sections 2.3.2 through 2.3.5 are repeated using the hole and VB input parameters. With the confinement energies and the wave functions for both the carriers, we consider the interaction of the carriers with each other. The overlap integral[80-82] is

$$\theta_{eh} = \left| \int \Psi_e(r,\theta,\phi) \Psi_h(r,\theta,\phi) d\tau \right|^2 \qquad \text{Eqn. 2.21}$$

Using the normalization of the spherical harmonics to simplify gives

$$\theta_{eh} = \left| \int R_e(r) R_h(r) r^2 \, dr \right|^2 \qquad \text{Eqn. 2.22}$$

2.3.7 Calculation of Coulomb interaction energy

The Coulomb interaction energy of the exciton is treated to first order in perturbation theory as previously described,[72] which changes the energies but not the states

$$E_c = \frac{-e^2}{4\pi}\int\int \frac{\left|\Psi_e(\vec{r}_e)\right|^2\left|\Psi_h(\vec{r}_h)\right|^2}{\left|\vec{r}_e-\vec{r}_h\right|\varepsilon(r_e,r_h)}d\vec{r}_e d\vec{r}_h \qquad \text{Eqn. 2.23}$$

Again, using the fact that the spherical harmonics are normalized allows for simplification.

$$E_c = \frac{-e^2}{4\pi}\int_{r_h=0}^{\infty}\int_{r_e=0}^{\infty} \frac{\left|R_e(r_e)\right|^2\left|R_h(r_h)\right|^2 r_e^{\,2} r_h^{\,2}}{\left|r_e-r_h\right|\varepsilon(r_e,r_h)}dr_e dr_h \qquad \text{Eqn. 2.24}$$

To deal with the varying dielectric constant in each of the three regions, we separate the calculation into three parts, one for each region, explicitly using the appropriate dielectric constant in each region.

$$E_c = E_{c1} + E_{c2} + E_{c3} \qquad \text{Eqn. 2.25}$$

$$\begin{aligned} E_c = {} & \frac{-e^2}{4\pi\varepsilon_0\varepsilon_{q1}}\int_{r_h=0}^{r1}\int_{r_e=0}^{r1} \frac{\left|R_e(r_e)\right|^2\left|R_h(r_h)\right|^2 r_e^2 r_h^2}{\left|r_e-r_h\right|}dr_e\,dr_h \\ & + \frac{-e^2}{4\pi\varepsilon_0\varepsilon_{q2}}\int_{r_h=r1}^{r2}\int_{r_e=r1}^{r2} \frac{\left|R_e(r_e)\right|^2\left|R_h(r_h)\right|^2 r_e^2 r_h^2}{\left|r_e-r_h\right|}dr_e\,dr_h \\ & + \frac{-e^2}{4\pi\varepsilon_0\varepsilon_{q3}}\int_{r_h=r2}^{\infty}\int_{r_e=r2}^{\infty} \frac{\left|R_e(r_e)\right|^2\left|R_h(r_h)\right|^2 r_e^2 r_h^2}{\left|r_e-r_h\right|}dr_e\,dr_h \end{aligned} \qquad \text{Eqn. 2.26}$$

We use the following expansion of $1/|r_e\text{-}r_h|$ to simplify

$$\frac{1}{\left|r_e-r_h\right|} = \sum_{l=0}^{\infty}\sum_{m=-l}^{l}\frac{4\pi}{2l+1}\frac{r_<^{\,l}}{r_>^{\,l+1}}Y_{l,m}(\theta_e,\phi_e)*Y_{l,m}(\theta_h,\phi_h) \qquad \text{Eqn. 2.27}$$

where $r_>$ and $r_<$ indicate the larger and smaller of r_e and r_h, respectively. Using the orthonormality of the spherical harmonics, only the l=m=0 terms survive and the first term of E_c, E_{c1}, becomes

$$E_{c1} = \frac{-e^2}{4\pi\varepsilon_0\varepsilon_{q1}}\int_{r_h=0}^{r1}\int_{r_e=0}^{r1} \frac{\left|R_e(r_e)\right|^2\left|R_h(r_h)\right|^2 r_e^{\,2} r_h^{\,2}}{r_>}dr_e dr_h \qquad \text{Eqn. 2.28}$$

The double integral must be broken down further since $r_e > r_h$ in the region of $0 < r_h < r_e$, while $r_h > r_e$ in the region of $r_e < r_h < r_1$.

$$E_{c1} = \frac{-e^2}{4\pi\varepsilon_0\varepsilon_{q1}} \int_{r_e=0}^{r_1} \left(\int_{r_h=0}^{r_e} \frac{|R_e(r_e)|^2 |R_h(r_h)|^2 r_e^{\,2} r_h^{\,2}}{r_e} dr_h + \int_{r_h=r_e}^{r_1} \frac{|R_e(r_e)|^2 |R_h(r_h)|^2 r_e^{\,2} r_h^{\,2}}{r_h} dr_h \right) dr_e \qquad \text{Eqn. 2.29}$$

In a similar manner, E_{c2} and E_{c3} become

$$E_{c2} = \frac{-e^2}{4\pi\varepsilon_0\varepsilon_{q2}} \int_{r_e=r_1}^{r_2} \left(\int_{r_h=r_1}^{r_e} \frac{|R_e(r_e)|^2 |R_h(r_h)|^2 r_e^{\,2} r_h^{\,2}}{r_e} dr_h + \int_{r_h=r_e}^{r_2} \frac{|R_e(r_e)|^2 |R_h(r_h)|^2 r_e^{\,2} r_h^{\,2}}{r_h} dr_h \right) dr_e \qquad \text{Eqn. 2.30}$$

and

$$E_{c3} = \frac{-e^2}{4\pi\varepsilon_0\varepsilon_{q3}} \int_{r_e=0}^{\infty} \left(\int_{r_h=r_2}^{r_e} \frac{|R_e(r_e)|^2 |R_h(r_h)|^2 r_e^{\,2} r_h^{\,2}}{r_e} dr_h + \int_{r_h=r_e}^{\infty} \frac{|R_e(r_e)|^2 |R_h(r_h)|^2 r_e^{\,2} r_h^{\,2}}{r_h} dr_h \right) dr_e \qquad \text{Eqn. 2.31}$$

2.3.8 Calculation of band gap energy

With the confinement energies and the Coulomb interaction energy in hand, we calculate the band gap energy

$$E_g^{(QD+L)} = E_g^{(bulk)} + E_e + E_h + E_c \qquad \text{Eqn. 2.32}$$

where $E_g^{(bulk)}$ is the bulk band gap of the QD material.

Chapter 3. Theoretical Foundations for Describing Chalcogenide Capped QDs*

> "You grow up thinking science is this pure thing, but when you get into it you find out its messy and full of guesses and approximations."
> - Jorge Cham

3.1 Abstract

Chalcogenide ligands (S^{2-}, Se^{2-}, Te^{2-}) are attractive candidates for passivation of surfaces of colloidal quantum dots (QDs) because they can enhance inter-particle or particle-adsorbate electronic coupling. Devices made with QDs in which insulating long-chain aliphatic ligands were replaced with chalcogenide ligands have exhibited improved charge transfer and transport characteristics. While these ligands enable promising device performance, their impact on the electronic structure of the QDs that they passivate is not understood. In this chapter, we describe significant changes in band-gap energies of CdTe QDs (up to 250 meV, 10% of the original band gap) that occur when native aliphatic ligands are replaced with chalcogenides. These changes are dependent on the ligand and the particle size. To explain the observed changes in band-gap energies, we used the single band effective mass approximation (EMA) to model the ligand layer as a thin

---

* This chapter is adapted with permission from the published work:

- Schnitzenbaumer, Kyle J.; Dukovic, Gordana. "Chalcogenide-Ligand Passivated CdTe Quantum Dots Can Be Treated As Core/Shell Semiconductor Nanostructures" *J. Phys. Chem. C.* **2014**, 118, 28170 – 28178. © 2014 American Chemical Society.

shell of Cd-chalcogenide formed by the bonding of chalcogenide ligands to partially coordinated Cd surface atoms. The model correctly predicted the observed trends in CdTe QD band-gap energies. The model also predicts that electrons and holes in chalcogenide-capped QDs can be significantly delocalized outside the core/shell structure, enhancing electronic coupling between QDs and adjacent species. Our work provides a simple description of the electronic structure of chalcogenide-capped QDs and may prove useful for the design of QD-based devices.

3.2 Introduction

Semiconductor nanocrystals show promise for optoelectronic applications because their electronic, optical, and surface properties can be controlled via chemical synthesis.[3-4, 21, 83-85] Devices utilizing these materials, such as photovoltaic or photochemical systems, require efficient collection of photogenerated carriers.[3, 6, 15] The long-chain aliphatic surface-capping ligands commonly used in nanocrystal synthesis form an insulating barrier that minimizes electronic coupling between the particle and its environment. Significant research efforts have focused on post-synthetic replacement of the insulating ligands by shorter and/or more conductive species.[4, 35-36, 38-48, 86] Many such ligands have been shown to improve carrier transport in devices.[35-36, 40, 43-44, 47, 49-50, 86-95] In the regime of weak electronic coupling, charge transport in arrays of semiconductor nanocrystals occurs via nearest neighbor hopping, which is enabled by inter-particle tunneling through surface-capping ligands.[35, 96-97] In order to improve inter-particle electronic coupling, ligand exchange can be used to tune both the heights (e.g., ligand orbital energies) and the widths (e.g., ligand length) of the tunneling barriers. Increasing the probability of a carrier tunneling into the surrounding environment results in more efficient charge transport. With sufficiently large coupling, band-like transport can be achieved in nanocrystal arrays.[95, 98-99]

From the standpoint of electronic coupling, chalcogenide ligands S^{2-}, Se^{2-}, and Te^{2-} are very appealing surface-capping agents for nanocrystals because they create very thin ligand layers.[40, 45] They have been employed in nanocrystal-based devices with promising results. Field effect transistors containing CdSe quantum dots (QDs) capped with S^{2-} ligands have high electron mobilities with almost no hysteresis.[40, 50, 87] High mobilities point to enhanced inter-particle coupling. Similarly, CdSe QD sensitized solar cells exhibited improved photovoltaic performance when long-chain aliphatic ligands were replaced with S^{2-}.[93, 100] These improvements were attributed to a higher rate of electron transfer from CdSe QDs to TiO_2 through the very thin S^{2-} ligand layer. While the performance of chalcogenide-capped QDs in devices is promising, the impact of chalcogenide ligands on the electronic structure of the QDs that they passivate is not understood. Specifically, in order to improve the design of devices based on chalcogenide-capped QDs, it is desirable to understand how the ligands affect quantum confinement and wave function probability distributions inside and outside the QD. These quantities are intimately related to inter-particle or particle-adsorbate electronic coupling and ultimately govern properties such as carrier mobilities and charge transfer rates.

In this chapter, we describe the optical and electronic properties of CdTe QDs of a range of radii (1.37 - 2.24 nm) functionalized with chalcogenide ligands S^{2-}, Se^{2-}, and Te^{2-}. We denote these structures as CdTe-S, CdTe-Se, and CdTe-Te respectively. Compared to CdTe QDs functionalized with organic ligands, chalcogenide-capped QDs exhibited large (up to 250 meV) red shifts of the band gap transitions in the absorption spectra. The spectral changes did not follow a trend based on the chalcogen order in the periodic table. Instead, largest red shifts were exhibited by CdTe-Se and smallest by CdTe-Te. Moreover, we observed a striking similarity between the band gap energy of CdTe QDs passivated with the Se^{2-} ligand and a CdTe/CdSe core-shell heterostructure. Consequently, we used a single band effective mass approximation (EMA) to model the ligand layer

as a monolayer CdX (X= S^{2-}, Se^{2-}, and Te^{2}) shell. This model correctly predicted the experimentally observed ordering of band-gap transition energies with no adjustable parameters, suggesting similarities between the chalcogenide-ligand capped QDs and core/shell structures. Using the EMA model, we calculated radial probability densities of electron and hole wave functions and showed that up to several percent of each carrier can be found outside the CdTe-X structure, with the values depending on both ligand identity and particle size. These values are orders of magnitude higher than probabilities of finding the carriers outside the ligand shell for organic-ligand capped QDs. Our work demonstrates that EMA modeling can be used to predict the electronic structure and carrier distribution in QDs passivated with chalcogenide ligands and provides guidance for selection of optimal QD structures for specific devices.

3.3 Results & Discussion

3.3.1 Ligand-induced changes in band gap energy

The band gap transition of CdTe is particularly sensitive to external perturbations due to its relatively light electron and hole effective masses and consequent strong quantum confinement (Bohr exciton radius = 7.3nm[101]). Thus, CdTe QDs are an excellent model system for an investigation of the impacts of chalcogenide ligands on band gap energy and electronic structure of nanocrystals. To obtain CdTe QD with a range of sizes and narrow, well-defined, band gap transition peaks, we synthesized zinc blende CdTe QDs capped with long-chain octadecylphosphonic acid (CdTe-ODPA).[23] UV-Vis absorption spectra* of selected sizes of as-grown CdTe-ODPA QDs are shown in Figure 3.1. The radii of the QDs used in this chapter range

* All steady state UV-Vis absorption spectra were obtained using an Agilent 8453 UV-Vis spectrophotometer. To prevent oxidation of the samples, spectra were recorded less than 5 min after removal from the glove box in 2 mm quartz cuvettes sealed under an Ar atmosphere.

from 1.37 to 2.24 nm as calculated using previously published absorption energy vs. size comparisons.[52, 102-103]

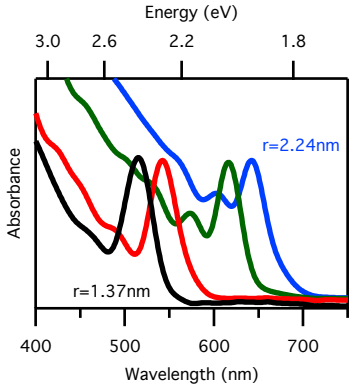

Figure 3.1: Absorption spectra of CdTe-ODPA QDs. Absorption spectra of as-grown CdTe QDs with r = 1.37 nm (black), r = 1.54 nm (red), r = 2.01 nm (green), and r = 2.24 nm (blue) as calculated via published relations.

To replace the long-chain ODPA ligands, we followed ligand exchange procedures developed by Talapin et. al. utilizing S^{2-}, Se^{2-}, and Te^{2-} as surface-capping ligands.[40] In that report, chalcogenide ligands were shown to completely displace aliphatic ligands by binding to partially coordinated Cd atoms on the nanocrystal surface via nucleophilic substitution.[40] Dynamic light scattering confirmed that chalcogenide-capped QDs were soluble as individual particles with decreased hydrodynamic radii consistent with replacement of aliphatic ligands with a layer of chalcogenide ligands with no changes in particle size and shape.[40]

In our ligand-exchanged samples, elemental analysis using energy dispersive spectroscopy* revealed the absence of P and presence of S, Se, and Te in the ligand-exchanged samples. Figure 3.2 shows representative EDS spectra of r = 1.54 nm CdTe QDs capped with ODPA (grey), MPA (black), S^{2-} (red), Se^{2-} (blue), and Te^{2-} (green), as well as CdTe/CdSe-ODPA QDs (cyan). The

* Energy Dispersive Spectroscopy (EDS) spectra were collected using a Jeol JSM-6480LV SEM with an INCA PentaFETx3 EDS detector. Samples were drop cast on a silicon wafer mounted to an SEM stub using double sided carbon tape.

energies characteristic of relevant elements are indicated by vertical dashed lines, and changes in elemental composition as a result of the ligand exchanges are highlighted using boxes. The spectrum of the as-grown CdTe-ODPA QDs exhibits peaks characteristic of elements Cd, Te, and P. The presence of P is consistent with surface-capping by ODPA. The CdTe-MPA, CdTe-S, and CdTe-Se ligand-exchanged samples lack this P peak, while new peaks corresponding to S (for CdTe-MPA and CdTe-S) and Se (for CdTe-Se) are present. The presence of S in the CdTe-MPA sample is due to the thiol group. The CdTe–Te sample lacks the P peak, while demonstrating an enhancement in the series of peaks characteristic of Te. The spectrum of the CdTe/CdSe-ODPA core/shell sample is qualitatively similar to that of the CdTe-ODPA, with the exception of the additional Se peak as expected. The CdTe/CdSe-ODPA spectrum is also qualitatively similar to that of CdTe-Se, with the exception of the additional P peak. The presence of small peaks corresponding to Na is due to the presence of Na^{+} as the counter ion of S^{2-}, Se^{2-}, Te^{2-} in the ligand exchange solutions. Note that both silicon and oxygen are present in all samples due to oxide on the Si wafer used as the substrate on which the samples were prepared for EDS analysis. For as-grown CdTe-ODPA, Cd:Te ratios range from 1:0.5 to 1:0.9. This suggests that as-synthesized CdTe QDs are Cd-rich, and the partially coordinated Cd QD surfaces could be expected to interact with the S^{2-}, Se^{2-}, and Te^{2-} chalcogenide ligands to form a thin ligand shell layer.

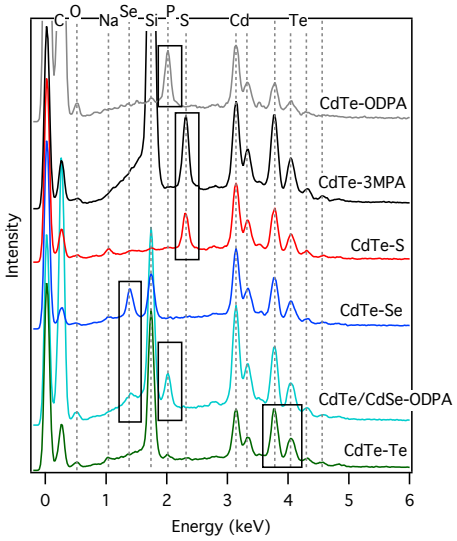

Figure 3.2: Energy Dispersive Spectroscopy spectra for ligand exchanged CdTe QDs. Representative EDS spectra for the as-grown CdTe-ODPA (grey) and CdTe/CdSe core/shell QDs (cyan), as well as MPA (black), S^{2-} (red), Se^{2-} (blue), and Te^{2-} (green) ligand-exchanged samples. All samples were prepared from the same batch of r = 1.54nm CdTe QDs. Adapted with permission from Schnitzenbaumer, Kyle J.; Dukovic, Gordana. *J. Phys. Chem. C.* **2014**, 118, 28170 – 28178. © 2014 American Chemical Society.

For purposes of comparison with organic surface-capping ligands in the same solvent, we also prepared CdTe QDs capped with 3-mercaptopropionic acid (MPA). The ligand-exchanged QD solutions were dispersed in formamide, resulting in optically clear samples with no evidence of precipitation. Samples of the same size QDs with the four different ligands were noticeably different in color. Photographs of solutions of r=1.60 nm CdTe QDs are shown in Figure 3.3. A color change from pink for CdTe-MPA (same color as CdTe-ODPA), red-brown for CdTe-S, brown for CdTe-Se, and back to pink for CdTe-Te QDs is observed.

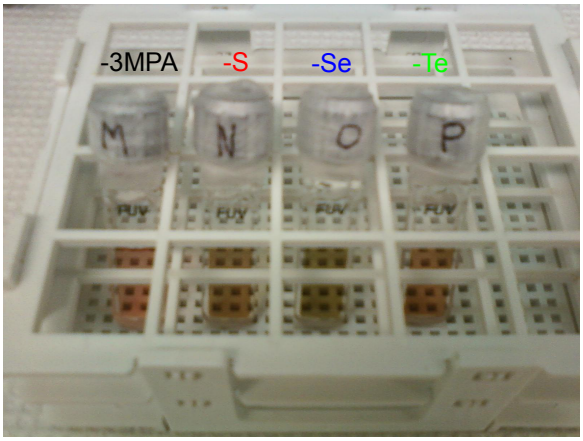

Figure 3.3: Photograph of ligand exchanged CdTe QDs. Photograph of the solutions resulting from ligand exchange to MPA, S^{2-}, Se^{2-}, and Te^{2-} on r = 1.60 nm CdTe-ODPA QDs. The image shows the solutions to be optically clear, as well as having noticeably different colors with different ligands. Adapted with permission from Schnitzenbaumer, Kyle J.; Dukovic, Gordana. *J. Phys. Chem. C.* **2014**, 118, 28170 – 28178. © 2014 American Chemical Society.

To examine the effects of ligand exchange on the optical spectra and band-gap transition energies of CdTe QDs, we acquired UV-Vis absorption spectra of CdTe QDs with radii ranging from 1.37 to 2.24 nm passivated with five ligands: ODPA, MPA, S^{2-}, Se^{2-}, Te^{2-}. To avoid sample oxidation, spectra were recorded in sealed cuvettes immediately upon ligand exchange under an inert atmosphere. As a representative example of the observed trends, absorption spectra for r_{QD}=1.54 nm CdTe QDs capped with the five ligands are shown in Figure 3.4a. CdTe-MPA spectra are qualitatively similar to the CdTe-ODPA spectra, whereas the CdTe-S, CdTe-Se, and CdTe-Te spectra are strikingly different. Compared to CdTe-MPA, spectra of chalcogenide-capped QDs exhibit large red shifts in the band-gap transition peak. To determine the band gap peak position, we find the point of maximum curvature by examining the second derivative of the band gap peak (Figure 3.4c and d). The order of band-gap transition energies as a function of surface-capping ligand is: CdTe-ODPA (542 nm) ≈ CdTe-MPA (546 nm) > CdTe-Te (564 nm) > CdTe-S (586 nm) > CdTe-Se (615 nm). The change in band gap energy of the CdTe-Se represents ~10% of the pre-ligand exchange value. Note that this ordering of band gap energies does not correlate with the

order of the chalcogens in the periodic table. Chalcogenide-capped QDs also exhibit broader peaks than CdTe-MPA, though the peaks become narrower with increasing QD size. Similar spectral broadening was observed previously for chalcogenide and chloride-capped QDs in solution, and its origin is not well understood.[40, 42] In the case of the S^{2-} ligand, broadening due to mixing of hole and surface states has been proposed, and may explain why CdTe-S peaks are particularly broad.[104]

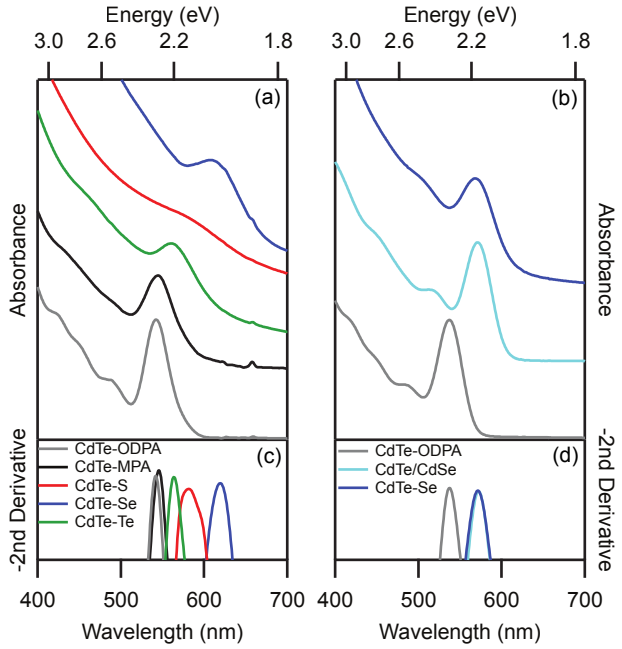

Figure 3.4: Absorption spectra of ligand exchanged CdTe QDs and core/shell CdTe/CdSe. (a) Absorption spectra of CdTe-MPA (black), CdTe-S (red), CdTe-Se (blue), and CdTe-Te (green) QDs with r_{QD}=1.54 nm, all obtained by ligand exchange from the same sample of as-synthesized CdTe-ODPA (grey). The spectra illustrate large spectral shifts in chalcogenide-capped samples. (b) Absorption spectra of CdTe/CdSe core/shell (light blue) and ligand-exchanged CdTe-Se (dark blue) made from the same CdTe QD cores (grey). Growing a thin CdSe shell around the CdTe core yields a similar red shift in band gap energy as exchanging the native ODPA ligands for Se^{2-} ligands. (c) Second derivatives (multiplied by -1) of the spectra in a, indicating the point of maximum curvature. (d) Second derivatives of the spectra in (b) multiplied by -1. Adapted with permission from Schnitzenbaumer, Kyle J.; Dukovic, Gordana. *J. Phys. Chem. C.* **2014**, 118, 28170 – 28178. © 2014 American Chemical Society.

Absorption and emission spectra of QDs can exhibit spectral shifting due to the solvent dielectric environment or changes in the quantum confinement, but these effects alone cannot explain the ordering of band-gap energies described above. We rule out solvent effects on the basis of two observations: (i) the relative similarity of band gap energies of CdTe-ODPA in toluene and CdTe-MPA in formamide and (ii) the marked difference of peak positions among samples that are

all in the same solvent (CdTe-MPA, CdTe-S, CdTe-Se, and CdTe-Te, all in formamide). We can also rule out the dielectric environment of the ligand shell as the sole cause of the red shift. A correction to the band gap energy due to the different ligand shell dielectric environments[105] leads to red shifts of up to 10 meV for r_{QD}=1.5nm CdTe QDs. The spectra in Figure 3.4a, on the other hand, exhibit red shifts of >100 meV for chalcogenide-capped QDs. We can also rule out a simple quantum confinement effect in which the only role of the chalcogenide ligands is to increase the QD radius. This would cause the CdTe-Te sample, with the ionic radius of Te being larger than that of both S and Se, to experience the weakest confinement and thus the largest red shift. As shown in Figure 3.4a, the CdTe-S and CdTe-Se samples exhibit larger red shifts and lower band gap energies than CdTe-Te.

To explain the behavior of band gap transitions for CdTe QDs with various surface-capping ligands, we postulate that the chalcogenide ligand forms a thin shell of Cd-chalcogenide that makes the QD-ligand shell composite similar to a CdTe/CdX core/shell nanocrystal. Like CdSe QDs,[73, 106-109] phosphonic-acid capped CdTe QDs are cation-rich, with Cd atoms comprising the majority of the surface.[103] The partially coordinated surface Cd atoms are available to interact with the negatively charged chalcogenide ligands, and could form a Cd-chalcogenide layer, which may act as a thin, semiconductor shell. In this case, the chalcogenide ligand exchange could be thought of as a controlled, single-layer shell growth similar to the first step of a SILAR process.[110] The precise chemical structure at the surface of a chalcogenide-capped QD is not understood. Solubility in polar solvents has been attributed to a negative surface charge[40] with fewer than 10 elemental charges on the surface of each QD in solution.[50] In solid arrays S^{2-} was thought to form a CdS shell around a CdSe QD.[45, 93] Thus, from the standpoint of surface chemistry, it is plausible that chalcogenide ligands could form a CdX semiconductor layer on the CdTe QDs.

If chalcogenide ligands do form CdX semiconductor shells around QDs, chalcogenide-capped CdTe QDs should have spectra similar to those of CdTe/CdX core/shell structures synthesized by seeded growth of the semiconductor shell. In Figure 3.4b, we compare the absorption spectrum of ligand-exchanged CdTe-Se to the spectrum of CdTe/CdSe core/shell samples prepared by high temperature shell growth on the same sample of r_{QD}=1.54 nm CdTe cores. A comparison of peak positions and intensities with those from published spectra of CdTe/CdSe core-shell QDs[111] suggests that the CdTe/CdSe core/shell sample in Figure 3.4b has approximately a single CdSe monolayer shell (we define monolayer here as a single layer of CdSe, i.e. half of a unit cell). The growth of this monolayer CdSe shell causes a red shift of the band gap transition peak of ~140 meV, whereas the Se^{2-} ligand exchange causes a red shift of ~130 meV. Considering the very different methods for preparing these two samples, the qualitative similarities between the CdTe-Se and CdTe/CdSe spectra are suggestive of similarities in terms of band edge electronic structure.

3.3.2 Analysis of band gap energies using an effective mass approximation model

To examine the observed ligand dependence of the band gap transition energy and to explore the analogy between chalcogenide-capped QDs and core/shell structures, we apply the single band effective mass approximation (EMA) to zinc-blende CdTe-X systems. The single band EMA model is commonly used to analyze band gap energies of QDs. It has previously been applied to quantum dot quantum well systems,[72, 112-113] core/shell nanostructures,[53-54, 73-75, 114-119] and even organic-molecule passivated quantum dots.[38] It has also been used to explain the dependence of photoelectron signal intensity on QD size for QDs in the gas phase,[120] as will be discussed in Chapter 6. In particular, the EMA model has been shown to apply for monolayer shells in core-shell structures,[53, 72-73, 118-119] as thin shell layers can comprise a significant volume fraction of a QD. For example, a 0.2 nm think shell layer on a 2.0 nm radius core represents 25% of the volume of the

composite core/shell structure. Here, we apply the EMA model to spherical core/shell structures where the core is the CdTe QD and the shell is a monolayer of the CdX semiconductor, where X corresponds to the chalcogen ligand (Figure 2.4). The model assumes a neutral particle surface, as may be the case in the presence of counterions or in nanocrystal arrays. This relatively simple model does not describe the intricacies of surface chemistry involved in ligand exchange. Nevertheless, by applying the model typically used to describe core/shell structures to these CdTe-X systems and comparing calculated and experimental band gaps, we can test the hypothesis that chalcogenide-ligand capped QDs behave as core/shell structures.

To carry out the EMA calculations, we followed previously described methods.[72-74] The calculations were described in detail in Chapter 2 of this dissertation. Here, the salient features of the model are discussed. A schematic representation of the relevant physical and energetic parameters is shown in Figure 2.4. We separate the core/shell particle into 3 distinct regions: (1) QD core, (2) ligand shell, and (3) solvent. We treat the photoexcited carriers as particles in spherically symmetric finite potential wells, the barrier heights of which are determined by bulk band potentials. The confinement energy of the carriers (E_e and E_h) is the energy of the carrier in excess of the bulk band potential. Carrier effective masses in each region are defined by the composition: CdTe for the QD core, and either CdS, CdSe, or CdTe for the ligand shell.[121-123] The energetic parameters used to model the MPA layer are estimated based on the reported β value for tunneling through mercapto-carboxylic acids.[124] The potential for the electron is determined by the bulk CB offset (Δ_{CB}) between the core and the shell/solvent. Likewise, the potential for the hole is determined by the bulk VB offset (Δ_{VB}).[125] The structural parameters that serve as inputs to the calculation are the radius of the QD core (r_{QD}) and radius of the QD plus the ligand shell (r_{QD+L}). Values for r_{QD+L} were chosen by adding one-half of the lattice parameter *a* for the cadmium chalcogenide shell layer material (corresponding to one CdX monolayer) to r_{QD}, following literature precedent for describing thin

shell layers.[126] The solvent region is modeled using the relevant parameters for water rather than formamide, as they were more readily found in the literature.[72] This change has a minor quantitative impact on the results of the calculation but no impact on the trends predicted by the model. Dielectric constants for the cadmium chalcogenides,[125] MPA,[105] and water[72] were taken from the literature. The parameters used in our calculations are shown in Table 3.1, and include no adjustable parameters. In conjunction with boundary conditions for r=0, $r=r_{QD}$, $r=r_{QD+L}$ and $r=\infty$,[78-79] the energetic and structural input parameters provide the basis for calculating carrier confinement energies (E_e and E_h), the Coulomb interaction energy (E_c), the expected band gap energy ($E_g^{(QD+L)} = E_g^{(bulk)} + E_e + E_h + E_c$), and wave functions of these systems. We restrict our calculations only to the band edge $1S_e$ and $1S_h$ states. While a multiband approach better models higher energy transitions, both the single- and multi- band models describe band edge states well.[75]

Table 3.1: Input parameters for EMA calculations.

	CdTe	CdSe	CdS	MPA	H_2O
$m_{eff,e}$ (m_0)	0.09	0.11	0.14	1	1
$m_{eff,h}$ (m_0)	0.12	0.44	0.51	1	1
$\Delta_{CB}^{(a)}$ (eV)	0	- 0.42	- 0.10	1.90	2.70
$\Delta_{VB}^{(a)}$ (eV)	0	0.57	0.99	2.99	3.65
shell width (nm)	0.324	0.303	0.291	0.5	n/a
ε_r (ε_0)	7.1	6.25	5.32	2.0	1.8
E_g^{bulk} (eV)	1.61	n/a	n/a	n/a	n/a

(a) Δ_{CB} and Δ_{VB} values are relative to CdTe, with positive values indicating potential barriers for both the electron and hole.

In Figure 3.5 we compare experimentally determined band gap energies with those calculated using the EMA model for a range of CdTe QD radii. Band gap energies determined experimentally (Figure 3.5a) decrease with increasing particle size due to relaxed quantum confinement. Band gap energies also depend strongly on the ligand, in the order CdTe-MPA > CdTe-Te > CdTe-S > CdTe-Se for most of the QD sizes. This ligand dependence is more apparent for smaller CdTe QDs than larger ones. Band gap energies for r_{QD} = 1.34nm CdTe QDs span a range of 250 meV from CdTe-MPA to CdTe-Se, compared to a range of 50 meV for r_{QD} = 2.24nm QDs. The calculated band gap

energies for chalcogenide- and MPA-capped CdTe QDs of various sizes are shown in Figure 3.5b. This model predicts that for all CdTe radii between 1.3 and 4.5 nm, the band gap transition energies order as CdTe-MPA > CdTe-Te > CdTe-S > CdTe-Se. Smaller QDs are predicted to exhibit a wider ligand-dependent band gap range than larger QDs. Calculated band gaps for CdTe QDs with r_{QD} = 1.35 nm have a range of 250 meV (from CdTe-MPA to CdTe-Se) while QDs with r_{QD} = 2.2 nm have a range of 120 meV.

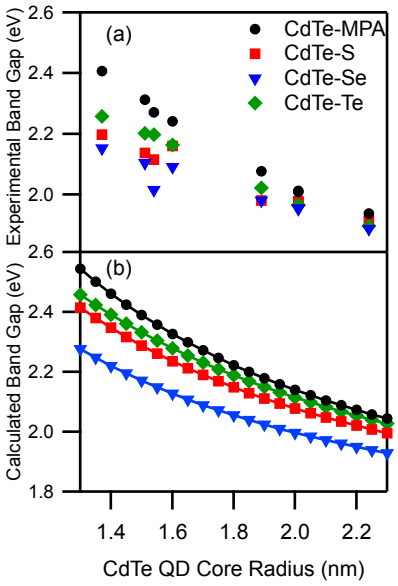

Figure 3.5: Experimental and calculated band gap energies of ligand exchanged CdTe QDs. (a) Experimentally determined band gap energies for various radii of CdTe-MPA (black), CdTe-S (red), CdTe-Se (blue), and CdTe-Te (green) QDs. (b) Band gap energies calculated using the EMA model. Adapted with permission from Schnitzenbaumer, Kyle J.; Dukovic, Gordana. *J. Phys. Chem. C.* **2014**, 118, 28170 – 28178. © 2014 American Chemical Society.

A comparison of the calculated and experimental band gap energies (Figure 3.5) reveals that the EMA model describes the observed trends quite well. We note that no adjustable parameters were used in the calculations and that the ranges of the x and y axes are identical in Figure 3.5a and b. The model, as expected, correctly describes the decrease in band gap energy with increasing CdTe QD radius, due to decreasing quantum confinement. More importantly, the model correctly predicts the energetic ordering of the band gaps as a function of ligand. To obtain the experimental ordering of band gap energies, it is necessary to use CdX effective masses for the ligand shell in the

calculations. Setting carrier effective masses in the ligand shell to those of CdTe for all the chalcogenide ligands leads to the incorrect band gap order CdTe-MPA >> CdTe-S > CdTe-Se > CdTe-Te because the shell thickness increases from S to Te (Figure 3.6a). Setting the effective masses in the ligand shell to the mass of a free electron leads to the same (incorrect) ordering (Figure 3.6b). Moreover, the band gap energy difference between CdTe-MPA and CdTe-Te is up to 600 and 800 meV in Figure 3.6, which is much larger than the experimental range. While the chemical structure of the ligand layer may be more complicated than simply a layer of ordered CdX, the parallels between the calculated and experimentally determined band gaps in Figure 3.5 demonstrate that modeling the CdTe-X systems as QD-core/ligand-shell heterostructures captures key features of chalcogenide-capped QD band edge electronic structure.

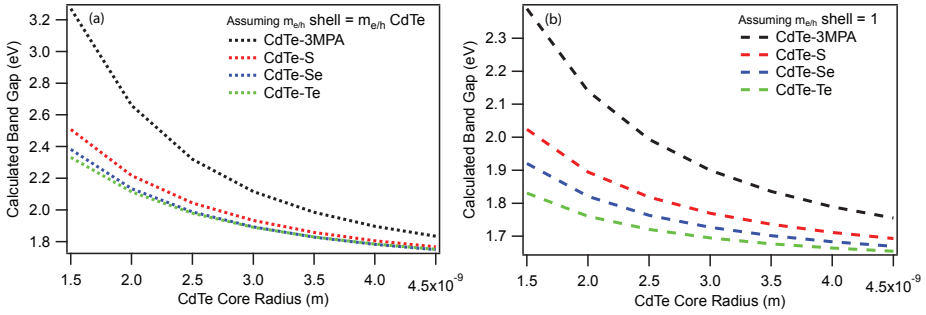

Figure 3.6: Calculated band gap energies using alternative carrier effective masses. Calculated CdTe-X E_g using effective carrier masses of CdTe (a) and electron rest mass (b) in the ligand shell layer. Using the effective masses of CdTe throughout the core/shell structure causes the calculated E_g values to be much higher than observed (Figure 3.5). Using the electron rest mass in the ligand shell layer leads E_g values lower than those observed. Both assumptions lead to a ligand-dependent E_g ordering inconsistent with that observed in Figure 3.5. Adapted with permission from Schnitzenbaumer, Kyle J.; Dukovic, Gordana. *J. Phys. Chem. C.* **2014**, 118, 28170 – 28178. © 2014 American Chemical Society.

3.3.3 Impact of ligands on carrier wave functions

The EMA model allows us to examine how the carrier wave functions are distributed spatially for the different ligand-capping scenarios and to ultimately determine the fraction of the wave function that can be found outside the core/shell structure. The behavior of the carrier wave function in the ligand layer is determined by how the carrier confinement energy $E_{e/h}$ compares to

$\Delta_{CB/VB}$ between CdTe and the ligand layer material. We note that $E_{e/h}$ is constant across the entire core/shell structure due to the strong quantum confinement in these systems. If $E_{e/h}$ does not exceed the potential barrier presented by the ligand shell layer, the carrier wave function will exhibit tunneling behavior and decay exponentially through the ligand shell. The rate at which the wave function decays in the ligand layer depends on the carrier effective mass in the shell as well as the magnitude of the difference between $E_{e/h}$ and $\Delta_{CB/VB}$, with larger differences leading to a more rapid decay. If, however, $E_{e/h}$ exceeds $\Delta_{CB/VB}$, its wave function will extend throughout the ligand layer and begin its exponential decay at the shell-solvent interface.

Figure 3.7 illustrates the effect of the various ligand layers on the CB and VB potentials, electron and hole confinement energies, wave functions, and probability densities for r_{QD}=1.5 nm CdTe-X QDs. Figure 3.7a – d show the electron and hole confinement energies (E_e and E_h) and the potentials of the core, ligand shell, and solvent for CdTe-MPA, CdTe-S, CdTe-Se, and CdTe-Te. Figure 3.7e – h show the electron and hole wave functions and radial probability densities. For CdTe-MPA, the confinement energy of both carriers falls far below the potential barrier presented by the ligand shell and surrounding solvent environment (Figure 3.7a). As a result, the electron (Figure 3.7e and g) and hole (Figure 3.7f and h) wave functions decay exponentially in the ligand-layer shell. For CdTe-S, E_e exceeds the potential barrier of the ligand layer (Figure 3.7b), so that the electron wave function extends into the ligand layer and exponentially decays in the solvent layer (Figure 3.7e and g). E_h is not sufficient to overcome the potential barrier (Figure 3.7b), and the hole decays exponentially in the CdS ligand layer (Figure 3.7f and h). The energetic diagram of CdTe-Se (Figure 3.7c) is similar to that of CdTe-S, but the shell potential barrier for the hole is lower and therefore the hole wave function decays more slowly in the shell (Figure 3.7f and h). Finally, for the case of CdTe-Te (Figure 3.7d), the ligand shell is another layer of the core semiconductor, effectively

resulting in a larger CdTe QD. Thus both carriers delocalize into the shell and begin to exponentially decay at the shell-solvent interface (Figure 3.7e – h).

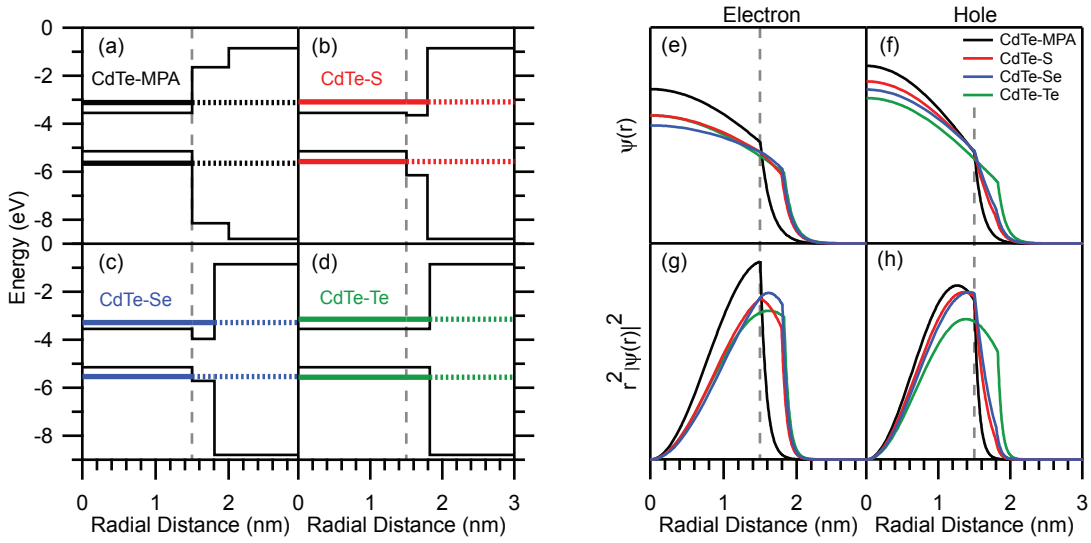

Figure 3.7: Chalcogenide ligand capped CdTe QD wave functions. (a-d) Radial CB and VB bulk potentials (black lines) for r_{QD}=1.5 nm CdTe-X structures and associated calculated electron and hole confinement energies (bold, horizontal lines). Solid bold lines indicate regions where the $E_{e/h}$ exceeds the potential barrier, whereas dotted bold lines indicate regions where $E_{e/h}$ falls below it. (e-h) Calculated electron and hole radial wave functions and probability densities for a CdTe-X QD with r_{QD}=1.5nm. Vertical dashed lines indicate CdTe-ligand layer interface (i.e., r_{QD} in Figure 2.4). The widths of the shell layers are ligand-dependent and therefore are different for all four ligands. Adapted with permission from Schnitzenbaumer, Kyle J.; Dukovic, Gordana. *J. Phys. Chem. C.* **2014**, 118, 28170 – 28178. © 2014 American Chemical Society.

We note that although the bulk band edge alignments of CdTe-S (Figure 3.7b) and CdTe-Se (Figure 3.7c) create a type-II configuration, where the valence and conduction bands are staggered, there is little carrier separation, with the electron-hole overlap integrals of 0.93 for both CdTe-S and CdTe-Se with r_{QD}=1.5 nm. The value of the overlap integral is in agreement with single-band effective mass approximation calculations on similarly sized core/shell CdTe/CdSe.[75] The small shell thickness and overall strong quantum confinement prevent the electron from localizing in the ligand shell, illustrating the importance of both the structural and the energetic parameters in determining carrier overlap.[82, 127-129]

3.3.4 Implications for charge transfer

The extent of carrier delocalization into the surroundings of a QD plays an important role in many applications. Carrier mobility in nanocrystal arrays is proportional to inter-particle electronic coupling,[95, 98, 130] which depends on carrier delocalization outside the particle. In the regime of enhanced coupling, where wave functions from neighboring particles overlap, inter-particle interactions are similar to chemical bonding in extended solids.[98, 131] Band-like transport has been observed in nanocrystal arrays with relatively strong coupling.[95, 98] Similarly, QD-sensitized solar cells and nanocrystal based photocatalytic systems require the transfer of photoexcited charge carriers from nanocrystals, which depends in part on donor-acceptor electronic coupling.[6, 15] By calculating carrier wave functions in CdTe-X systems using the EMA model, we are able to analyze the effect of chalcogenide ligands on the carrier delocalization.

Figure 3.8a shows the probability of finding an electron outside the CdTe-X core/shell structure ($P_{solvent,e}$), as a function of electron confinement energy (E_e) for CdTe-X QD with r_{QD} ranging from 1.5 to 4.5 nm. Figure 3.8b shows the probability of finding a hole outside the core-shell structure ($P_{solvent,h}$) as a function of E_h for the same systems. The size of the QD core decreases with increasing $E_{e/h}$. Because previous work on chalcogenide-capped QDs focused on CdSe, rather than CdTe, we also calculated $P_{solvent,e}$ and $P_{solvent,h}$ as a function of E_e and E_h, respectively, for chalcogenide-capped CdSe QDs (Figure 3.8c and d). The results are very similar to those obtained for CdTe. There are several features of note that are evident for both CdTe and CdSe QDs in Figure 3.8: (i) while the values of $P_{solvent,e}$ and $P_{solvent,h}$ for CdTe-MPA QDs are miniscule (~5 thousandths of a percent), they are in the range of 0.1-6% for chalcogenide-capped QDs. Such relatively high values suggest the potential for enhanced electronic coupling. Improved coupling is reflected experimentally in high carrier mobilities in arrays of CdSe-S QDs[40, 50, 87] and increased power conversion efficiencies of CdSe-S QD sensitized solar cells.[93, 100] (ii) For chalogenide-capped QDs,

the values of $P_{solvent,e}$ and $P_{solvent,h}$ increase several-fold with increasing confinement energies, suggesting that the electronic coupling between chalcogenide-capped QDs and their surroundings will depend on particle size. This is in contrast to QDs capped with aliphatic ligands, where emphasis is placed on the role of particle size in determining energy levels rather than the electronic coupling.[132-133] (iii) While the values of $P_{solvent}$ for electrons do not strongly depend on the chalcogenide ligand (Figure 3.8a), the dependence is noticeable for the holes (Figure 3.8b). For the smallest QDs examined, values of $P_{solvent,e}$ range from 5.2 to 6.1%, but $P_{solvent,h}$ is 0.7% for CdTe-S, 1.1% for CdTe-Se, and 3.7% for CdTe-Te. This is ultimately because the conduction bands of Cd-chalcogenide semiconductors originate from Cd 5s orbitals,[134] making the barrier heights for electrons similar for the three cases. Valence bands, on the other hand, are constructed from chalcogen p orbitals,[134] such that the hole tunneling barrier is tallest in the case of CdTe-S and shortest in the case of CdTe-Te (see Figure 3.7b – d). The predictions in Figure 3.8 are qualitatively consistent with the experimentally measured exciton diameter of CdSe-S QDs with a core radius of 1.4 nm, which was 7% larger than the exciton diameter of octylamine-capped CdSe QDs with the same value of r_{QD}.[135] This analysis demonstrates that EMA modeling of chalcogenide-capped CdTe QDs provides insights that could be used in the design of devices by informing the selection of QD sizes and surface-capping ligands.

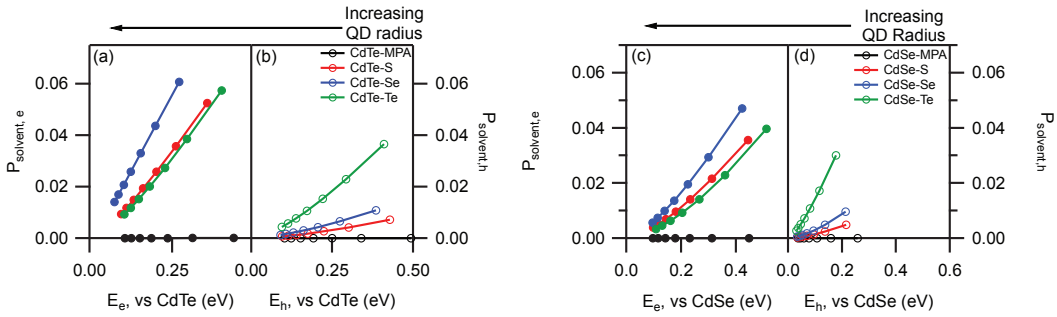

Figure 3.8: Effect of carrier confinement and ligand identity on delocalization. Calculated relationship between the probability of finding the carrier in the surrounding environment, $P_{solvent,e/h}$, and its confinement energy, $E_{e/h}$, for electrons (a) and holes (b) in CdTe-X systems. Displayed traces are for CdTe QDs of radii ranging from 1.5 to 4.5 nm, with higher confinement energies corresponding to smaller QDs. (c, d) $P_{solvent,e/h}$ vs $E_{e/h}$ for CdSe-X QDs of radii ranging from 1.5 – 4.5nm. These values were calculated in the same manner as CdTe-X QDs. Adapted with permission from Schnitzenbaumer, Kyle J.; Dukovic, Gordana. *J. Phys. Chem. C.* **2014**, 118, 28170 – 28178. © 2014 American Chemical Society.

3.4 Conclusions

In this chapter, we described the size and ligand dependence of the band gap energies of CdTe-MPA, CdTe-S, CdTe-Se, and CdTe-Te QDs. We found that modeling chalcogenide-capped QDs as a CdTe QD core surrounded by a thin, semiconducting shell of CdX correctly described the experimentally measured band gap energetic ordering as a function of surface-capping ligand. The agreement between experiment and the model demonstrates that the strongly confined, chalcogenide-ligand capped systems can be treated as core/shell structures with thin shell widths. The application of the EMA model to these systems highlights the changes in QD energy levels and photoexcited carrier wave functions due to the presence of chalcogenide ligands. In contrast to aliphatic ligands, the semiconducting nature of chalcogenide ligands allows for significant delocalization of carrier wave functions outside the QD-ligand structure. The extent of the delocalization depends on both the ligand and the particle size. This analysis provides guidance for the design of devices such as conductive films and solar cells based on chalcogenide-capped nanocrystals.

Chapter 4. Impact of Chalcogenide Ligands on the Photophysics of CdSe QDs*

> "I became gripped by a quiet, unwonted urge to know a little about these matters and to understand how people figured them out. That to me was the greatest of all amazements – how scientists work things out."
>
> - Bill Bryson

4.1 Introduction

The ability to synthetically control the electronic, optical, and surface properties of semiconductor nanocrystals has generated significant interest for their use in optoelectronic devices.[3-4, 21, 83-85] The surfaces of semiconductor nanocrystals are typically passivated with surface-capping ligands that provide colloidal stability in solution. These ligands play an important role in excited state dynamics of nanocrystals because they influence relaxation pathways of photoexcited carriers and their binding to the surface can govern carrier trapping rates at surface sites.[25, 32, 34] For applications that require efficient transfer and collection of photogenerated charge carriers, such as nanocrystal-based photovoltaics, the native long-chain aliphatic ligands used in synthesis serve as insulating barriers that hinder charge transfer and transport.[3, 6, 15] Recent years have seen tremendous

---

* This chapter is adapted with permission from work submitted for publication:

- Schnitzenbaumer, Kyle J.; Labrador, Tais; Dukovic, Gordana. "Impact of Chalcogenide Ligands on Excited State Dynamics in CdSe Quantum Dots" *J. Phys. Chem. C.* In press. Unpublished work © 2015 American Chemical Society.

advancements in the design and implementation of new surface bound species that can replace the native ligands,[4, 35, 37-48] many of which have significantly improved performance of optoelectronic devices.[35-36, 40, 43-44, 47, 49-50, 86-95] Given the importance of surface capping ligands to excited state relaxation, it is important to understand how the new functionalities on the nanocrystal surface impact the dynamics of photoexcited electrons and holes.

Single-atom chalcogenide ligands S^{2-}, Se^{2-}, and Te^{2-} stand in contrast to insulating long-chain ligands in that they create ultra-thin barriers for charge transfer and transport.[45, 50, 95, 136] A number of reports have described the use of chalcogenide-ligand capped nanocrystals in devices with promising results. CdSe QDs capped with S^{2-} ligands have been employed in field effect transistors yielding high electron mobilities with little hysteresis.[40, 50, 87] Solar cells sensitized with CdSe QDs demonstrated faster electron transfer when long chain aliphatic ligands were replaced with S^{2-}. This was attributed to increased rates of electron transfer from the QDs to TiO_2 nanoparticles enabled by the thin ligand shell.[93, 100]

While these reports indicate that chalcogenide ligands can enable relatively high charge transfer rates, little is known about how ligand exchange from native organic ligands to chalcogenide ligands impacts the excited state decay pathways in the nanocrystals. Because the transfer of a photoexcited carrier out of the nanocrystal is in direct competition with relaxation pathways such as carrier trapping, understanding the impact of chalcogenide ligands on nanocrystal photophysics is critical. The use of S^{2-} ligands has been shown to lead to PL quenching of approximately an order of magnitude in comparison to aliphatic ligands.[40, 50] This PL quenching is associated with a significantly decreased PL lifetime in S^{2-} capped CdSe QDs.[50] PL quenching and lifetime shortening are normally a consequence of enhanced trapping rates, but PL does not distinguish between electron and hole trapping. To understand which structural parameters are ultimately important for device design, it is

necessary to understand the relaxation pathways of both electrons and holes in chalcogenide-capped nanocrystals.

In this chapter, we describe the excited state relaxation dynamics of CdSe QDs with a radius of 2.8 nm functionalized with chalcogenide ligands S^{2-}, Se^{2-}, and Te^{2-}. We denote these systems CdSe-S, CdSe-Se, and CdSe-Te, respectively, and compare them with CdSe QDs capped with the native organic ligand n-octadecylamine (CdSe-ODA) and 3-mercaptopropionic acid (CdSe-MPA). We monitor several features in the transient absorption (TA) spectra to follow carrier cooling, trapping of photoexcited holes, and relaxation of band edge electrons. We find that time constants for both electron and hole cooling remain relatively ligand-independent (subpicosecond in all cases). Upon ligand exchange, band edge electron lifetimes are shortened from 11 ns in CdSe-ODA to 3 ns in CdSe-MPA, 2 ns in CdSe-S, and significantly shortened to 70 ps in CdSe-Se and 10 ps in CdSe-Te. We attribute the two order of magnitude decrease in electron lifetime in CdSe-Se and CdSe-Te to fast and efficient electron trapping. Hole trapping follows a different trend, with all ligands exhibiting relatively fast hole trapping (subpicosecond) except for CdSe-Se, which exhibits unusually slow hole trapping (17 ps). By comparing the lifetimes of band edge electrons and trapped holes, we find that the main mechanism for relaxation of the band edge electron in CdSe-MPA and CdSe-S is recombination with a trapped hole. In contrast, in the case of CdSe-Se and CdSe-Te, electron trapping is a much faster process and the main electron relaxation pathway. We conclude our discussion with the implications of this excited state behavior for optoelectronic devices.

4.2 Results

4.2.1 Post-synthetic ligand exchanges

Because of the extensive literature precendent for TA spectroscopy of CdSe QDs capped with native, aliphatic ligands, CdSe QDs are an attractive system for studying the impact of surface ligand modification on QD photophysics.[13, 34] A schematic representation of CdSe QD energy levels is shown in Figure 4.1a. The first three exciton absorption peaks in the typical CdSe QD absorption spectrum are assigned to the 1S(e)–$1S_{3/2}$(h), 1S(e)–$2S_{3/2}$(h), and 1P(e)–$1P_{3/2}$(h) excitons. Following previous work,[68] we refer to these as the X1, X2, and X3 excitons, respectively. To examine the impact of surface-capping ligands on excited state dynamics of CdSe QDs, we perform post-synthetic ligand exchanges on a sample of CdSe-ODA QDs with radii of 2.8 nm. The surface ligands were modified to the chalcogenide ligands S^{2-}, Se^{2-}, and Te^{2-} following ligand exchange procedures developed by Talapin et al.,[40] allowing for solubility in the polar solvent formamide (FA). This work has shown that chalcogenide ligands completely displace aliphatic ligands and allow for stable colloidal nanocrystal solutions.[40] For comparison with an aliphatic ligand that also allows for solubility in FA, a ligand exchange to 3-mercaptopropionic acid (MPA) was performed following previously published procedures.[55-57]

Steady state UV-Vis absorption spectra of CdSe-ODA and the ligand-exchanged samples, are shown in Figure 4.1b. In Chapter 3, we showed that chalcogenide ligands dramatically shift band gap transitions of CdTe QDs (up to 250 meV) due to carrier delocalization into the ligand shell.[136] This effect is considerably smaller in the CdSe QDs investigated here (Figure 4.1b), with the largest red shift being 16 meV between CdSe-ODA and CdSe-Se. This contrast with the behavior of chalcogenide capped CdTe QDs described in Chapter 3 is due to the larger carrier effective masses in CdSe and the relatively large size of CdSe QDs used here. These two differences decrease the extent of carrier confinement and therefore decrease the perturbation of the QD energy levels

induced by different ligand identities. Thus, the energy levels and their energetic spacing depicted in Figure 4.1a are representative of all the CdSe QD samples investigated here.

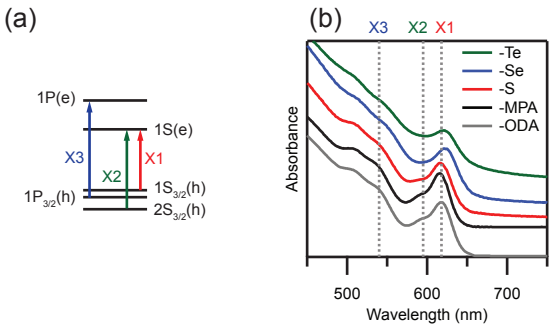

Figure 4.1: Absorption spectra of chalcogenide ligand capped CdSe QDs. (a) Schematic representation of the CdSe QD photoexcited carrier energy levels. The vertical arrows indicate the excitations used in this chapter. (b) Absorption spectra of r = 2.8 nm CdSe-ODA (grey), CdSe-MPA (black), CdSe-S (red), CdSe-Se (blue), and CdSe-Te (green). Dashed vertical lines indicate the wavelengths of the X1, X2, and X3 transitions in each CdSe sample. Adapted from Schnitzenbaumer, Kyle J.; Labrador, Tais; Dukovic, Gordana. *J. Phys. Chem. C.* In press. Unpublished work © 2015 American Chemical Society.

4.2.2 Monitoring photoexcited carriers

In this section, we describe the features in the transient absorption (TA) spectra of CdSe QD that we use to probe the dynamics of 4 processes: (i) cooling of the electron, (ii) cooling of the hole, (iii) relaxation of the electron from the 1S(e) band edge state, and (iv) trapping of the hole from the $1S_{3/2}$(h) band edge state. It is important to note the distinction between the pump pulses that excite exciton transitions X1, X2, and X3 (Figure 4.1a) and the features in the TA spectrum that will be monitored. Figure 4.2a shows the UV-Vis spectrum of CdSe-ODA sample along with the spectra of laser pulses used to generate the X1, X2, and X3 excitons. Figure 4.2b shows a representative TA spectrum of CdSe-ODA 700 fs after X3 photoexcitation. There are three features, denoted in Figure 4.2b as B1, A1, and PA, which we will use to extract carrier dynamics in these samples. TA spectra of all ligand-exchanged samples exhibit similar features, as shown in Figure 4.3. The spectral positions of the features shift slightly based upon ligand identity, in accordance with the small shifts in the steady state absorption spectra (Figure 4.1b). The red shifts of the CdSe-Se and

CdSe-Te spectra reflect the greater degree of carrier delocalization induced by these ligands as demonstrated in Figure 3.8c and d.

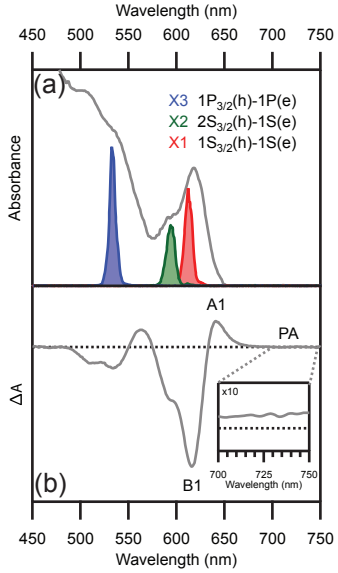

Figure 4.2: Chalcogenide ligand capped CdSe QD TA spectra. (a) Representative pump pulse spectra for X1 (red), X2 (green), and X3 (blue) excitations, plotted along with the steady state UV-Vis absorption spectrum of CdSe-ODA QDs. Similar pump spectra are used in all pump/probe experiments described in this work. (b) Transient absorption spectrum of CdSe-ODA, excited with X3, at a time delay of 280 fs. Some notable features are labeled: B1, which is assigned to photoexcited electrons occupying the 1S(e) state; A1, which is assigned to the absorption of an X1 exciton in the presence of a hot photoexcited carrier; and PA, which is assigned to trapped holes. Adapted from Schnitzenbaumer, Kyle J.; Labrador, Tais; Dukovic, Gordana. *J. Phys. Chem. C.* In press. Unpublished work © 2015 American Chemical Society.

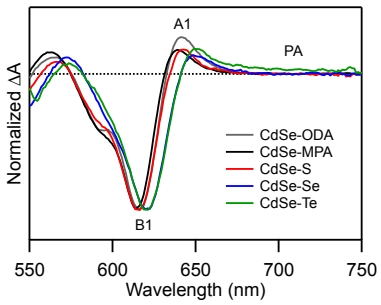

Figure 4.3: Ligand independence of CdSe QD TA spectra. The prominent features in the TA spectra, B1, A1, and PA, remain the same regardless of ligand identity. Their spectral positions shifts slightly based on ligand identity as described in the text. Adapted from Schnitzenbaumer, Kyle J.; Labrador, Tais; Dukovic, Gordana. *J. Phys. Chem. C.* In press. Unpublished work © 2015 American Chemical Society.

Following the literature convention, we refer to the bleach of the band gap transition as B1 (Figure 4.2 and Figure 4.3, ~620 nm).[137] This feature is well established in CdSe QDs to be representative of electron population in the 1S(e) band edge state.[13, 138-139] The A1 feature (occurring

here at ~640 nm, Figure 4.2 and Figure 4.3),[137] arises due to the attractive interaction of the biexciton formed upon band edge absorption of the probe pulse in the presence of a hot exciton.[13] This feature is therefore indicative of a carrier, either electron or hole, which has not yet relaxed (cooled) to the band edge state. The feature labeled PA (observable at all wavelengths red of A1, Figure 4.2b inset) is a broadband photoinduced absorption that has been noted in the literature for CdSe QDs on multiple occasions.[140-143] Through the use of electron (benzoquinone, BQ) and hole (phenothiazine, PTZ) accepting molecules, we confirm Lian et al's assignment of the PA feature's relation to holes.[140] The kinetics of the PA feature of CdSe-ODA QDs exhibit no change in the presence of the electron acceptor benzoquinone (Figure 4.4b). The B1 feature, which corresponds to the band edge electron population, decays more quickly, however, indicating that electron transfer to benzoquinone takes place (Figure 4.4a). In contrast, the PA feature (Figure 4.4d) shows a faster decay in the presence of the hole acceptor phenothiazine, with no evidence of electron transfer in the B1 feature (Figure 4.4c).

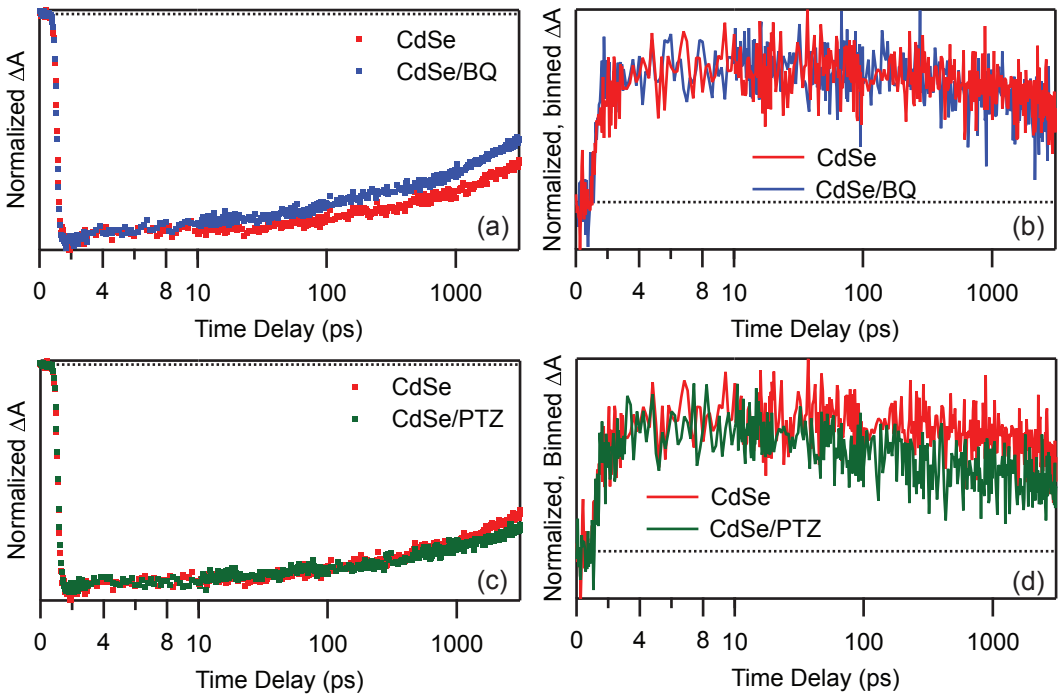

Figure 4.4: Impact of electron and hole acceptors on CdSe-ODA TA kinetics. (a) B1 kinetics with (blue) and without (red) the electron acceptor benzoquinone (BQ). The faster decay of the B1 bleach indicates electron transfer from the CdSe QD to BQ. (b) PA kinetics with (blue) and without (red) BQ. The similarity in the kinetics indicates that electron transfer has no impact on the PA feature. (c) B1 kinetics with (green) and without (red) the hole acceptor phenothiazine (PTZ). Hole transfer occurs from the CdSe QD to PTZ, evidenced by a slightly slower recovery of the B1 kinetics (which monitors 1S(e) electrons) in the presence of PTZ. (d) PA kinetics with (green) and without (red) PTZ. The more rapid decay of the PA feature in the presence of a hole acceptor indicates its relation to holes in CdSe QDs. Adapted from Schnitzenbaumer, Kyle J.; Labrador, Tais; Dukovic, Gordana. *J. Phys. Chem. C.* In press. Unpublished work © 2015 American Chemical Society.

4.2.3 Measurements of electron and hole cooling

In order to examine the ligand dependence of photoexcited carrier cooling, we employ the exciton-selective, state-resolved experimental approach pioneered by Kambhampati et al.[66, 68] This technique allows for determination of the 1P(e) → 1S(e) and $2S_{3/2}$(h) → $1S_{3/2}$(h) cooling rates through the comparison of transient absorption (TA) kinetics following carefully chosen excitation energies. The key ideas behind this experimental approach are displayed in Figure 4.1 and Figure 4.2. Excitation with a pump pulse of energy X1, signified by the red arrow in Figure 4.1a and the red laser spectrum in Figure 4.2a, generates an exciton with both photoexcited carriers in their band edge 1S(e) and $1S_{3/2}$(h) states. Excitation with pump pulse energy of X2, however, signified by the green arrow in Figure 4.1a and green laser spectrum in Figure 4.2b, generates an exciton with the

electron in the 1S(e) state and the hole in the $2S_{3/2}$(h) state. The only difference between X2 and X1 excitation is that X2 produces a hole in the $2S_{3/2}$(h) state rather than the $1S_{3/2}$(h) state. Since the A1 feature corresponds to the presence of a hot carrier, the difference in the decays of the A1 feature following X1 and X2 excitations reveals the cooling of the hot $2S_{3/2}$(h) hole to the band edge $1S_{3/2}$(h) state. Similarly, excitation with pump pulse energy of X3, signified by the blue arrow in Figure 4.1a and blue excitation spectrum in Figure 4.2b, generates an exciton with the electron in the 1P(e) state and the hole in the $1P_{3/2}$(h) state. Since the B1 feature monitors electrons in the 1S(e) state, subtracting B1 kinetics following X1 and X3 excitations reveals the kinetics of electron arrival to the band edge 1S(e) state from the 1P(e) state. Below, we use these methods to determine electron and hole cooling time constants in CdSe QDs as a function of surface capping ligand.

Figure 4.5a – e show the B1 (~620 nm) kinetics for CdSe-ODA, CdSe-MPA, CdSe-S, CdSe-Se, and CdSe-Te following excitation of X1 (red) and X3 (blue) transitions. The differences in the decay kinetics following X1 and X3 excitation occur only at the very early times and are identical after 2 ps. Thus, the kinetics are normalized between 3 and 4 ps. Subtraction of these normalized kinetics yields the state-to-state transition kinetics. Following the notation of Kambhampati et al, we refer to the difference of the kinetics as ΔΔA. The ΔΔA kinetics for the five samples are shown as the black markers in Figure 4.5f – j. These ΔΔA traces are fit (red lines in Figure 4.5f – j) with a single exponential decay convolved with the instrument response function (IRF).

$$\Delta\Delta A(t) = IRF \otimes e^{-(t-t_0)/\tau} \qquad \text{Eqn. 4.1}$$

The time constant for the single exponential decay corresponds to the 1P(e) → 1S(e) relaxation rate (i.e., cooling rate). The 1P(e) → 1S(e) cooling lifetimes for each ligand identity are summarized in the first row of Table 4.1, where the values reflect the average (weighted by the error of the fits) and standard deviation of three measurements on each sample. The values in Table 4.1

reflect the average of three measurements on each sample. With the exception of CdSe-Te, the 1P(e) → 1S(e) cooling lifetimes are in the 100 to 200 fs range for all ligands. For CdSe-Te (Figure 4.5e and j), the B1 kinetics following X1 and X3 excitation exhibit virtually no difference, leading to a ΔΔA trace that can be fit to the same function as our IRF (Chapter 2). We therefore conclude that the ΔΔA time constant for CdSe-Te is faster than our instrumental resolution (~100 fs).

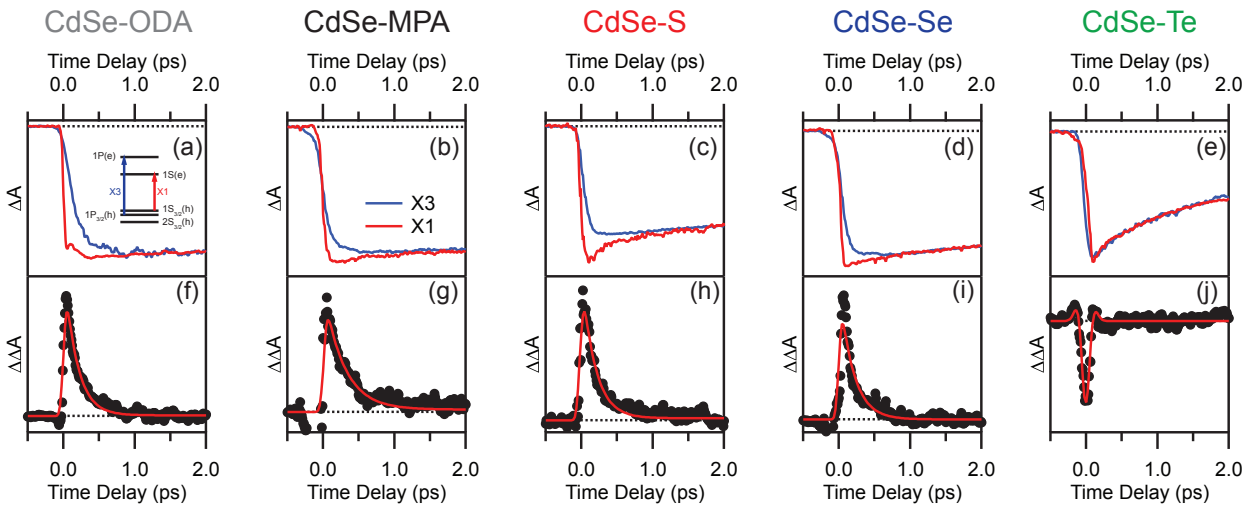

Figure 4.5: Electron cooling in CdSe QDs. (a – e) Normalized B1 (~620 nm) kinetic traces of CdSe-ODA (a), CdSe-MPA (b), CdSe-S (c), CdSe-Se (d), and CdSe-Te (e) following X3 (blue) and X1 (red) excitation. (a, inset) Energy level schematic depicting the experiment performed to measure 1P(e) → 1S(e) relaxation rates. (f – j) ΔΔA trace generated by subtracting the normalized kinetics in the panel above. The red trace is a fit of the data used to extract the 1P(e) → 1S(e) relaxation time constant. Horizontal dashed lines denote ΔA and ΔΔA of zero. Adapted from Schnitzenbaumer, Kyle J.; Labrador, Tais; Dukovic, Gordana. *J. Phys. Chem. C.* In press. Unpublished work © 2015 American Chemical Society.

Table 4.1: Summary of measured time constants. Values represent the average of three separate measurements ± one standard deviation.

	CdSe-ODA	CdSe-MPA	CdSe-S	CdSe-Se	CdSe-Te
1P(e) → 1S(e)[a]	200 ± 50 fs	175 ± 100 fs	200 ± 50 fs	125 ± 75 fs	< 100 fs
1S(e) lifetime[b]	11 ± 4 ns	3 ± 0.2 ns	1.8 ± 0.8 ns	70 ± 10 ps	10 ± 3 ps
$2S_{3/2}(h)$ → $1S_{3/2}(h)$[c]	375 ± 100 fs	225 ± 100 fs	300 ± 75 fs	275 ± 50 fs	125 ± 25 fs
$1S_{3/2}(h)$ → T(h)[d]	525 ± 75 fs	725 ± 125 fs	600 ± 375 fs	17 ± 4 ps	175 ± 50 fs
T(h) lifetime[e]	6 ± 3 ns	3 ± 0.4 ns	1 ± 0.3 ns	20 ± 4 ns	3 ± 3 ns

(a) Measured by state specific pumping of the X3 and X1 transitions.
(b) Average lifetime of the B1 feature calculated using Eqn. 4.2.
(c) Measured by state specific pumping of the X2 and X1 transitions.
(d) T(h) denotes a hole trap state. $1S_{3/2}(h)$ → T(h) lifetimes come from the X1 pumped PA rise time.
(e) T(h) lifetimes come from the decay of the X1 pumped PA feature.
(a) and (c) are the average of 3 trials (weighted by the error of the fits) ± standard deviation. (b), (d), and (e) are the average of 3 trials ± standard deviation.

We apply a similar process for determining the time constants for $2S_{3/2}(h) \rightarrow 1S_{3/2}(h)$ hole cooling. Figure 4.6a – e show the A1 (~640 nm) kinetics for CdSe-ODA, CdSe-MPA, CdSe-S, CdSe-Se, and CdSe-Te following excitation of X1 (red) and X2 (green) transitions. As is done for the $1P(e) \rightarrow 1S(e)$ rate above, the $2S_{3/2}(h) \rightarrow 1S_{3/2}(h)$ cooling rate can be obtained by fitting the difference of these kinetic traces to a single exponential convolved with the IRF (Eqn. 4.1). As above, these kinetics are normalized between delays of 3 and 4 ps and exhibit the same dynamics at all later times. The ΔΔA traces, arising from subtraction of the A1 kinetics following X1 and X2 excitation, and fits are shown in Figure 4.6f – j. From these ΔΔA traces, it is clear that ligand identity does not have a substantial effect on the $2S_{3/2}(h) \rightarrow 1S_{3/2}(h)$ relaxation rate. The $2S_{3/2}(h) \rightarrow 1S_{3/2}(h)$ cooling lifetimes are summarized in the third row of Table 4.1. The hole cooling time constants are somewhat longer than those measured for electron cooling (ranging from 100 to 400 fs) with CdSe-Te again exhibiting the fastest cooling.

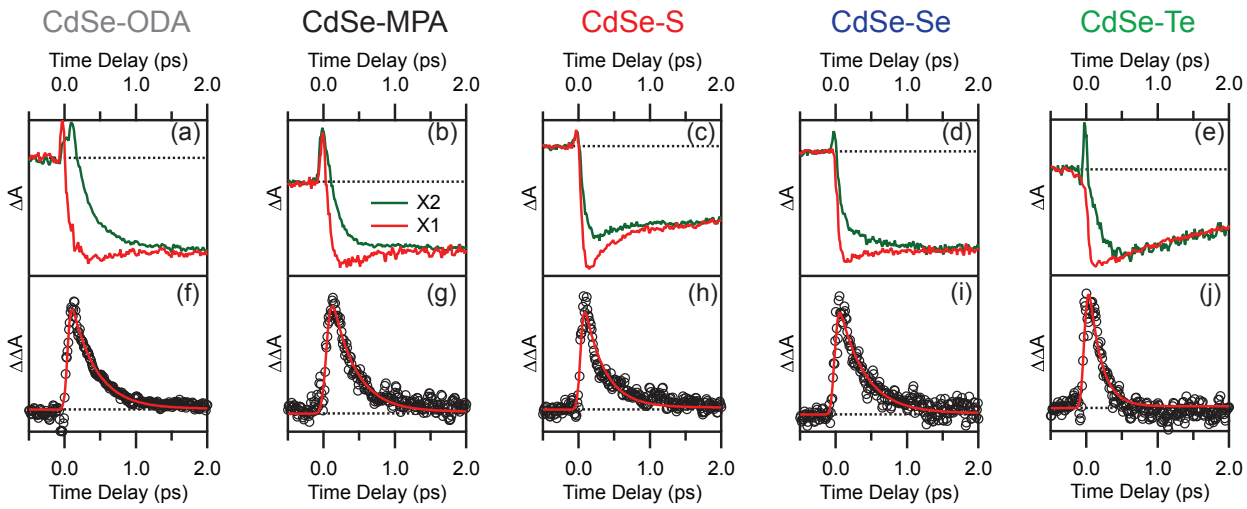

Figure 4.6: Hole cooling in CdSe QDs. (a – e) Normalized A1 kinetic traces of CdSe-ODA (a), CdSe-MPA (b), CdSe-S (c), CdSe-Se (d), and CdSe-Te (e) following X2 (green) and X1 (red) excitation. (f – j) ΔΔA traces generated by subtracting the normalized kinetics in the panel above. The red trace is a fit of the data used to extract the $2S_{3/2}(h) \rightarrow 1S_{3/2}(h)$ relaxation time constant. Horizontal dashed lines denote ΔA and ΔΔA of zero. Adapted from Schnitzenbaumer, Kyle J.; Labrador, Tais; Dukovic, Gordana. *J. Phys. Chem. C.* In press. Unpublished work © 2015 American Chemical Society.

4.2.4 Depopulation of the 1S(e) state

While carrier cooling in CdSe QDs occurs on a subpicosecond timescale, relaxation from the band edge 1S(e) state can occur over a range of timescales, encompassing processes such as radiative and non-radiative electron-hole recombination and electron trapping.[34] The decay of the B1 feature (~620 nm, Figure 4.2b) corresponds to the depopulation of the 1S(e) state, thereby serving as an indication for how long electrons remain in the excited state.[13, 138-139] Monitoring the kinetics after directly exciting the band edge X1 excitonic state prevents any complicating factors that may arise due to carrier cooling. Figure 4.7 shows the B1 decay kinetics of CdSe-ODA, CdSe-MPA, CdSe-S, CdSe-Se, and CdSe-Te following X1 excitation. The kinetics shown in Figure 4.7 exhibit such a strong dependence on ligand identity that we use a logarithmic time axis to show all the decays on one plot. The native ODA-capped CdSe QDs have the slowest 1S(e) decay while the decay of CdSe-MPA is somewhat faster. Ligand exchange to CdSe-S, CdSe-Se, and CdSe-Te results in successively faster decays. The simplest way to compare the ligand-dependence of 1S(e) band edge electron decay is by comparing the average lifetimes, i.e., the average times the electron spends in the 1S(e) state , defined as:[144]

$$\bar{\tau} = \frac{\int_0^\infty t \cdot \Delta A(t)\, dt}{\int_0^\infty \Delta A(t)\, dt} \qquad \text{Eqn. 4.2}$$

To best approximate ΔA(t), we fit each kinetic trace to a triple exponential decay convolved with the IRF. Average lifetimes calculated using Eqn. 4.2 progressively decrease as a function of ligand identity, from CdSe-ODA (11 ns), CdSe-MPA (3 ns), CdSe-S (1.8 ns), CdSe-Se (70 ps) to CdSe-Te (10 ps). The values resulting from triplicate measurements are tabulated in Table 4.1. The value of $\bar{\tau}$ for CdSe-ODA has a particularly large error associated with it because it is larger than the time window of the experiment (3 ns). The average 1S(e) lifetimes for CdSe-ODA (11 ns) and CdSe-MPA (3 ns) measured here agree within the margin of error with the 8.0 ns and 2.6 ns,

respectively, previously reported for phosphonate and MPA capped CdSe QDs.[145] These values demonstrate drastic differences in photoexcited electron decay pathways as a function of ligand identity.

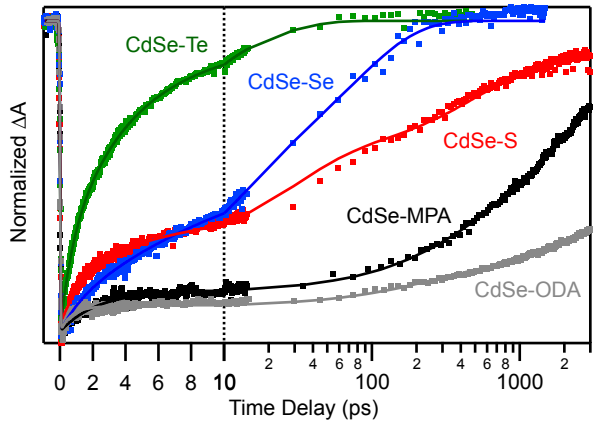

Figure 4.7: Ligand dependence of 1S(e) photoexcited electron decay. B1 kinetics of CdSe-ODA (grey), CdSe-MPA (black), CdSe-S (red), CdSe-Se (blue), and CdSe-Te (green). The x-axis is split into a linear scale for time delays less than 10 ps and a logarithmic scale above. The dashed vertical line marks this split. These traces, which monitor the depopulation of the 1S(e) state, demonstrate the drastically different kinetics depending on the identity of the ligand. Adapted from Schnitzenbaumer, Kyle J.; Labrador, Tais; Dukovic, Gordana. *J. Phys. Chem. C.* In press. Unpublished work © 2015 American Chemical Society.

4.2.5 Measurements of hole trapping

Because TA spectra of CdSe QDs are insensitive to holes in the $1S_{3/2}(h)$ state, we are unfortunately unable to directly monitor relaxation of band edge holes. As described above however, the spectrally broad positive signal in the TA spectra, denoted as PA in Figure 4.2d, is due to holes. Monitoring the kinetics of this feature thus provides insight into the ligand dependence of hole behavior, a relatively uncommon occurrence for TA measurements of cadmium chalcogenide nanocrystals. Since the PA feature is weak, spectrally broad, and its kinetics are identical across the feature, we increase the signal to noise ratio of its kinetics by averaging the kinetics between 700 and 750 nm. Figure 4.8 shows these averaged PA feature kinetics for CdSe-ODA, CdSe-MPA, CdSe-S, CdSe-Se, and CdSe-Te following X1 excitation. Once again, monitoring the kinetics following X1 excitation allows us to avoid complications due the cooling of either carrier. The PA kinetics generally rise quickly, on the subpicosecond timescale. The notable exception to this is CdSe-Se,

which has a significantly slower rise time on the order of tens of picoseconds. The rise time of CdSe-Se and the others, while fast, are longer than the IRF of the experiment (~200 fs at probe wavelengths 700 – 750 nm). Since the $1S_{3/2}$(h) state is directly occupied via X1 excitation, we assign the PA feature to trapped holes. The PA signal then decays relatively slowly. With the exception of CdSe-S, the PA signal does not reach zero inside the 3ns time window of the experiment.

To quantitatively describe these kinetics, we fit the data with a sum of two exponentials, a rise (τ_{rise}) and a decay (τ_{decay}), convolved with the IRF.

$$\Delta A(t) = IRF \otimes \left(-a\, e^{-t/\tau_{rise}} + a\, e^{-t/\tau_{decay}} \right) \qquad \text{Eqn. 4.3}$$

The fits of the data are indicated by the solid traces in Figure 4.8. The time constant for the rise corresponds to hole trapping, while the decay corresponds to the removal of trapped holes. We denote the trapped hole states as T(h). The associated time constants of the rise and subsequent decay are shown in Table 4.1.

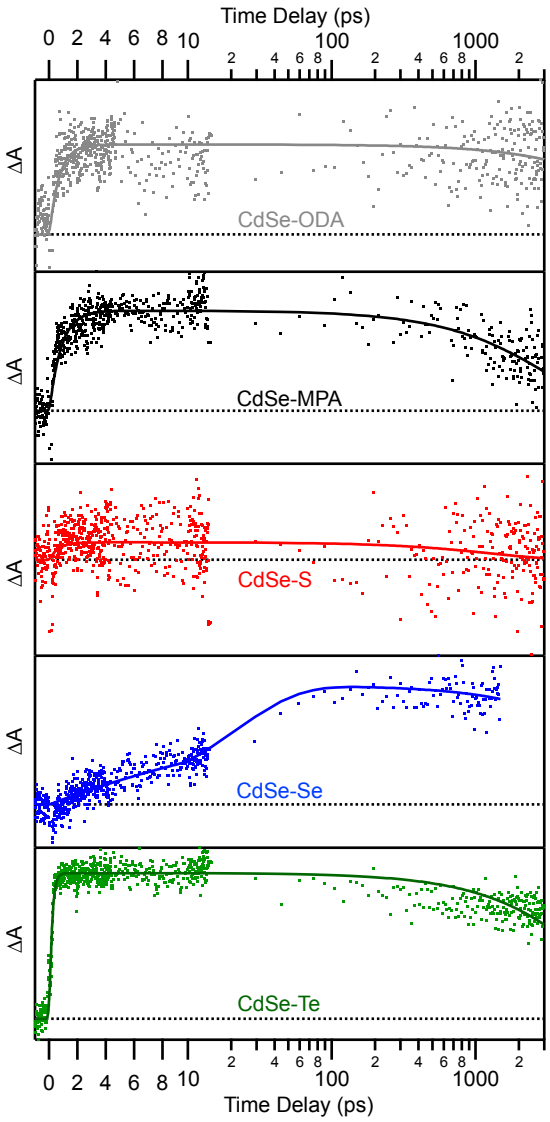

Figure 4.8: Broadband photoinduced absorption kinetics. PA feature kinetics for CdSe QDs passivated with ODA (grey), MPA (black), S (red), Se (blue), and Te (green). A horizontal dashed line indicates ΔA of zero in each panel. The x-axis is split into a linear scale for time delays less than 10 ps and a logarithmic scale above. The colored lines in each panel indicate fits of the data as described by Eqn. 4.3. Adapted from Schnitzenbaumer, Kyle J.; Labrador, Tais; Dukovic, Gordana. *J. Phys. Chem. C.* In press. Unpublished work © 2015 American Chemical Society.

4.3 Discussion

4.3.1 Ligand dependence of carrier cooling

In CdSe QDs, electron cooling occurs primarily through an Auger relaxation mechanism, where the hot electron relaxes by transferring energy to the band-edge hole, creating a hot hole and

band edge electron.[34, 146] This process requires spatial overlap between the electron and hole. Removal of the hole from the valence band state and the subsequent decoupling from the electron via spatial separation of the carriers results in significantly lengthened electron cooling times, up to hundreds of picoseconds.[147-148] The 1P(e) → 1S(e) cooling time constants for CdSe-ODA, CdSe-MPA, CdSe-S, CdSe-Se, and CdSe-Te, determined by the method shown in Figure 4.5, are plotted in Figure 4.9a. The error bars indicate the standard deviation of the three measurements. CdSe-ODA (200 ± 50 fs), CdSe-MPA (175 ± 100 fs), CdSe-S (200 ± 50 fs), and CdSe-Se (175 ± 75 fs) all have similar 1P(e) → 1S(e) relaxation time constants. The notable exception, CdSe-Te, is depicted in Figure 4.9a as shorter than 100 fs, because any time constant longer than 100 fs would have been measureable with our time resolution. We note that our measured time constant for CdSe-ODA is in agreement with that previously reported for CdSe QDs of the same size (r = 2.8 nm).[146] The observation here that electron cooling is largely independent of ligand identity (Figure 4.9a) indicates that both carriers retain significant spatial overlap on the subpicosecond timescale. The unusually fast cooling observed in CdSe-Te will be discussed in Section 4.3.2 below.

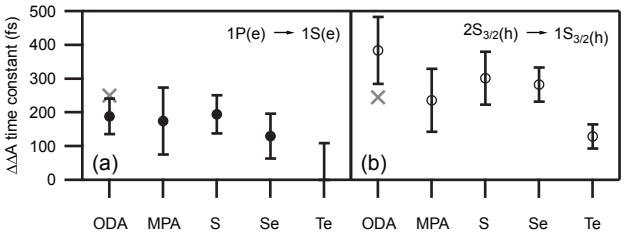

Figure 4.9: Ligand dependence of electron and hole cooling time constants of CdSe QDs. (a) 1P(e) → 1S(e) cooling time constants plotted as a function of ligand identity for r = 2.8 nm CdSe QD. The values are determined by taking a average of three separate experiments, weighted by the error of the fits. Error bars indicate the standard deviation of these measurements. The error bar for CdSe-Te is indicated as reaching as high as 100 fs, as this is the IRF of our measurement. Any slower of a time constant would have been detected. (b) $2S_{3/2}(h) \rightarrow 1S_{3/2}(h)$ relaxation time constants plotted as a function of ligand identity for r = 2.8 nm CdSe QD. The grey X symbols indicates the previously reported values for CdSe-ODA.[146] Adapted from Schnitzenbaumer, Kyle J.; Labrador, Tais; Dukovic, Gordana. *J. Phys. Chem. C.* In press. Unpublished work © 2015 American Chemical Society.

It is thought that hole cooling in CdSe QDs occurs through a combination of energy transfer to ligand vibrational modes, through phonon modes of the QD crystal lattice, and via

processes mediated by surface states.[146, 149-153] The Auger energy loss channel is not accessible to the hole because the energy gap between the $2S_{3/2}$(h) and $1S_{3/2}$(h) levels is smaller than the energetic spacing between the 1P(e) and 1S(e) levels which precludes $2S_{3/2}$(h) hole cooling by exciting an electron. The average hole cooling time constants extracted from the data in Figure 4.6 and associated standard deviations of CdSe-ODA (375 ± 100 fs), CdSe-MPA (225 ± 100 fs), CdSe-S (300 ± 75 fs), CdSe-Se (275 ± 50 fs), and CdSe-Te (125 ± 25 fs) are shown in Figure 4.9b. The previously reported time constant for hole cooling in CdSe-ODA, 250±15 fs, is slightly faster than the range we observe here.[146] For all the samples, hole relaxation is 1.5 to 2 times slower than that of the electron (Figure 4.9a). This is due to the absence of the Auger energy loss channel for hole cooling. Ligand identity does not drastically alter the hole relaxation time constant, with the fast (125 ± 25 fs) time constant of CdSe-Te being the one exception, which will be addressed in Section 4.3.3 below. Replacement of organic surface-capping ligands with chalcogenides removes the cooling channel of energy transfer to the many vibrational modes of the aliphatic ligand. Thus, one might expect the hole cooling in chalcogenide-capped CdSe QDs to be slower than in organic-ligand capped particles. The fact that we do not observe such slowing suggests that cooling through phonon modes or increased importance of surface mediated processes could compensate for the dearth of vibrational modes of the ligands.

4.3.2 Photoexcited electron deactivation

While carrier cooling in CdSe QDs is largely unaffected by ligand identity, relaxation from the band edge states is strongly dependent on which ligand passivates the surface. As observed in Figure 4.7, the lifetime of electrons in the 1S(e) state for the chalcogenide ligands are drastically different than that of the native, aliphatic CdSe-ODA. Strikingly, the average lifetimes of 1S(e) electrons in CdSe-Se and CdSe-Te samples are under 100 ps, compared to several nanoseconds for organic-capped CdSe QDs. For such drastic differences in the 1S(e) lifetime to be observed,

additional deactivation channels must be present. One possibility is an increased number of electron trap sites on the surface. To evaluate this possibility, we analyze the B1 decay using a kinetic model that has been previously used to describe surface trapping in nanocrystalline systems.[154-155] The premise of this model is that each nanocrystal has the same rate constant for electron-hole recombination and electron trapping, but the ensemble of nanocrystals has a distribution in the number of traps per particle, which is described using Poisson statistics. Thus the trapping rate, given by the product of the rate constant and the number of traps, varies among the nanocrystals in the ensemble. To adequately describe the CdSe-S, CdSe-Se, and CdSe-Te B1 kinetic traces using this model, two distinct types of trap states, which we denote type-A and type-B, are necessary. The decay of the B1 signal in Figure 4.7 can then be described with:[154-155]

$$\Delta A(t) = aExp[{}^{-t}\!/_{\tau_{QD}} + m_{tr1}(e^{{}^{-t}\!/_{\tau_{tr1}}}) + m_{tr2}(e^{{}^{-t}\!/_{\tau_{tr2}}})] \qquad \text{Eqn. 4.4}$$

Here τ_{QD} represents the lifetime for trap-independent electron-hole recombination in the CdSe QD, τ_{trA} and τ_{trB} represent the time constants for electron trapping to trap states A and B, respectively, and m_{trA} and m_{trB} represent the average number of trap states type-A and type-B per QD in the ensemble sample. We suppose that ligand exchange to chalcogenide ligands introduces an additional type of electron trap, which has a different trapping rate constant, but that the trapping rate constants do not vary between samples. Rather, the quantity that varies among the samples is the number of traps. Thus, we perform global fitting of the B1 decay of CdSe-MPA, CdSe-S, CdSe-Se, and CdSe-Te simultaneously and require that the time constants for τ_{QD}, τ_{trA}, and τ_{trB} are the same for each sample.

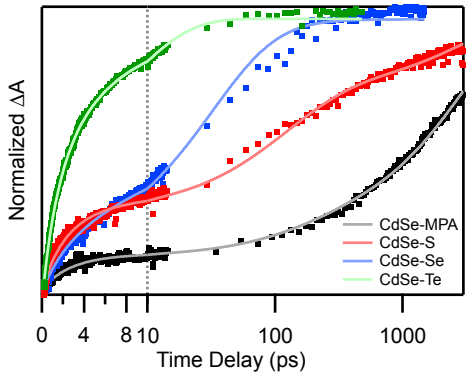

Figure 4.10: Global fits of ligand dependent B1 kinetics in CdSe QDs. Global fits of CdSe-MPA (black), CdSe-S (red), CdSe-Se (blue), and CdSe-Te (green) to the kinetic trapping model presented in Eqn. 4.4. The more rapid decays of the chalcogenide ligand capped CdSe QDs are attributed to increased trapping, as discussed in the text and presented in Table 4.2. Adapted from Schnitzenbaumer, Kyle J.; Labrador, Tais; Dukovic, Gordana. *J. Phys. Chem. C.* In press. Unpublished work © 2015 American Chemical Society.

Figure 4.10 shows the fits to the decay of the B1 kinetics following X1 excitation using Eqn. 4.4. The results of this analysis are presented in Table 4.2. The value of m_{trA} is small (< 1) for each sample and largely ligand-independent. In contrast, the value of m_{trB} varies significantly among the samples, varying from 0.14 for CdSe-MPA to 22 for CdSe-Te. The small value of m_{trB} for CdSe-MPA compared to the other samples is reflective of its relatively negligible contribution to the decay. The large value of m_{trB} for CdSe-Te (22) reflects that this second trapping process is primarily responsible for the short 1S(e) lifetime in CdSe-Te. This analysis suggests that the shortening of the average lifetime of the 1S(e) band edge electron is primarily due to the increased number of the type-B trap. The most likely candidates for at least one type of electron trap are under-coordinated Cd sites on the nanocrystal surface. At this time, the chemical identity of the second trapping site in unknown. We note that the analysis described above is not a unique way of treating the data, as many functions with as many adjustable parameters may fit the data. Rather, this analysis is based on the hypothesis that the decreased average lifetimes of chalcogenide-capped CdSe QDs are caused by increased contribution of electron trapping as a relaxation channel.

Table 4.2: Kinetic model fit parameters. Fit parameters arising from a global fit analysis, using Eqn. 4.4, of the B1 kinetics traces of CdSe-MPA, CdSe-S, CdSe-Se, and CdSe-Te shown in Figure 4.10. The time constants are constrained to be independent of ligand identity. τ_{QD} represents the intrinsic QD decay rate, τ_{trA} and τ_{trB} represent the characteristic time constant to trap states type A and type B, respectively, and m_{trA} and m_{trB} represent the average number of trap states type A and type B per QD, respectively.

	MPA	S	Se	Te
τ_{QD}	2860 ps			
m_{tr1}	0.13	0.35	0.18	0.71
τ_{tr1}	2.71 ps			
m_{tr2}	0.14	0.99	5.5	22.5
τ_{tr2}	183 ps			

This treatment of the B1 kinetics lends some insight into the fast 1P(e) → 1S(e) (< 100 fs) electron cooling in CdSe-Te shown in Figure 4.5e and j and Figure 4.10. It has been reported that electron transfer rates from the 1P(e) state are comparable or faster than those from the 1S(e) state because of a higher driving force.[156] For a similar reason, if electron trapping is fast from the 1S(e) state, it is likely to be as fast or faster from the 1P(e) state. With the large number of traps and the fast 1S(e) depopulation in CdSe-Te observed here, it is possible that electrons in the 1P(e) state could be trapped at a rate that is faster than cooling to 1S(e). Because we monitor the kinetics of the B1 feature, the ΔA, and therefore ΔΔA, traces are monitoring the *arrival* of the electron at the 1S(e) state. Electrons that get trapped directly from the 1P(e) state therefore do not affect the ΔΔA kinetics since they bypass the 1S(e) state. Because of this, we cannot distinguish between a 1P(e) → 1S(e) rate that is faster than our time resolution and the electron trapping from the 1P(e) state outcompeting relaxation to the 1S(e) state. Either of these two circumstances could lead to the observed ΔΔA time constant of <100 fs for CdSe-Te. However, given the relatively ligand-independent electron cooling rates in the other samples (Figure 4.10a), and the high number of electron traps in the CdSe-Te, it is likely that the trapping is faster than cooling in that sample.

4.3.3 Ligand dependence of hole trapping

Figure 4.8 shows the kinetics of the PA feature for CdSe-ODA, CdSe-MPA, CdSe-S, CdSe-Se, and CdSe-Te following X1 excitation. Above, we discussed the experiments used to confirm the previously reported assignment of the PA feature in CdSe QDs to holes.[140] By comparing several aspects of B1 and PA kinetics in the samples described here, we present further evidence that the PA feature cannot be due to electrons and must be assigned specifically to trapped holes. Chalcogenide-capped samples CdSe-Se and CdSe-Te demonstrate that the PA signal cannot be due to the 1S(e) electrons because in those samples the B1 signal is much shorter lived (< 100 ps) than the PA signal (> 1ns) (Figure 4.7 and Figure 4.8). If both features were monitoring electrons in the 1S(e) state, they would have similar kinetics. Similarly, CdSe-ODA, CdSe-MPA, and CdSe-S samples demonstrate that the PA signal cannot be due to trapped electrons because its rise (< 1ps) is much faster than the decay of the 1S(e) populations (> 1ns). If the PA signal were due to trapped electrons, trapping would then be as fast as its rise and therefore very efficient, and 1S(e) populations would be much shorter lived. If the PA feature were due to band edge holes in the $1S_{3/2}(h)$ state, then the rise of its kinetics would be instrument limited following X1 excitation. All samples except CdSe-Te exhibit a rise time slower than the instrument resolution (~200 fs at probe wavelengths 700 – 750 nm), however, precluding valence band holes from being the cause of the PA feature. The fitting parameters τ_{rise} and τ_{decay} in Eqn. 4.3 therefore correspond to the $1S_{3/2}(h) \rightarrow T(h)$ hole trapping time constant and T(h) lifetime, respectively.

The fast $1S_{3/2}(h) \rightarrow T(h)$ trapping in CdSe-Te (175 fs) indicated by the rise of the PA feature in Figure 4.8 also provides some insight into the $2S_{3/2}(h) \rightarrow 1S_{3/2}(h)$ cooling in CdSe-Te. As Figure 4.9b shows, CdSe-Te exhibits hole cooling that is approximately twice as fast as in the other samples. We attribute this increased cooling rate in part to hole trapping in CdSe-Te, which is fast enough to be competitive with $2S_{3/2}(h) \rightarrow 1S_{3/2}(h)$ cooling (125 fs). For the reasons described above,

it is expected that hole trapping from the $2S_{3/2}(h)$ state is comparable or faster than that from the $1S_{3/2}(h)$ state (175 fs). The A1 kinetics, which are sensitive to either carrier being above the band edge, effectively monitor holes in the $2S_{3/2}(h)$ state when the X2 transition is excited. This is in contrast to the electron cooling in CdSe-Te discussed above, where the arrival of electrons at the 1S(e) band edge state is monitored. Here, holes being trapped directly from the $2S_{3/2}(h)$ state, since they decrease the population of the $2S_{3/2}(h)$ state, *do* affect the ΔΔA kinetics. The combination of both trapping and cooling channels depopulating the $2S_{3/2}(h)$ state therefore leads to the unusually fast measured $2S_{3/2}(h) \rightarrow 1S_{3/2}(h)$ rate in CdSe-Te.

4.3.4 Ligand dependence of 1S(e) electron decay pathways

By considering the information about the decay of 1S(e) electrons and hole trapping results discussed above collectively, we can qualitatively map out the ligand-dependence of the primary relaxation pathways for the photoexcited 1S(e) electrons in CdSe QDs. All of the time constants measured in this work, which this section will refer to, are summarized in Table 4.1. Five of these time constants, the 1S(e) lifetime, electron and hole cooling time constants, and hole trapping time scale of CdSe-ODA, as well as the 1S(e) lifetime of CdSe-MPA, agree with prior reports. The remaining 20 have not been previously reported.

For organic-ligand capped CdSe QDs, we observe behavior consistent with previous reports. In native-ligand capped CdSe-ODA, 1S(e) band edge electrons are relatively long-lived (11 ns), hole trapping is relatively fast (subpicosecond), and the trapped hole lifetime (6 ns) is similar to the 1S(e) lifetime. It has been previously shown that such fast hole trapping in organic ligand capped CdSe QDs accounts for 40% of the PL decay,[64] suggesting that the majority of the photoexcited holes are trapped before recombination with the 1S(e) electron. Thus, the primary relaxation mechanism for 1S(e) electrons in CdSe-ODA is likely recombination with a trapped hole, similar to reported behavior in phosphonate-capped CdSe QDs.[140] We observe similar behavior in CdSe-MPA, where

hole trapping is known to be more efficient than in carboxylate or phosphonate-capped QDs,[25, 32] making 1S(e) → T(h) recombination even more prevalent. In fact, the lifetimes of 1S(e) electron and T(h) hole are both 3 ns. Thus, the 3 ns lifetime of both these states in CdSe-MPA is likely representative of 1S(e) → T(h) recombination.

The rate constants in Table 4.1 for CdSe-S are on the order of those observed for CdSe-MPA. Hole trapping from the $1S_{3/2}$(h) state is still subpicosecond. The 1S(e) electron lifetime in CdSe-S is about a factor of two shorter than CdSe-MPA (1.8 ns compared to 3 ns) primarily due to the ten-fold increase in the average number of type-B traps per QD (Table 4.2). The increase in the number of electron traps compared to CdSe-MPA indicates that, in CdSe-S, electron trapping competes with of 1S(e) → T(h) recombination as the primary 1S(e) electron relaxation channel.

CdSe-Se exhibits notably different behavior. $1S_{3/2}$(h) trapping (17 ps) is two orders of magnitude slower than for all the other samples discussed here. Perhaps coincidentally, in this sample the chalcogenide ligand is the same as the chalcogen contained in the QD. The average 1S(e) lifetime is relatively short (70 ps) due to a strong trapping component caused by, on average, 5.5 type-B electron traps per QD. This significant 1S(e) electron trapping is likely to out-compete 1S(e) → T(h) recombination as the dominant electron relaxation pathway. This is supported by a T(h) lifetime (20 ns) that is three orders of magnitude longer than the 1S(e) lifetime, indicating that trapped holes decay through a mechanism other than recombination with band edge electrons.

In the case of CdSe-Te, electron trapping is even more pronounced. As discussed above, trapping is prevalent enough that direct trapping of hot 1P(e) electrons could be competitive with 1P(e) → 1S(e) cooling. The average number of type-B electron traps is very high (22.5), ultimately resulting in a very short average 1S(e) lifetime (10 ps). $1S_{3/2}$(h) → T(h) hole trapping is also faster than it is in the other samples, which also contributes to a shorter time constant for $2S_{3/2}$(h) → $1S_{3/2}$(h) cooling. This convolution of trapping and cooling from the 1P(e) and $2S_{3/2}$(h) states

differentiates CdSe-Te from organic, S^{2-}, and Se^{2-} capped CdSe QDs. T(h) in CdSe-Te remains relatively long lived as 1S(e) electrons decay by trapping rather than recombination with trapped holes.

4.3.5 Implications for device performance

We conclude this discussion by considering the implications of the electron relaxation behavior in chalcogenide-capped CdSe QDs on their use in devices. Literature reports of the use of these ligands for devices focus on the S^{2-} ligand, which we find to have the longest lived band-edge electrons of the chalcogenide ligands. In these devices, electron-hole recombination and electron trapping discussed here are in direct competition with electron transfer out of the QD. In CdSe QD-sensitized solar cells, the electron transfer lifetime from photoexcited CdSe-S QDs to TiO_2 was determined to be 7.6 ns.[100] This value is within the same order of magnitude as the CdSe-S 1S(e) lifetimes measured here (1.8 ns). This comparison suggests that for CdSe-S can be competitive with the other 1S(e) deactivation channels. However, we expect this would not be the case with CdSe-Se and CdSe-Te, based upon their short 1S(e) lifetimes (70 ps and 10 ps, respectively). For electron transfer in a CdSe-Se or CdSe-Te sensitized solar cell to be competitive with the increased trapping pathways, electron transfer rates would have to be roughly 10 – 100 times faster than those measured using CdSe-S. Based on the previous work described in Chapter 3 (Figure 3.8c and d), only a modest increase in k_{et} is likely when using CdSe-Se instead of CdSe-S.[136] Thus, to use CdSe-Se and CdSe-Te in such devices, electron trapping pathways would need to be mitigated synthetically.

Field effect transistors, on the other hand, provide a different picture. Measured electron mobilities in CdSe-S arrays range anywhere from 0.01 to 7 $cm^2\ V^{-1}\ s^{-1}$.[50] On the higher end of this range, these mobilities correspond to an inter-particle hopping rate on the subpicosecond timescale.[95] Such subpicosecond electron transfer rates would be competitive even with the fastest 1S(e) lifetime measured here (10 ps for CdSe-Te). On the lower end, these mobilities correspond to

inter-particle hopping around the hundreds of picoseconds timescale.[95] These electron transfer rates would be competitive only with the longest chalcogenide ligand capped CdSe QD 1S(e) lifetimes measured here (1.8 ns for CdSe-S).

4.4 Conclusions

In this chapter, we described the excited state relaxation dynamics of r = 2.8 nm CdSe QDs functionalized with chalcogenide ligands S^{2-}, Se^{2-}, and Te^{2-}, as well as aliphatic ODA and mercapto-carboxylic MPA ligands, using transient absorption spectroscopy. By monitoring the B1, A1, and PA features, we are able to measure the 1S(e) lifetime, trapped hole lifetime, 1P(e) → 1S(e), $2S_{3/2}$(h) → $1S_{3/2}$(h), and $1S_{3/2}$(h) → T(h) hole trapping time constants. The chalcogenide ligands lead to a decrease in 1S(e) electron lifetime, moderate for S^{2-} and drastic for Se^{2-} and Te^{2-}, which is attributed to an additional electron trapping pathway in these systems. All ligands investigated here induce subpicosecond hole trapping except Se^{2-}, which exhibits unusually slow hole trapping (12 ps). Both electron and hole cooling rates are largely unaffected by ligand identity, except in the case of Te^{2-}, where the electron and hole trapping rates from the 1P(e) and $1S_{3/2}$(h) states, respectively, in CdSe-Te are fast enough to be competitive with carrier cooling.

For CdSe-ODA, CdSe-MPA, and CdSe-S, recombination with trapped holes is the predominant photoexcited electron decay pathway. In CdSe-Se and CdSe-Te, however, electron trapping dominates electron deactivation. In comparison to reported electron transfer rates in QDDSSC, the electron lifetimes measured here indicate that Se^{2-} and Te^{2-} ligands would not be expected to improve performance. For field effect transistors, which exhibit significantly faster electron hopping, the fast electron trapping induced by Se^{2-} and Te^{2-} ligands is not prohibitive.

Chapter 5. Impact of Surface Modification on CdTe QD Photophysics

> "When you make the finding yourself - even if you're the last person on Earth to see the light - you'll never forget it."
>
> - Carl Sagan

5.1 Abstract

This chapter is motivated by the analogy between chalcogenide ligand capped CdTe QDs and CdTe/CdSe core/shell heterostructures introduced in Chapter 3. The focus of this chapter is the exploration of CdTe QD photophysics and the impact of two methods of surface modification: (i) the growth of a thin CdSe shell, and (ii) Se^{2-} ligand exchange. Combined with the band edge energy levels and photoexcited carrier wave functions discussed in Chapter 3, knowledge of these excited state dynamics helps build a more complete photophysical picture. The excited state dynamics of CdTe-ODPA QDs, core/shell CdTe/CdSe heterostructures, and ligand-exchanged CdTe-Se are probed using transient absorption (TA) spectroscopy utilizing the state specific experimental approach outlined in Chapter 4. By selectively exciting particular excitonic states of the QDs, we find that the TA features of our CdTe core QDs should be interpreted in a similar manner as those in CdSe QDs.

Comparisons between TA measurements of core/shell CdTe/CdSe and ligand-exchanged CdTe-Se reveal some notable similarities. Both the core/shell and ligand-exchanged samples have a

significantly shortened excited state electron lifetime when compared to the CdTe-ODPA core QDs. They both also exhibit a noticeable red-shifting of the band edge bleach TA feature as a function of pump-probe delay. The combination of decreased electron lifetime and red-shifting of TA bleach features is suggestive of increased carrier trapping compared to the CdTe core QDs. There are also some notable differences between the CdTe/CdSe and CdTe-Se samples. The intensity of various TA features are quite different, with the TA spectra of the CdTe/CdSe core/shell being very similar to the CdTe core QDs. We also explore the effects of the CdSe shell growth and Se^{2-} ligand exchange on the exciton-phonon coupling of CdTe core QDs. This chapter describes the first observations of exciton-phonon coupling in chalcogenide capped CdTe QDs. While we observe exciton-phonon coupling with the longitudinal optical phonon mode, the chalcogenide ligand exchange effectively turns off exciton coupling to the longitudinal acoustic mode.

5.2 Introduction

Spectroscopic comparisons among CdTe QDs, CdTe/CdSe core/shell heterostructures, and CdTe-Se ligand-exchanged QDs allow for further exploration of the analogy drawn between chalcogenide capped QDs and core/shell structures in Chapter 3. Aside from developing a more complete understanding of the photophysics of these systems, there are two additional motivations for studying CdTe QD systems using the state specific transient absorption approach. As noted in Chapter 3, CdTe exhibits stronger quantum confinement than CdSe due to its smaller electron and hole effective masses. This leads to larger energetic spacing between electron and hole states and therefore increased spectral resolution of steady state and transient features in CdTe compared to CdSe. While there is a solid understanding of CdSe QDs and their TA spectra, there is less agreement about CdTe QDs. CdTe is also a promising material for implementation in devices,[3-4, 157]

and the state specific approach has the potential to help eliminate ambiguities in the interpretation of CdTe TA measurements. This chapter reports the results of our state specific pumped TA measurements on four samples: two sizes of CdTe-ODPA QDs, as well as core/shell CdTe/CdSe heterostructures and ligand-exchanged CdTe-Se QDs. Our findings are discussed within the framework of previous reports.

5.3 Results & Discussion

5.3.1 Steady state absorption

A logical beginning to this discussion is a key result from Chapter 3. Both growing a thin CdSe shell on a CdTe QD and exchanging the native ODPA ligands to Se^{2-} lead to a similar redshift in the band edge absorption. As shown in Chapter 3, treating the CdTe-Se composite as a CdTe/CdSe core/shell structure led to agreement between calculated and experimental band gap energies.[136] Figure 5.1a shows the absorption spectra of Se^{2-} passivated CdTe QDs in formamide (CdTe-Se, blue), CdTe/CdSe-ODPA core/shell heterostructures in hexane (cyan), and r = 1.55 nm CdTe-ODPA QDs (grey) in hexane. Both the ligand exchanged (blue) and core/shell (cyan) samples were synthesized from the r = 1.55 nm QDs (grey). For comparison, Figure 5.1a also includes another size of CdTe-ODPA QDs, r = 2.01 nm, in hexane (black). The sizes of the CdTe QDs were calculated using the spectral position of the first exciton peak and published tuning curves.[52, 102-103] The difference in solvent environment is unavoidable given the drastically different nature of the ligand shells. The shell width of the CdTe/CdSe core/shell particles used here is estimated to be 0.3 nm based on comparison to previously reported CdTe/CdSe absorption spectra.[53, 111] We note that this is a very thin shell, such that no type-II behavior is observed,[53, 111] as discussed in Chapter 3. The

outer layer of the CdTe-Se QD sample is considered to be a similar monolayer of CdSe. Here, a monolayer is defined as a single layer of CdSe (i.e. half a unit cell).

Each of these CdTe-based samples has the electronic structure depicted in Figure 5.1b, which is similar to that of CdSe QDs.[53, 63, 158-161] This leads to the same spectral features, although they occur at different energies due to differences in energetic spacing among the samples. The ground state absorption features of CdTe/CdSe heterostructures, especially with shell widths as thin as those used here, are assigned in a similar manner as CdTe QDs.[53, 159] This general electronic structure (Figure 5.1b) gives rise to the absorption spectra in Figure 5.1a. From lower to higher energies, all samples exhibit a strong band edge excitonic absorption, assigned to the $1S_{3/2}(h)$-1S(e) transition (X1, red arrows), a relatively weak second excitonic absorption, assigned to the $2S_{3/2}(h)$-1S(e) transition (X2, green arrows), and a somewhat stronger third excitonic absorption, assigned to the $1P_{3/2}(h)$-1P(e) transition (X3, blue arrows).

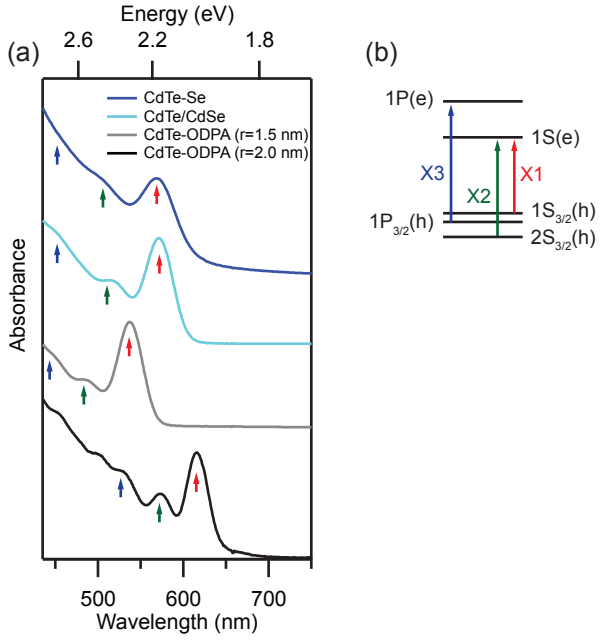

Figure 5.1: QD, core/shell, and ligand exchanged CdTe absorption spectra and energy levels. (a) Steady state absorption spectra of r = 2.01 nm CdTe-ODPA QDs (black), r = 1.55 nm CdTe-ODPA QDs (grey), CdTe/CdSe core/shell heterostructures (cyan), and CdTe-Se ligand-exchanged QDs (blue). The core/shell and ligand-exchanged samples were both prepared from the r = 1.55 nm CdTe-ODPA QD cores. (b) Schematic of CdTe QD photoexcited carrier energy levels and associated excitonic states. The colored arrows in (a) denote the transitions X1 (red), X2 (green), and X3 (blue) depicted in (b).

5.3.2 Interpreting TA spectral features – CdTe QDs

To analyze the excited state behavior induced by CdSe shell growth or Se^{2-} ligand exchange, we must understand the dynamics of the CdTe QDs they are synthesized from. State specific TA experiments were performed on the CdTe-ODPA core sample used for both the shell growth and ligand exchange (Figure 5.2b and d). Since the spectral assignments for CdTe QDs are critical for understanding all the samples discussed in this chapter, we also perform state specific TA experiments on a second sample of CdTe-ODPA QDs of a different size (Figure 5.2a and c).

State specific pumping is a useful experimental technique that significantly aids in the interpretation of TA measurements. As demonstrated with CdSe QDs in Chapter 4, knowledge of a sample's electronic structure coupled with a state specific experimental approach allows for the extraction of intraband relaxation rates. On the other hand, interpreting TA data collected using various pump wavelengths can help determine the electronic structure of a sample. Indeed, this is an approach often employed to elucidate the electronic structure of nanocrystalline heterostructures.[18, 162-163] Though not explicitly referred to as a state-specific approach in these reports, the underlying concept is the same. The combination of TA dynamics, coupled with the knowledge of what absorption feature was initially excited, allows for a more detailed interpretation of the sample's excited state behavior than excitation into the nanocrystal continuum.[67-68]

Employed in this manner, a state specific approach can help us understand the various features in the CdTe-ODPA QDs, and by extension CdTe/CdSe and CdTe-Se QDs, studied here. The basic concept of the experiment is the same as that applied to CdSe QDs in Chapter 4, and is outlined in Figure 5.2a and b. The absorption spectra of two different sizes of CdTe-ODPA, r = 2.01 nm (Figure 5.2a) and r = 1.55 nm (Figure 5.2b), are plotted along with the spectra of the pump pulses used to excite ground state electronic transitions X1, X2, and X3 (Figure 5.1b). The lower panels of Figure 5.2 show the TA spectra of each sample at 150 fs (red), 500 fs (orange), 1 ps

(green), 3 ps (cyan), and 10 ps (blue) following X3 excitation (blue spectra in panels a and b). This series of spectra demonstrates the evolution of the excited state over the first 10 ps following photoexcitation. Notable features that will be discussed below are labeled. The B1 and B2 features are the transient bleaches of the X1 and X2 ground state absorption transitions, respectively, as can be seen by comparing their spectral positions to the associated absorption features in the upper panels. The A1 feature, as noted in Chapter 4, arises from the attractive interaction between an X1 exciton generated by absorption of the probe pulse and a higher energy exciton present due to the pump.[13, 137] Unlike the PA feature in CdSe QDs (discussed in Chapter 4), the mechanism that leads to the broadband photoinduced absorption in CdTe QDs is largely unknown, though various surface trapping processes have been proposed.[63]

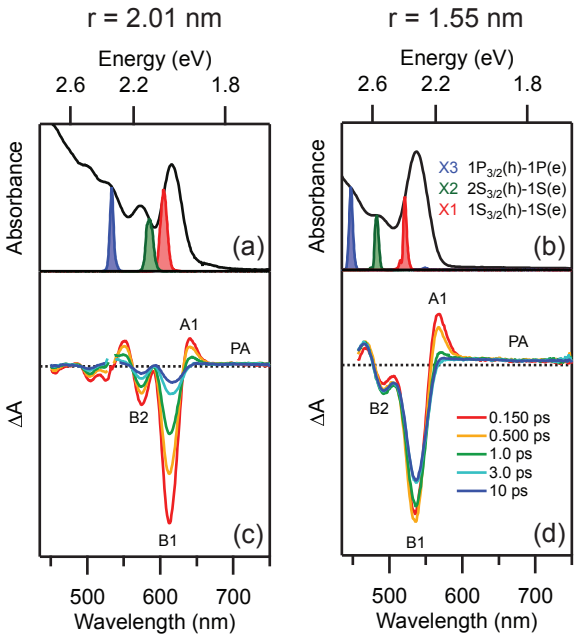

Figure 5.2: CdTe-ODPA absorption and TA spectra. (a – b) Absorption spectra of r = 2.01 nm CdTe-ODPA (a) and r = 1.55 nm CdTe-ODPA (b) plotted with the X1 (red), X2 (green), and X3 (blue) excitation laser spectra for each sample. Each sample has the same general electronic structure, such that while the energy of the X1 – X3 transitions change, the excitonic identities do not. (c – d) Transient absorption spectra of r = 2.01 nm CdTe-ODPA (a) and r = 1.55 nm CdTe-ODPA (b) at delays of 150 fs (red), 500 fs (orange), 1 ps (green), 3 ps (cyan), and 10 ps (blue) following X3 excitation. Notable TA features are labeled for each sample.

We first focus on the TA spectra of the CdTe-ODPA QD samples (Figure 5.2) as they provide the basis for interpreting the CdTe/CdSe core/shell and CdTe-Se ligand exchanged TA

measurements. Both sizes of CdTe QDs exhibit similar TA features, though they occur at different energies. While the assignment of absorption features are well agreed upon, the TA features denoted in Figure 5.2 are interpreted differently in different reports. Some reports treat the TA features of CdTe QDs identically to those in CdS and CdSe QDs.[63] The band edge $1S_{3/2}$(h)-1S(e) bleach (B1) of CdS and CdSe QDs is attributed to electrons in the 1S(e) state and is insensitive to holes in the $1S_{3/2}$(h) state.[13, 164] Reports have shown that the same holds true for the B2 feature.[165] From the perspective of CdS, CdSe, and CdTe being analogous, the band edge bleach of CdTe QDs is therefore expected to monitor the population of the 1S(e) state and contain no information about the $1S_{3/2}$(h) state. Other reports, however, suggest that the B1 feature in CdTe QDs is sensitive to both electron and hole populations, in contrast to what is observed in CdS and CdSe QDs.[158, 160] This conclusion was reached based on the comparison of B1 and B2 kinetics of CdTe QDs, where the early timescale, subpicosecond dynamics of the two features were found to be different. It was postulated that this effect was due to the different effective degeneracies of valence band energy levels near the band edge in CdTe than in CdSe QDs, perhaps because of differences in spin-orbit interactions or crystal symmetry. In both these reports, B1 and B2 kinetics were monitored following 400 nm excitation.

To evaluate which of these interpretations is applicable to the systems studied here, we examine both the B1 and B2 kinetics of the two CdTe-ODPA samples. Rather than exciting at 400 nm, high above the band edge, we excited each sample at its X2 transition as shown in Figure 5.2a and b. The schematic representation of these experiments is shown in the inset of Figure 5.3b. We observe differences between the B1 and B2 kinetics in both sizes of QDs, as shown in Figure 5.3a and b, though the differences between the kinetics depend on the QD size. In the larger, r = 2.01 CdTe QDs (Figure 5.3a), we observe a fairly small difference between the B1 and B2 kinetics. In the smaller, r = 1.55 CdTe QDs (Figure 5.3b), the B2 feature exhibits an apparent grow-in time, which

is in stark contrast to the instrument response limited rise of the B1 kinetics. The fact that we observe different kinetics would seem to imply that the B1 and B2 bleaches probe different states and may therefore be sensitive to holes in the valence band.

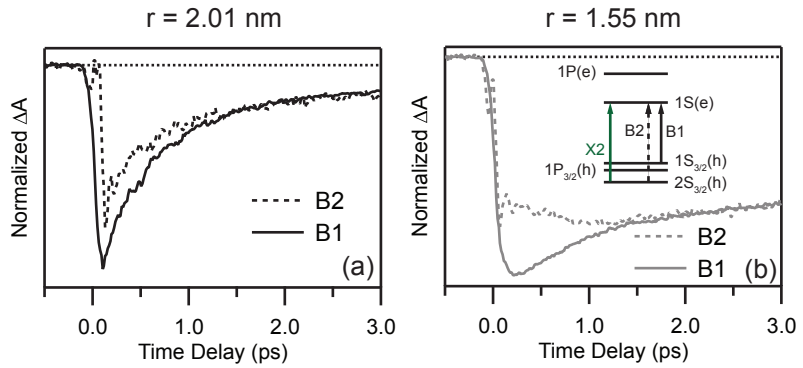

Figure 5.3: Comparison of B1 and B2 kinetics in CdTe-ODPA QDs. (a) Normalized kinetics of the B1 (solid) and B2 (dotted) features of r = 2.01 nm CdTe-ODPA QDs following X2 excitation. (b) The same as a, but for r = 1.55 nm CdTe-ODPA QDs. (inset) Energy level diagram for CdTe QDs denoting the X2 transition excited and the transitions associated with the B1 and B2 bleaches. The instrument limited bleach of the B1 kinetics in both samples following excitation of the $2S_{3/2}$(h)-1S(e) transition indicates that B1 kinetics monitor the population of the 1S(e) state. Horizontal dashed lines indicate ΔA value of zero.

Further consideration on the basis of the specific excitation energy used demonstrates this conclusion to be incorrect. Specifically pumping the X2 transition produces a $2S_{3/2}$(h)-1S(e) exciton. If the B1 and/or B2 bleaches in CdTe TA spectra were sensitive to hole states in addition to electron states, as has been previously proposed,[158, 160] the B2 feature would demonstrate an instrument limited rise since it is a bleach of the transition excited by the pump. A similar rationale would lead us to expect the B1 feature, which is the bleach of the $1S_{3/2}$(h)-1S(e) transition, to exhibit a grow-in time as the hole cools from the $2S_{3/2}$(h) state to the $1S_{3/2}$(h) state. As shown in Figure 5.3, however, we indeed observe the *opposite*, where the B2 kinetics exhibit an apparent grow-in time and the B1 kinetics exhibit an instrument-limited bleach. This indicates that the B1 kinetics of our CdTe QDs are sensitive to electrons in the 1S(e) state and insensitive to holes in the $1S_{3/2}$(h) state, in agreement with the B1 kinetics of CdS and CdSe QDs.

This conclusion does not address why different kinetics are observed for the B1 and B2 features even though they both monitor the population of the 1S(e) state. The fact that these observations are opposite of what we would expect if the B1 and B2 features were sensitive to hole states provides an indication as to the origin of the discrepancy between the B1 and B2 kinetics. As can be seen in Figure 5.2, the intensity of B2 is significantly less than B1 for both sizes of CdTe-ODPA QDs. The B2 feature is also flanked by induced absorption features to both the red and the blue. Between the relatively small signal strength of the B2 feature and its spectral proximity to two induced absorption features, the kinetics of the B2 feature are convolved with other dynamics. This leads to B2 kinetics exhibiting deviations from the "pure" B1 kinetics as seen in Figure 5.3. This effect is more noticeable in the smaller CdTe QDs (Figure 5.3b) because the spectral features are better resolved due to the increased quantum confinement. The increased spectral resolution of the steady state absorption spectrum leads to the increased prevalence of the induced absorption features to either side of B2 in the TA spectrum. We attribute the discrepancy of the B1 and B2 kinetics to the contamination of the relatively weak B2 bleach by these induced absorption signals. Ultimately, we therefore conclude that the CdTe TA spectra should be interpreted in the same manner as that of CdS and CdSe QDs, where the kinetics of the B1 feature represent the populations of the 1S(e) state.

5.3.3 Photophysics induced by CdSe shell growth and Se^{2-} ligand exchange

Understanding how to interpret the CdTe-ODPA QD TA dynamics allows us to analyze the impact of CdSe shell growth and Se^{2-} ligand exchange on CdTe QD photophysics. We apply the state specific approach to these samples in the same manner as described above for the CdTe-ODPA samples. Figure 5.4a – c shows the steady state absorption spectra and associated X1, X2, and X3 excitation pump spectra for r = 1.55 nm CdTe-ODPA core QDs, CdTe/CdSe core/shell heterostructures, and CdTe-Se ligand exchanged QDs. The lower panels of Figure 5.4 show the TA

spectra of each sample at 150 fs (red), 500 fs (orange), 1 ps (green), 3 ps (cyan), and 10 ps (blue) following X3 excitation (blue spectra in panels a – c). Figure 5.4a and d, the spectra associated with r = 1.55 nm CdTe QDs, are identical to Figure 5.2b and d and reproduced here to allow for direct comparison with the core/shell and ligand exchanged QDs.

Many of the same features observed in CdTe QDs are also observed in CdTe/CdSe and CdTe-Se. This is largely expected based upon the thin shell and ligand layers in CdTe/CdSe and CdTe-Se respectively. In combination with the strong quantum confinement exhibited in CdTe QDs, especially as small as the r = 1.55 nm QD cores studied here, these thin shell and ligand layers do not provide a significant enough perturbation to drastically alter the features observed in the TA spectra. While they are observed at different spectral positions than in the CdTe-ODPA cores, due to the effects described in Chapter 3, both the core/shell and ligand exchanged sample exhibit B1, A1, and PA features (Figure 5.4e and f).

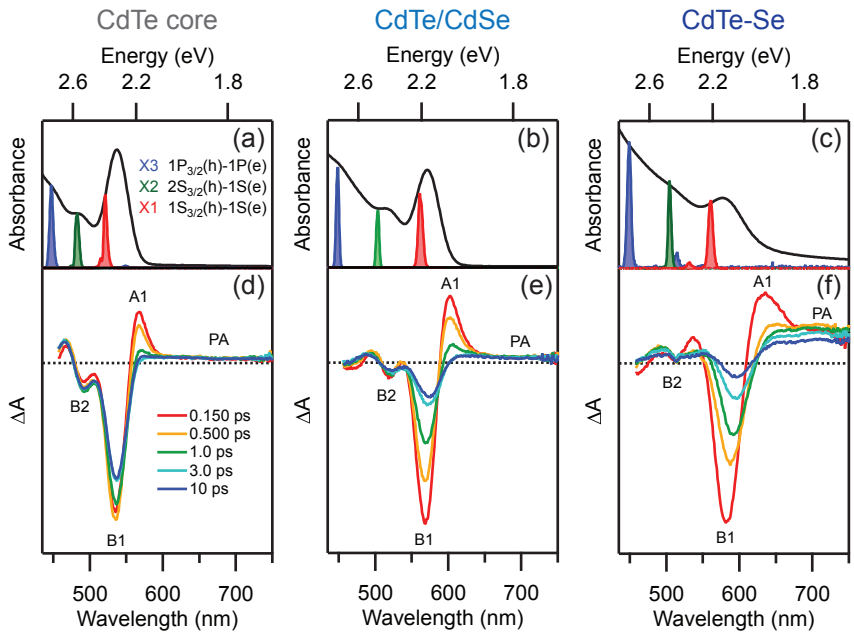

Figure 5.4: CdTe QD, CdTe/CdSe, and CdTe-Se absorption and TA spectra. (a – c) Absorption spectra of r = 1.55 nm CdTe-ODPA QD cores (a), core/shell CdTe/CdSe heterostructures (b), and ligand exchanged CdTe-Se (c) plotted with the X1 (red), X2 (green), and X3 (blue) excitation laser spectra for each sample. Each sample has the same general electronic structure, such that while the energy of the X1 – X3 transitions change, the excitonic identities do not. (d – f) Transient absorption spectra of each sample at pump-probe delays of 150 fs (red), 500 fs (orange), 1 ps (green), 3 ps (cyan), and 10 ps (blue) following X3 excitation. Notable TA features are labeled for each sample.

The thin shell and ligand layers are nevertheless perturbations to the energy levels of CdTe QDs, and lead to some notable differences in the TA spectra of the core/shell and ligand-exchanged samples when compared to the parent CdTe core QDs. In the CdTe-Se ligand exchanged sample (Figure 5.4f) the PA feature is considerably more intense than in the CdTe-ODPA core (Figure 5.4d). The exact mechanism that leads to the PA feature in CdTe is not completely understood, though carrier trapping at the surface has been proposed.[63] Under this interpretation, it would appear that surface trapping is much stronger in CdTe-Se than CdTe or CdTe/CdSe. The indication that the ligand-exchanged CdTe-Se sample exhibits increased trapping is analogous with the increased trapping observed in chalcogenide capped CdSe discussed in Chapter 4.

A particularly intriguing observation in both the CdTe/CdSe (Figure 5.4e) and CdTe-Se (Figure 5.4f) TA spectra is the red-shifting of the B1 feature as a function of delay time. Between pump-probe delays of ~150 fs to 10 ps, the CdTe/CdSe spectra red shift by 6 meV while the CdTe-Se spectra red shift by 26 meV. Red shifts of TA bleach signals as a function of pump-probe delay time in nanocrystalline materials have been reported on multiple occasions.[119, 166-170] In these reports, the red-shifting of TA features is typically attributed to a charge trapping or charge transfer induced Stark effect. The localization of a charge carrier alters exciton energetics via the electric field between the two carriers. As delay time increases, the charge localization process occurs in a greater fraction of the probed sample, thereby gradually shifting spectral position. The observation here of a red-shifting B1 feature thus provides evidence for increased charge trapping in CdTe/CdSe and CdTe-Se compared to the CdTe-ODPA cores.

5.3.4 Measurements of Carrier Cooling

By monitoring the evolution of the TA spectra in Figure 5.2 and Figure 5.4 as a function of pump-probe delay time, we describe the kinetics in CdTe-ODPA QDs, core/shell CdTe/CdSe heterostructures, and ligand exchanged CdTe-Se. We first investigate the intraband relaxation (i.e.

carrier cooling) in each of these samples. The method for measuring the timescales of both the 1P(e) → 1S(e) and $2S_{3/2}(h)$ → $1S_{3/2}(h)$ cooling processes is the same as that employed by Kambhampati et al to extract these time constants in CdSe QDs.[67-68, 143] This technique was used in Chapter 4 and is described there in detail. Briefly, excitation pump pulse energies are chosen to excite particular transitions and subtraction of the resulting kinetics isolates state-to-state population dynamics. For example, subtracting B1 kinetics following X3 and X1 excitation yields the dynamics of 1P(e) → 1S(e) cooling. Similarly, subtracting A1 kinetics following X2 and X1 excitation yields the dynamics of $2S_{3/2}(h)$ → $1S_{3/2}(h)$ cooling.

To extract the 1P(e) → 1S(e) lifetime, we compare the B1 kinetics following X3 (blue) and X1 (red) excitation for CdTe-ODPA, CdTe/CdSe, and CdTe-Se in Figure 5.5a – c. The X3 (blue) and X1 (red) pump spectra used to excite the samples are shown in Figure 5.4a – c. The B1 kinetics following X3 and X1 excitation for each sample agree at all pump-probe delays other than the subpicosecond timescale shown in Figure 5.5 and are therefore normalized at these later delay times. Subtracting the X3 and X1 pumped B1 kinetics of each sample yields the ΔΔA traces in Figure 5.5d – f. The fits (red lines) of the data (black dots) are a single exponential convolved with our instrument response function.

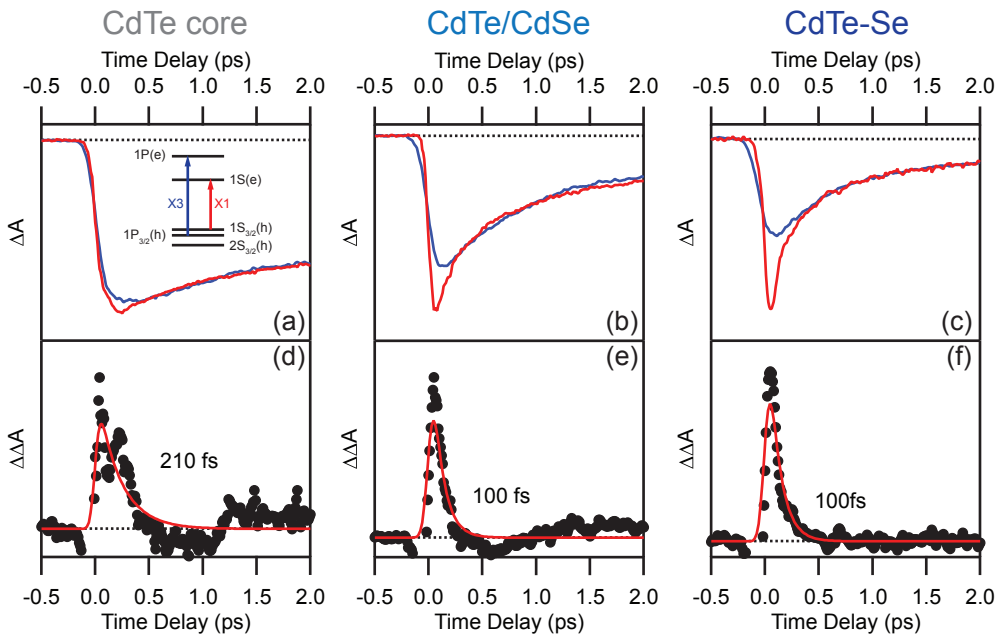

Figure 5.5: Electron cooling in CdTe, CdTe/CdSe, and CdTe-Se. (a – c) Normalized B1 kinetic traces for r = 1.55 nm CdTe-ODPA core QDs (a), CdTe/CdSe core/shell heterostructures (b), and ligand-exchanged CdTe-Se (c) following X3 (blue) and X1 (red) excitation. The B1 kinetics following X3 and X1 excitation differ on the subpicosecond timescale but agree at all later delay times. (a, inset) Energy level schematic depicting the excitonic states excited to generate the B1 kinetics. (d – f) ΔΔA traces obtained by subtracting the normalized kinetics in the above panels. The red trace is a fit of the data used to extract the time constant for 1P(e) → 1S(e) cooling. The horizontal dashed lines represent ΔA and ΔΔA values of zero.

$$\Delta\Delta A(t) = IRF \otimes ae^{-(t-t_0)/\tau} \qquad \text{Eqn. 5.1}$$

The time constant τ extracted from the fits represents the characteristic time constant of 1P(e) → 1S(e) electron cooling. For the CdTe-ODPA QDs (Figure 5.5a and d), we measure an electron cooling time constant of 210 fs. This is in excellent agreement with previously reported values for CdTe QDs.[63, 160] For the core/shell CdTe/CdSe (Figure 5.5b and e) and ligand-exchanged CdTe-Se samples (Figure 5.5c and f), we measure a cooling time constant of 100 fs. These experiments, unlike those described in Chapter 4 for chalcogenide ligand capped CdSe QDs, were not performed in triplicate. It is therefore difficult to assess the error associated with these values. Assuming a similar standard deviation here as the cooling measurements made in Chapter 4 (± 75 fs), the difference in the time constants of electron cooling in CdTe-ODPA QDs (210 ± 75 fs),

CdTe/CdSe core/shell heterostructures (100 ± 75 fs), and ligand exchanged CdTe-Se (100 ± 75 fs) are relatively minimal.

A similar analysis is performed to extract the time constants of $2S_{3/2}(h) \rightarrow 1S_{3/2}(h)$ cooling. To extract the $2S_{3/2}(h) \rightarrow 1S_{3/2}(h)$ lifetime, we compare the A1 kinetics following X2 and X1 excitation for CdTe-ODPA, CdTe/CdSe, and CdTe-Se in Figure 5.6a – c. The X2 (green) and X1 (red) pump spectra used to excite the samples are shown in Figure 5.4b – d. The A1 kinetics following X2 and X1 excitation for each sample agree at all pump-probe delays other than the subpicosecond timescale shown in Figure 5.6 and are therefore normalized at these later delay times. Subtracting the X3 and X1 pumped B1 kinetics of each sample yields the ΔΔA traces in Figure 5.6d – f. The fits (red lines) of the data (black circles) are a single exponential convolved with our instrument response function, as shown in Eqn. 5.1.

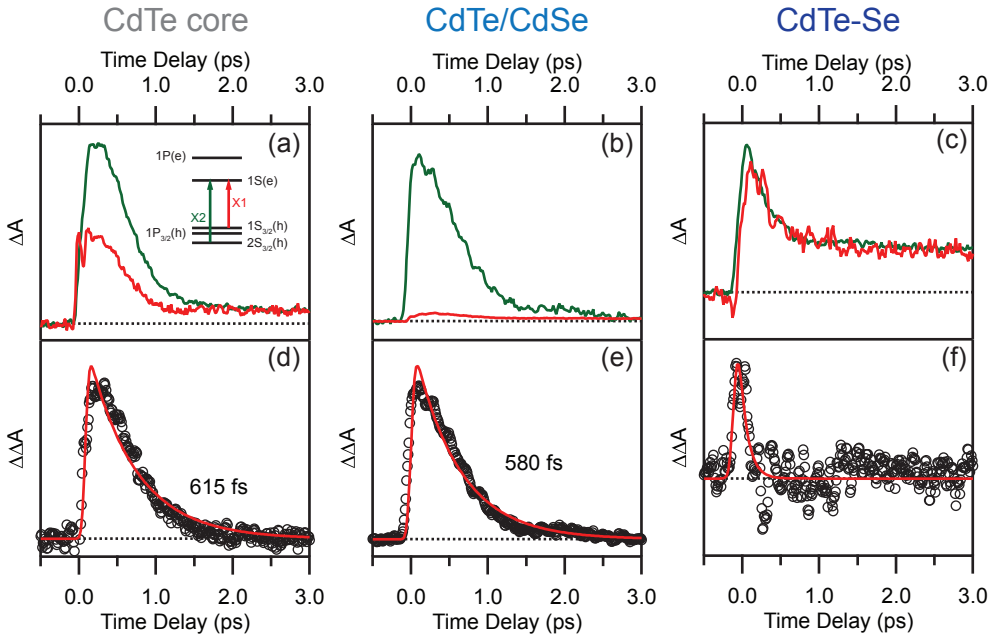

Figure 5.6: Hole Cooling in CdTe, CdTe/CdSe, and CdTe-Se. (a – c) Normalized A1 kinetic traces for r = 1.55 nm CdTe-ODPA core QDs (a), CdTe/CdSe core/shell heterostructures (b), and ligand-exchanged CdTe-Se (c) following X2 (green) and X1 (red) excitation. The B1 kinetics following X2 and X1 excitation agree at all later delay times beyond the window shown here. (a, inset) Energy level schematic depicting the excitonic states excited to generate the A1 kinetics. (d – f) ΔΔA traces obtained by subtracting the normalized kinetics in the above panels. The red trace is a fit of the data used to extract the time constant for 1P(e) → 1S(e) cooling. The horizontal dashed lines represent ΔA and ΔΔA values of zero.

The time constant τ extracted from the fits represents the characteristic time of $2S_{3/2}(h) \rightarrow 1S_{3/2}(h)$ cooling. For CdTe-ODPA QDs (Figure 5.6a and d) and CdTe/CdSe core/shell heterostructures (Figure 5.6b and e), we measure hole cooling time constants of 615 fs and 580 fs, respectively. These values are virtually identical within the error of the measurement (± 75 fs), which we again estimate according to the measurements made in triplicate in Chapter 4. In contrast, the normalized A1 kinetics of CdTe-Se show very similar behavior at all delay times as shown in Figure 5.6c. Therefore the difference between these kinetics is minimal (ΔΔA, Figure 5.6f), consisting of merely a spike at a time delay of zero. The absence of any measurable difference between these kinetics suggest that hole cooling is proceeding faster than our instrumental resolution (~100 fs). Similarly fast ΔΔA dynamics were observed in Chapter 4 for electron cooling in CdSe-Te. Considering this observation coupled with the known importance of hole surface trapping in the early time dynamics of CdTe QDs,[158] it is likely that trapping from the $2S_{3/2}(h)$ state is fast enough to compete with cooling to the $1S_{3/2}(h)$ state. The A1 kinetics used here directly monitor the depopulation of the $2S_{3/2}(h)$ state. Therefore trapping from the $2S_{3/2}(h)$ state would lead to a decreased time constant associated with the ΔΔA trace, as observed in Figure 5.6f.

5.3.5 Photoexcited electron deactivation

There is less consensus about how to interpret each of the TA features in CdTe, and therefore by extension CdTe/CdSe and CdTe-Se, than in CdSe. For this reason it is difficult to extract detailed information about both the electron and hole relaxation dynamics as was done in Chapter 4. Because the PA feature in CdTe QDs in not as well understood as in CdSe QDs, we cannot monitor hole trapping here as we did in Chapter 4. Above, however, we established that the B1 feature of CdTe QDs monitors electrons in the conduction band. We can, therefore, focus on the decay of the 1S(e) photoexcited electron population in the comparison among CdTe cores, CdTe/CdSe core/shell, and CdTe-Se QDs.

The most prominent TA feature for each sample is the B1 bleach (Figure 5.4). This feature shows significantly different kinetics in the first few picoseconds in CdTe, CdTe/CdSe, and CdTe-Se samples, as seen in Figure 5.5a – c (red traces). Figure 5.7 shows the complete decay of the B1 kinetics using a much larger time window, out to 3 ns. All three kinetics are monitored following X1 excitation to eliminate the effects of hot carriers. As can be seen in Figure 5.7, the CdTe/CdSe and CdTe-Se B1 kinetics decay more quickly than those of CdTe. The majority of the deviation from the CdTe kinetics occurs on the picosecond timescale. The kinetics could not be fit using the trapping model used to describe the chalcogenide capped CdSe QDs in Chapter 4 (Eqn. 4.4). Rather, a sum of five exponentials convolved with the instrumental response is used to perform a global fit of all three kinetic traces simultaneously. The time constants, τ_i, used to fit each kinetic trace are forced to be the same across all three samples, and the amplitudes, a_i, are allowed to vary.

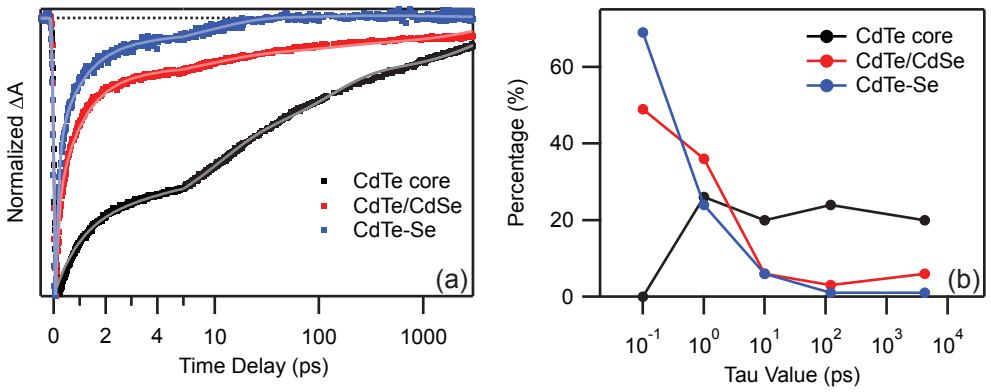

Figure 5.7: CdTe core, CdTe/CdSe, and CdTe-Se B1 kinetics. (a) B1 kinetics (points) and results of a multiexponential global fit analysis (solid lines) where time constants were held the same for each sample. The time axis is linear below 5 ps delay times and logarithmic above in order to display the complete decay kinetics for each sample. (b) a_i values expressed as a percentage of the total decay as a function of their associated time constant. The first two time constants account for at least 85% of the total decay in core/shell CdTe/CdSe and ligand-exchanged CdTe-Se but only account for 25% of B1 decay for CdTe cores. Both the kinetics and their fits show more similarities between CdTe/CdSe core/shell and CdTe-Se than the parent CdTe QD cores.

$$\Delta A(t) = IRF \otimes \sum_{i=1}^{5} \left(a_i e^{-(t-t_0)/\tau_i} \right) \qquad \text{Eqn. 5.2}$$

These resulting fits are shown as the solid traces in Figure 5.7a. The time constants used in the global fit of the three kinetics (0.1 ps, 1 ps, 10 ps, 120 ps, and 4200 ps) span multiple orders of

magnitude. Figure 5.7b shows the a_i values required for fitting each kinetic trace, expressed as a percentage of the decay, plotted as a function of time constant τ_i. The first two time constants, 100 fs and 1 ps, account for more than 85% of the decay in the CdTe/CdSe and CdTe-Se B1 kinetics. This is in stark contrast to the CdTe core QD B1 kinetics, which only has 25% of its decay attributed to the first two time constants. In terms of the depopulation of the 1S(e) state, CdTe/CdSe and CdTe-Se behave more similarly to each other than they do to the parent CdTe core QD. The rapid decay of the B1 bleach in CdTe QDs has been attributed to efficient surface trapping of the electron.[63] We assign the even more rapid recovery of the B1 feature in core/shell CdTe/CdSe and ligand-exchanged CdTe-Se QDs to increased electron surface trapping compared to CdTe-ODPA core QDs.

5.3.6 Exciton-phonon coupling

Up to this point, we have focused on the kinetics of particular TA features. The A1 feature provides insight into hot carrier dynamics, and the B1 feature allows us to monitor electron cooling to and subsequent deactivation from the 1S(e) state. Kinetics at other regions of the probe spectrum, however, also contain useful information. Figure 5.8 shows the evolution of the TA spectra following X1 excitation of CdTe/CdSe core/shell heterostructures from time delays -0.5 to 3.0 ps. The spectral slice at a time delay of 450 fs, plotted at the top of the figure corresponds to the horizontal grey line. This TA spectrum is similar to that following X3 excitation plotted in Figure 5.4e and discussed above. The kinetics at 585 nm, between the B1 and A1 features denoted in Figure 5.4e, are plotted on the right side of Figure 5.8. These kinetics clearly demonstrate modulation of the ΔA signal. The color image demonstrates the modulation of the ΔA signals occurring at a variety of probe wavelengths, visible as faint horizontal bands. These are most prominent to the red and blue sides of the B1 feature (565 nm), where maximum amplitude of the oscillation is observed.[67, 171] The

ability of our experimental setup to trigger these coherent oscillations in QD samples is explained in Section 2.2.4.

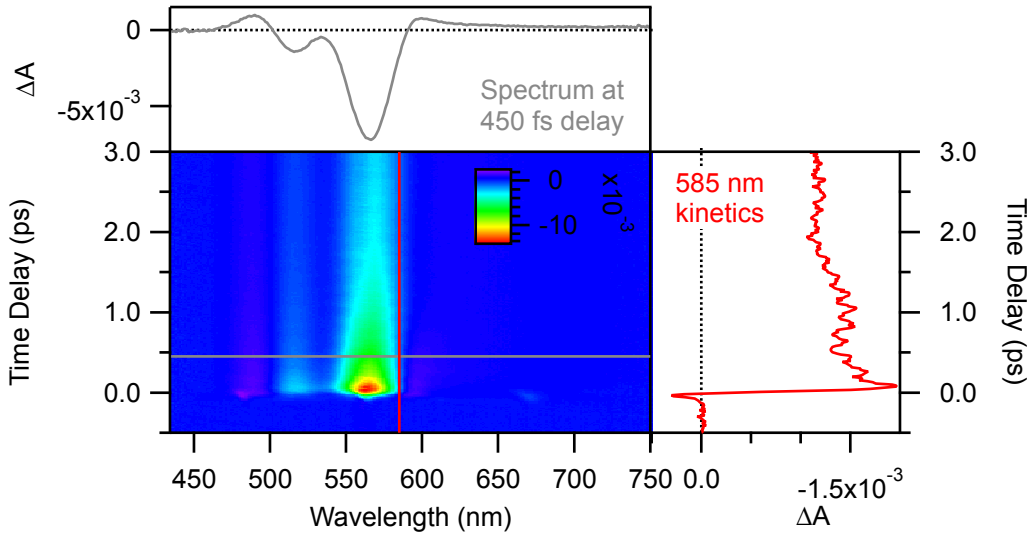

Figure 5.8: Modulation of ΔA signal. Image plot of the TA spectral evolution of CdTe/CdSe core/shell heterostructures following X1 excitation. The upper panel is the TA spectrum taken 450 fs after excitation (grey line). The right panel is the TA kinetics taken at 585 nm (red line), between the B1 (~565 nm) and A1 (~605 nm) features. These kinetics demonstrate clear modulation of the ΔA signal. Dashed lines indicate ΔA of zero.

Closer examination of CdTe core, CdTe/CdSe core/shell, and ligand-exchanged CdTe-Se QD kinetics all reveal coherent oscillations in the measured ΔA signal. Figure 5.9a – c show kinetic traces from the red edge of the B1 feature in each sample. These probe wavelengths are chosen because they demonstrate maximum amplitude of the oscillations.[67, 171] The kinetics are fit to a double exponential function, and the residuals, shown in Figure 5.9d – f, represent the underlying oscillations isolated from the excited state dynamics.[171] To determine the frequency of these oscillations, Fourier transforms of the residuals were performed, resulting in the traces shown in Figure 5.9g – i. The frequencies of these oscillations correspond to the longitudinal acoustic (LA, 20 cm^{-1}) and longitudinal optical (LO, 166 cm^{-1}) phonon modes in CdTe, which are indicated by the vertical dashed lines in Figure 5.9g – i. LO phonons couple to excitons through the Fröhlich interaction, whereby the crystal potentials that determine electronic band energies are modulated through phonon vibrations of a polar crystal.[172-173] These LO phonons arise from the relative

displacement of the positive and negative ions in the crystal lattice. LA phonons couple through the deformation potential, whereby the vibrational displacement of atomic positions leads to a shift in electronic band edges.[172, 174] Due to the exciton-phonon coupling, these kinetics shown in Figure 5.9 follow not only the evolution of the photoexcited state, but also vibrations of the QDs. Figure 5.9c, f, and i represent the first observations of exciton-phonon coupling in chalcogenide capped QDs.

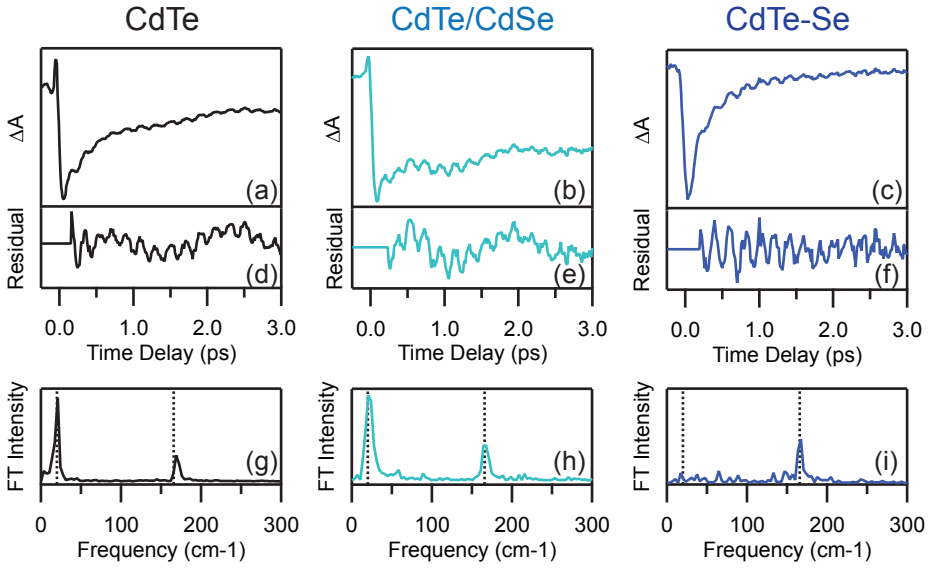

Figure 5.9: Coherent oscillations due to exciton-phonon coupling. (a – c) Kinetic traces from the edge of the B1 bleach feature of CdTe-ODPA (grey), CdTe/CdSe core/shell (cyan), and ligand exchanged CdTe-Se (blue). This spectral region is chosen because it provides the maximum observed oscillation amplitude. Horizontal dashed lines denote zero ΔA. (d – f) Residuals from fitting the kinetics in (a – c) with a double exponential function. The double exponential function describes the excited state dynamics, and thus the residuals isolate the underlying coherent oscillations. (g – i) Fourier transforms of the residuals in d – f. The vertical dashed lines represent the frequencies of the LA (20 cm^{-1}) and LO (166 cm^{-1}) phonon modes in CdTe.

Such coherent oscillations have been previously observed in pump-probe experiments on CdSe and CdTe QDs.[63, 171-172] Exciton-phonon coupling has been studied in CdTe/CdSe core/shell heterostructures as well.[159, 175] The oscillations in the pump-probe transient signal arise from resonant impulsive stimulated Raman scattering (RISRS).[172] When the duration of the pump pulse is short enough, corresponding to less than half a vibrational period,[176] the pulse provides an impulse that initiates the vibration in the ground state. Subsequent absorption is modulated at this vibrational frequency, leading to the observed oscillations in the TA kinetics.

The strength of the coupling between QD phonon modes and excitonic states is still largely debated.[172] In part, this is due to the different results obtained through the various methods of measuring this coupling, which include vibrationally resolved absorption or emission spectroscopies and resonance Raman scattering in addition to the pump-probe technique used here. While the lack of a definitive technique for determining the strength of the exciton-phonon coupling from pump-probe transients precludes us from definitively determining coupling strengths, there are notable benefits to the time-resolved, state specific approach utilized in this chapter. The first is that these experiments were performed in the single exciton regime as discussed in Section 2.2.4. This avoids any exciton-exciton interactions which have proven troublesome to other experimental methods for observing exciton-phonon coupling.[172] Second, we are able to explore exciton-phonon coupling as a function of initial excitonic state dependence using the state specific approach. This approach has previously been applied to CdSe and CdTe QDs,[63, 171] and here we extend it to CdTe/CdSe and CdTe-Se samples.

It is apparent from Figure 5.9g – i that not all samples demonstrate coupling to both LO and LA phonon modes. Figure 5.9i indicates that the TA kinetics of CdTe-Se following X1 excitation are modulated at the LO frequency (166 cm^{-1}) but not the LA frequency (20 cm^{-1}). Since the experiments were performed using X1, X2, and X3 excitation, it is possible to explore the correlation between initial excitonic state dependence and the observation of exciton-phonon coupling. Table 5.1 summarizes the phonon modes observed for CdTe-ODPA, CdTe/CdSe, and CdTe-Se as a function of excitonic state pumped. For both CdTe-ODPA and CdTe/CdSe, we observe LO and LA phonons when pumping the band edge X1 state. Pumping higher energy excitonic states and monitoring the same probe wavelengths as in Figure 5.9, however, leads to the observation of the LA mode only. This finding is in agreement with previous reports for both CdTe and CdSe QDs, where only the X1 exciton couples to the LO phonon mode.[63, 171] For the ligand-

exchanged CdTe-Se sample, the LO mode is observed following X1 excitation, but the acoustic mode is notably absent. In fact, the LA phonon is absent following X1, X2, and X3 excitation. Due to the strict experimental conditions necessary for observing these coherent oscillations (pulse duration less than half vibrational period), their absence in pump-probe kinetics does not necessarily imply the absence of exciton-phonon coupling. Here, however, the LO phonon, with a higher frequency and therefore shorter vibrational period than the LA phonon, requires a shorter pump pulse duration to trigger the RISRS process. Since the LO phonon is observed in X1 pumped CdTe-Se, we can be certain that the observed lack of exciton-LA-phonon coupling is not an experimental artifact, but rather a characteristic of the sample.

Table 5.1: Excitation dependence of observed phonon modes.

	CdTe-ODPA	CdTe/CdSe	CdTe-Se
X1	LO + LA	LO + LA	LO
X2	LA	LA	Neither
X3	LA	LA	Neither

The disappearance of the LA phonon mode upon modification of a sample has been previously reported in CdSe QDs with adsorbed methyl viologen radicals, which act as electron acceptors.[177] In this report, ultrafast electron transfer from the CdSe to the acceptor triggered the observed coherent oscillations. Another report attributes the triggering of LA phonons in CdSe QDs to the piezoelectric potential arising from ultrafast carrier trapping, with the strength of the exciton-phonon coupling directly related to migration of charges to the QD surface.[81] Ultrafast charge transfer and ultrafast charge trapping are similar events, both collapsing a delocalized state into a localized one. These reports seem to suggest that one possible explanation for the lack of LA phonons in CdTe-Se would be the *absence* of carrier trapping. On the basis of the observed rapid decay of the B1 kinetics (Figure 5.7) and prevalence of the PA feature (Figure 5.4) in CdTe-Se QDs discussed above, however, we reject this explanation for why CdTe-Se QD TA kinetics are not

modulated at the LA phonon frequency. Rather, the absence of excitons coupling to LA phonon modes in CdTe-Se suggests that this ligand-exchange process either decreases the exciton-LA-phonon coupling strength to zero or critically damps the acoustic phonon. The fact that a phonon mode associated with the QD material can be turned off or critically damped through surface ligand modification is surprising and warrants further study. Since acoustic phonons are breathing modes of the QD,[174] critical damping of these modes through surface modification could yield important information about the boundary conditions for reflection of the acoustic wave at the QD surface. Further exploration of this system could provide significant insights into how ligand identity affects exciton-phonon coupling and/or acoustic phonon propagation.

5.4 Conclusions and Outlook

The excited state dynamics of CdTe-ODPA QDs, core/shell CdTe/CdSe heterostructures, and ligand-exchanged CdTe-Se were probed using transient absorption (TA) spectroscopy utilizing the state specific experimental approach. With this approach, we find that the B1 feature of our CdTe QDs is insensitive to holes and monitors the band edge 1S(e) state population. CdTe QD TA B1 kinetics should therefore be interpreted in a similar manner as those in CdSe QDs.

We also described some aspects of CdTe QD photoexcited state dynamics which are altered by CdSe shell growth and Se^{2-} ligand exchange. The B1 recovery, indicative of electrons in the 1S(e) state, demonstrate remarkably fast kinetics following surface modification. For both CdTe/CdSe and CdTe-Se, 85% of the decay is attributed to time constants on the subpicosecond to picosecond timescale. In CdTe core QDs, these timescales account for only 25% of the B1 decay. The electron cooling time constants measured for CdTe/CdSe and CdTe-Se 1P(e) → 1S(e) lifetimes are slightly faster than the CdTe-ODPA core QDs. Both the core/shell and ligand-exchanged sample also

exhibit a noticeable red-shifting of the band edge bleach TA feature as a function of pump-probe delay, suggestive of increased trapping in both cases compared to the CdTe core QDs.

The TA spectra of the CdTe/CdSe core/shell are very similar to the CdTe core QDs while those of CdTe-Se exhibit notable differences. The PA feature in CdTe-Se is substantially more intense than the other samples, suggesting enhanced surface trapping similar to that observed in chalcogenide capped CdSe QDs described in Chapter 4. This increased surface trapping is also the likely explanation for faster $2S_{3/2}(h) \rightarrow 1S_{3/2}(h)$ hole cooling in CdTe-Se QDs (<100 fs) compared to CdTe/CdSe and CdTe-ODPA core QDs (600 fs).

We also explored the effects of CdSe shell growth and Se^{2-} ligand exchange on the exciton-phonon coupling of CdTe QDs. While the CdTe QDs and core/shell CdTe/CdSe exhibit $1S_{3/2}(h)$-1S(e) exciton-phonon coupling to both the LA and LO phonon modes for CdTe, only the LO phonon mode is observed following excitation of the $1S_{3/2}(h)$-1S(e) exciton in CdTe-Se. No exciton-phonon coupling to the LA phonon mode is observed in CdTe-Se, indicating that the Se^{2-} ligand exchange either critically damps the longitudinal acoustic phonon mode or turns off exciton-phonon coupling.

The work described in this chapter provides a solid foundation for understanding the excited state dynamics in CdTe-based core/shell heterostructures and chalcogenide ligand capped QDs. In addition, it highlights the benefits of applying state resolved TA to help better understand excited state dynamics in nanocrystal heterostructures. Likewise, understanding the origin of the PA feature in CdTe QDs would allow for more detailed interpretation of both electron and hole dynamics. This can be investigated through monitoring the impact of electron and hole acceptors on TA kinetics, in the same manner as benzoquinone and phenothiazine were used to assign the PA feature of CdSe QDs in Chapter 4. Given the widespread use of CdTe in nanocrystalline heterostructures, further exploration of these CdTe based systems is expected to be both beneficial and fruitful.

Chapter 6. Measuring the Excited State Dynamics of CdSe QD in the Gas Phase*

> "When we try to pick out anything by itself, we find it is tied to everything else in the universe."
>
> - John Muir

6.1 Introduction

This chapter focuses on work performed in collaboration with the Kapteyn-Murnane group in JILA, the joint physics institute between the University of Colorado Boulder and the National Institute of Standards and Technology. There, researchers Dan Hickstein, Jennifer Ellis, and Wei Xiong have developed a unique instrument, the photoelectron velocity map imaging spectrometer, and have used it to study quantum dots in the gas phase. The details of the instrument are provided in Section 6.2 below. My contributions to these research efforts focus on the application of the

---

* This chapter is adapted with permission from the published works:

- Xiong, Wei; Hickstein, Daniel D.; Schnitzenbaumer, Kyle J.; Ellis, Jennifer L.; Palm, Brett B.; Keister, K. Ellen; Ding, Chengyuan; Miaja-Avila, Luis; Dukovic, Gordana; Jimenez, Jose L.; Murnane, Margaret M.; Kapteyn, Henry C. "Photoelectron Spectroscopy of CdSe Nanocrystals in the Gas Phase: A Direct Measure of the Evanescent Electron Wave Function of Quantum Dots" *Nano Letters* **2013**, 13(6), 2924 – 2930. © 2013 American Chemical Society.
- Ellis, Jennifer L.; Hickstein, Daniel D.; Schnitzenbaumer, Kyle J.; Wilker, Molly, B.; Palm, Brett B.; Jimenez, Jose L.; Dukovic, Gordana; Murnane, Margaret M.; Kapteyn, Henry C. "Solvent Effects on Charge Transfer from Quantum Dots" *J. Am. Chem. Soc.* **2015**, 137, 3759 – 3762. © 2015 American Chemical Society.

methods, both theoretical and experimental, outlined in Chapter 2. Similar to the manner in which they were used to investigate chalcogenide ligand capped QD systems in Chapters 3 – 5, these methods are applied to the photoelectron velocity map imaging spectrometer in two ways. (i) A relatively simple theoretical modeling of QDs provided the basis for understanding the QD signals measured by this instrument. This was achieved through the application of the effective mass approximation model to determine the electron wave function in different sizes of CdSe QDs. Comparison of experimentally observed and computationally predicted trends show that the instrument is essentially measuring the evanescent electron wave function of the QD. This work is described in Section 6.3. (ii) Measurements made in the gas phase most notably contrast with those performed in solution phase due to the absence of solvent molecules. Comparison between solution phase transient absorption and the gas phase photoelectron measurements verifies the capability of the photoelectron spectrometer to monitor charge transfer processes in nanoscale systems. It also allows for the exploration of the role solvent molecules play in a charge transfer process. This work is the focus of Section 6.4.

6.2 The Velocity Map Imaging Photoelectron Spectrometer

Photoelectron spectroscopy provides electronic structure information that is complementary to that obtained from transient absorption spectroscopy.[66, 68, 119, 165, 178-181] While a transient absorption experiment probes both the initial state and the final state simultaneously, photoelectron spectroscopy liberates an electron into a plane-wave state, thereby making a direct measurement of only the initial state. Additionally, in photoelectron spectroscopy there are no dark states present as there are in optical spectroscopy.[182-183]

The experimental apparatus consists of a velocity map imaging photoelectron spectrometer[184-185] coupled to a nanoparticle generator and an aerodynamic lens (Aerodyne),[186] which

introduce particles into the interaction region in a high-vacuum chamber[187-188] (Figure 6.1). In order to reach sufficient aerosol concentrations in the high-vacuum chamber, we utilize an aerodynamic lens. Since its invention in 1995,[189] the aerodynamic lens has transformed the field of aerosol and atmospheric sciences by enabling the development of aerosol mass spectrometers,[190-191] which can measure the chemical composition of size-selected particles in the atmosphere. While several previous studies have coupled an aerodynamic lens with a photoelectron spectrometer to study nanoparticles made from dielectric materials such as NaCl[187] and SiO_2,[188] this work represents the first time that an aerodynamic-lens equipped photoelectron spectrometer has been used to study semiconductor nanomaterials and also presents the first *time-resolved* photoelectron spectroscopy of nanoparticles in the gas phase.

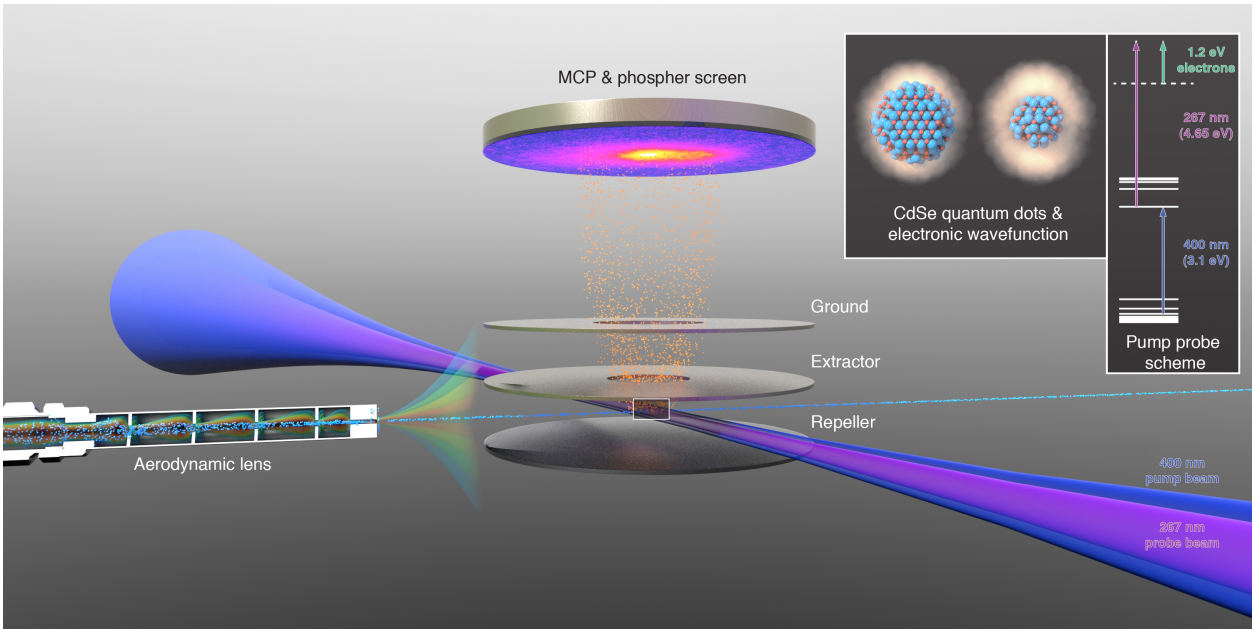

Figure 6.1: Velocity map imaging photoelectron spectrometer setup used for investigations of CdSe QDs in the gas phase. (a) The experimental apparatus consists of a velocity map imaging photoelectron spectrometer coupled to a nanoparticle aerosol source. Clusters of quantum dots (QDs) are focused into the interaction region by an aerodynamic lens, where they are excited and ionized by two time-delayed 40 fs laser pulses. (b) Smaller quantum dots that have been excited to an exciton state have an electronic wave function that extends further outside of the QD and are therefore easier to ionize. (c) In the two-photon photoelectron spectroscopy (PES) experiment, the 400 nm pump pulse excites an electron from the valence band to the conduction band. After a time delay, the 267 nm probe pulse brings the electron into the continuum with ~1.2 eV of kinetic energy. Reproduced with permission from Xiong, Wei; Hickstein, Daniel D.; Schnitzenbaumer, Kyle J.; Ellis, Jennifer L.; Palm, Brett B.; Keister, K. Ellen; Ding, Chengyuan; Miaja-Avila, Luis; Dukovic, Gordana; Jimenez, Jose L.; Murnane, Margaret M.; Kapteyn, Henry C. *Nano Letters* **2013**, 13(6), 2924 – 2930. © 2013 American Chemical Society.

A hexane solution containing the QDs is aerosolized by a compressed-gas atomizer (TSI inc.) with helium gas to form droplets of ~1 μm diameter. The droplets are allowed to dry before entering the aerodynamic lens, leaving behind clusters of quantum dots with diameters of approximately 50 nm. The quantum confined properties of the QDs are well preserved after the aerosol system. The isolation of the individual QDs within the larger clusters indicates that the ligands remain attached to the QDs during the atomization process and subsequent expansion into the vacuum. Both the retention of QD quantum confinement and individual QDs are confirmed through TEM images of QDs collected after passing through the instrument. Effects such as long-lived trap states and optical blinking in quantum dots[192-193] typically require continuously refreshing the interaction volume using flowing or rotating sample cells.[178] Sample degradation is not a problem in this gas-phase experiment, because the particles are flowing through the system and new QDs are used for every measurement. The QD aerosol is collimated to a width of approximately 500 μm by an aerodynamic lens, which creates a nanoparticle beam by passing the QD–helium aerosol through a series of six orifices with decreasing diameters from 5 to 3 mm. The collimated cluster beam is introduced into the first vacuum chamber and then passes through a 1.5 mm skimmer into a separate, differentially pumped, velocity map imaging (VMI) vacuum chamber.[185]

In the two-photon photoelectron experiment, the QDs are first excited by a 400 nm pump pulse (40 fs) and the resulting dynamics are then probed using a 267 nm pulse (40 fs). Both beams are derived from a 1 kHz Ti:sapphire 800 nm laser (KMLabs) using BBO crystals, and the time delay between them is controlled using a Mach–Zehnder interferometer. The power and polarization of each beam is controlled by a half-wave plate and a polarizer. Excitons are generated by the 400 nm pump pulse and the excited QD is ionized by the 267 nm pulse, as shown in the insert on the right of Figure 6.1. The photon flux of the 400 nm beam is set to approximately 0.05 mJ/cm^2, which is well below the single exciton limit for all the quantum dots in this study.[66, 194] The polarization for

both beams is set parallel to the plane of the detector. The photoelectrons are focused onto an MCP/phosphor detector by three electrodes in the standard Eppink–Parker geometry.[184] A CCD camera captures the photoelecton images, which are then reconstructed using the BASEX algorithm of Dribinski and coworkers.[195] We estimate that there are 10^7 particles in our interaction volume, which is a much lower number of particles than that used for other measurements. For instance, transient absorption spectroscopy typically requires 10^{10} particles in the interaction region.[56] This comparison shows that photoelectron spectrosopy can provide excellent sensitivity, which allows for the study of lower concentration samples.

6.3 Effect of QD Size on Photoelectron Signal Strength

6.3.1 Abstract

We present the first photoelectron spectroscopy measurements of quantum dots (semiconductor nanocrystals) in the gas phase. By coupling a nanoparticle aerosol source to a femtosecond velocity map imaging photoelectron spectrometer, we apply robust gas-phase photoelectron spectroscopy techniques to colloidal quantum dots, which typically must be studied in a liquid solvent or while bound to a surface. Working with a flowing aerosol of quantum dots offers the additional advantages of providing fresh nanoparticles for each laser shot and removing perturbations from bonding with a surface or interactions with the solvent. First, we perform a two-photon photoionization experiment to show that the photoelectron yield per exciton depends on the physical size of the quantum dot, increasing for smaller dots. Next, using effective mass modeling, we show that the extent to which the electron wave function of the exciton extends from the quantum dot, the so-called "evanescent electron wave function", increases as the size of the quantum dot decreases. We show that the photoelectron yield is dominated by the evanescent

electron density due to quantum confinement effects, the difference in the density of states inside and outside of the quantum dots, and the angle-dependent transmission probability of electrons through the surface of the quantum dot. Therefore, the photoelectron yield directly reflects the fraction of evanescent electron wave function that extends outside of the quantum dot. This work shows that gas-phase photoelectron spectroscopy is a robust and general probe of the electronic structure of quantum dots, enabling the first direct measurements of the evanescent exciton wave function.

6.3.2 Introduction

Quantum dots (QDs) are one of the fundamental building blocks of complex nanoscale devices, including next-generation solar energy harvesters,[3-6, 17, 196] quantum computers,[197] and nano-electromechanical systems.[198] To effectively design nanoscale systems, a thorough understanding of the electronic coupling between QDs and the substrate material is needed. Electronic coupling between QDs is highly dependent on the overlap between exciton wave functions. The extent of this overlap is dictated by the portion of the exciton wave function that extends outside the physical boundary of QDs[4, 54, 72-73, 119] which we refer to as the "evanescent electron wave function."

Despite the importance of understanding the extent of the exciton wave function in QDs, to date only *indirect* experimental methods have been implemented to measure the delocalization of the exciton states. One method to quantify the exciton delocalization is to measure the shifts of absorption peaks, which provide information about electronic coupling between adjacent QDs,[199-200] allowing the extent of exciton orbital overlap to be inferred in an indirect manner. In other studies, researchers have used ultrafast transient absorption spectroscopy to show that the charge separation rate of Type II core-shell QDs depends on the extent of the evanescent exciton wave functions in the shell portion of the core-shell QDs.[54, 117, 119, 162] However, none of these studies provides a *direct* probe of the evanescent electron wave function.

In this section, we describe the first study of QDs in the gas phase, which isolates the QDs from substrates and solvents and thereby eliminates any effects of external interactions and bonding. We use an aerosol sample of CdSe QDs that is constantly refreshed in the interaction region so that new QDs are used for each laser shot which avoids any effects of sample degradation, such as charging and photo-oxidation.[201-204] This new capability allows us to show that the total photoelectron yield from the QDs is proportional to the fraction of the electron wave function of the exciton that extends outside the QD, thereby making the first direct measurement of the evanescent electron density of the QD exciton. We use ultrafast two-photon photoelectron spectroscopy (PES) to first create an exciton in a QD and then subsequently liberate an electron using a second photon. By using the photoelectron spectrometer described in Section 6.2 and adjusting the time-delay between the two pulses, we can collect angle, energy, and time-resolved photoelectron spectra of the QD excitons. We observe that the total photoelectron yield per exciton is inversely proportional to the size of the QDs. Using effective mass modeling[54, 72-73] described in Chapter 2 and the three-step model of photoemission from bulk material,[182, 205] we demonstrate that the size dependence of the photoelectron yield can be explained by the extent to which the exciton wave function extends from the QD. In this regard, photoemission from QDs is more similar to photoemission from molecules rather than bulk materials. In the future, by using this general approach to better understand the various factors influencing exciton delocalization and coupling, complex nanostructures can be designed for better charge transfer efficiency.

6.3.3 Inverse scaling of photoelectron yield with QD size

For the work discussed in this section, the QD samples used are the octadecylamine capped CdSe QDs (NN-Labs). They were diluted to 0.01 mg/ml under argon using hexane as a solvent, but otherwise used as received. The sizes of the quantum dots (2.3, 2.5, and 2.8 nm) were determined

from the band-edge absorption using the tuning curve provided by the manufacturer, in good agreement with previously published relationships.[52]

The time-resolved PES spectrum from the d = 2.3 nm CdSe QDs (Figure 6.2a) shows a broad peak near 1.2 eV that exists for positive time delays, i.e., when the 400 nm pump pulse precedes the 267 nm probe pulse. This peak does not decay appreciably on the ~100 ps timescale explored in this study. The less intense features at negative time delays, when the probe pulse precedes the pump pulse, are time independent and result from ionization from either the 267 nm or 400 nm beams acting alone. The PES spectra of d = 2.5 nm and d = 2.8 nm QDs show a very similar behavior. A control experiment using only octadecylamine ligands dissolved in hexane demonstrated that the signal from both ligand and solvent molecules is negligible. The sharp peak at zero kinetic energy results from electrons that are first excited to higher energy states near the continuum by the probe pulse, and then ionized by the DC field of the spectrometer,[206] similar to a zero kinetic energy (ZEKE) experiment.

For each size QD, the PES spectrum at positive time delays (Figure 6.2b) shows a peak centered at 1.2 ± 0.1 eV, which, given our probe photon energy of 4.65 eV, corresponds to an exciton state where the electron lies at -3.45 eV with respect to vacuum. Effective mass calculations show that the 1S electron should be bound by -3.4 eV. Therefore, we assign the peak at 1.2 eV to the 1S electron, an assignment that is further substantiated by the long lifetime (>100 ps) of this peak.[165] The notable absence of a distinct peak from the 1P electron state is likely due to the fact that most of the QDs are instead excited to exciton states that involve a 1S electron and a corresponding deeper hole in the valence band.[13, 66, 194, 201] Additionally, a recent report has shown that the photoelectron signal from the 1P electrons appears as a relatively small shoulder on the main photoelectron peak even under resonant 1P pumping conditions.[201] Thus, it is not surprising that we do not resolve a distinct peak resulting from the 1P electrons.

To investigate the difference between single excitons in different diameter QDs, we measured the PES spectra of 2.3, 2.5, and 2.8 nm diameter quantum dots under the same experimental conditions. We then normalized the PES spectra by the average number of excitons generated in each sample. To avoid multiple carrier generation from an overly intense pump pulse, we set the pulse intensity such that less than 10 percent of the dots absorb a photon from the pump pulse. The normalized PES spectra per exciton ($I_{PE\ per\ exciton}$) is then calculated as

$$I_{\text{PE per exciton}} = \frac{I_{PE}}{N_{QD} \cdot \sigma \cdot P} \qquad \text{Eqn. 6.1}$$

where I_{PE} is the experimental PES spectrum, N_{QD} is the number density of the quantum dots in solution (which can be calculated from ultraviolet-visible spectra), P is the pump photon flux, and σ is the absorption cross-section of the quantum dots.

As shown in Figure 6.2b, the intensities of the PES spectra decrease as the diameter of the QDs increases from 2.3 to 2.8 nm. For QDs with diameters larger than 2.8 nm, the signal cannot be resolved from the noise level. The shift of the 1S peak due to the energy shift of the band gap is expected to be between 0.1 to 0.2 eV, and cannot be resolved in these spectra because the 1S peak is broadened to ~1.5 eV. There are several factors that could contribute to the broadening of the photoelectron spectral peak, including the size inhomogeneity of the sample as well as the presence of secondary electrons that arise from inelastic scattering.[205] However, we should not experience broadening from charged quantum dots, as has been observed in thin film samples,[201, 207] because each laser shot interacts with a new sample of quantum dots. In the future, the secondary photoelectrons that arise due to electron-electron and electron-phonon scattering could be mitigated by using extreme ultraviolet high harmonics as a higher energy probe.[208]

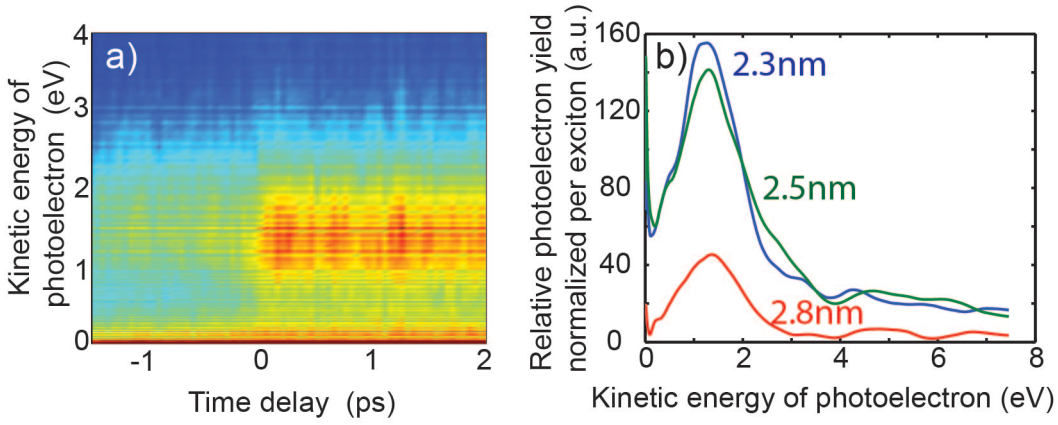

Figure 6.2: Two-photon photoelectron spectroscopy (PES) from excitonic states of CdSe QDs. (a) The temporal evolution of the PES spectra from 2.3 nm diameter CdSe QDs shows a broad peak corresponding to the 1S electron state. (b) Relative photoelectron yield per exciton for different diameter CdSe QDs, observed with a pump-probe time delay of 50 fs. The time independent background signal has been subtracted. The total photoelectron yield per exciton decreases as the QD diameter increases from 2.3 to 2.8 nm. Reproduced with permission from Xiong, Wei; Hickstein, Daniel D.; Schnitzenbaumer, Kyle J.; Ellis, Jennifer L.; Palm, Brett B.; Keister, K. Ellen; Ding, Chengyuan; Miaja-Avila, Luis; Dukovic, Gordana; Jimenez, Jose L.; Murnane, Margaret M.; Kapteyn, Henry C. *Nano Letters* **2013**, 13(6), 2924 – 2930. © 2013 American Chemical Society.

6.3.4 Photoelectron signal intensity dependence on QD size

The decreasing photoelectron intensity with increasing size of the QDs (Figure 6.2) is explained by the decrease evanescent electron density with increasing QD size. The Bohr radius for the CdSe 1S exciton is around 5.6 nm,[194] so intuitively, the exciton orbital extends further outside the dot as the size of the QD decreases. To gain a more quantitative understanding, we performed effective mass model calculations[54, 72-73] for the three sizes of quantum dots used for our experiment as outlined in Chapter 2. Two regions of potential are used to describe the QDs in this study, a spherical region whose parameters are set to those of bulk CdSe[121] surrounded by vacuum.[209] The input parameters used are listed in Table 6.1.

Table 6.1: Input parameters for the effective mass model calculations used to describe varying sizes of CdSe QDs.

	$m_{eff,e}$ (m_0)	$m_{eff,h}$ (m_0)	V_e (eV)	V_h (eV)	ε_r (ε_0)	E_g^{bulk} (eV)
CdSe	0.12	0.45	0	0	6.25	1.914
Vacuum	1	1	3.86	2.00	1	n/a

From these calculations, we obtained the electron wave functions and electron probability densities (Figure 6.3) of the 1S(e) electron. The electron probability distributions (Figure 6.3a) show two interesting features. First, the smaller quantum dots exhibit a maximum in the electron probability density that is closer to the surface of the QD. Second, the maximum electron density is larger for smaller dots, because the electron wave function has less room to spread inside of the smaller QDs. As a result of both of these factors, the electron density at the surface of the QD is lower for larger QDs.[54, 73, 119]

If we consider only the portion of the exciton electronic wave function that extends outside the QD (Figure 6.3c), we see that the electron density decays to ~10% of the interface density at distances of 0.1 nm. Much like quantum tunneling through a potential barrier, we see that the chance of finding the electron outside the QD is directly related to the electron probability density at the interface. The calculated probabilities of finding the electron outside the quantum dots are 7.4%, 6.7% and 5.6% for the 2.3 nm, 2.5 nm and 2.8 nm QDs, respectively.

Since the surface of a QD is coated with a layer of ligands, we also need to consider the effect that these ligands will have on a photoelectron emitted from the QD. We consider three ways that the ligands might affect photoemission. (1) The photoelectron could be scattered by the ligands, which can block its pathway to the vacuum. Surface photoemission of CdSe QDs using soft X-ray radiation from a synchrotron has shown that the photoelectrons originating from the core can effectively penetrate through the ligand layer.[210] Since photoelectrons emitted by soft X-ray photons have even shorter mean free paths than the lower kinetic energy photoelectrons studied here, this suggests that photoelectrons are not blocked by the ligands through a scattering mechanism. (2) The ligands could affect the excitation of electrons that reside in the portion of the wave function that extends outside of the QD and into the ligand layer. Because the mass of a free electron moving through the ligand layer is very nearly the mass of an electron in vacuum (e.g., octadecylamine

ligands do not form bands to which the effective mass approximation can be applied), we can therefore use continuum plane wave functions instead of Bloch wave functions to model the final states in the photoionization process. This increases the likelihood that the electrons outside of the QD will be ionized, as we shown in the next paragraph. (3) It is possible that the ligand layer could act as a tunneling barrier for the excited electrons.[31, 33] However, since the kinetic energy of the photoelectron is much higher than the height of the barrier, the tunneling barrier should not significantly affect the photoemission process. In short, it is unlikely that the aliphatic octadecylamine ligands will substantially alter the ionization process of the QD and can therefore be omitted in the following analysis.

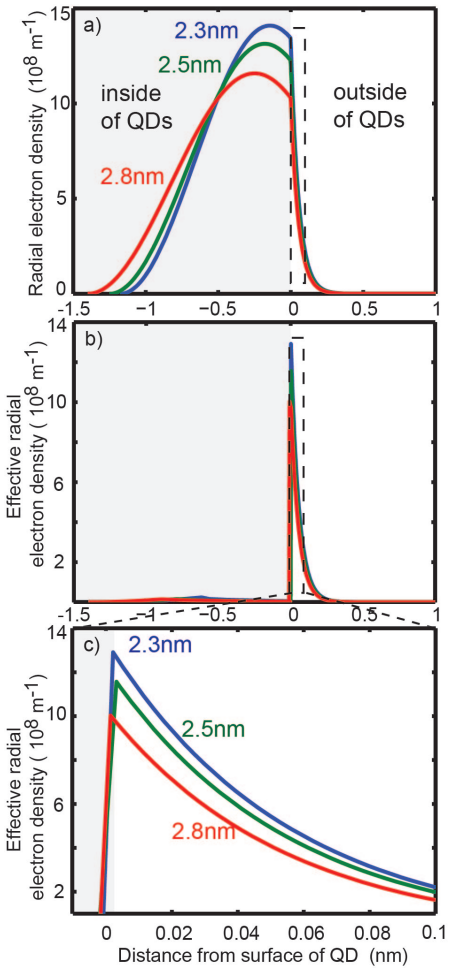

Figure 6.3: Radial electron probability densities for QDs with various diameters. On the x-axis, zero is the surface of the QD. (a) Radial electron probability density in both the interior and exterior of QDs. (b) The effective radial electron density available for photoemission after accounting for surface refraction and density of states shows that the portion of the electron wave function that extends outside of the QD dominates the photoelectron yield. (c) A magnified view of the effective radial electron probability density outside of the QDs. This size dependence of the electron density outside of the QD explains the experimentally observed QD size dependence of photoelectron yields. Reproduced with permission from Xiong, Wei; Hickstein, Daniel D.; Schnitzenbaumer, Kyle J.; Ellis, Jennifer L.; Palm, Brett B.; Keister, K. Ellen; Ding, Chengyuan; Miaja-Avila, Luis; Dukovic, Gordana; Jimenez, Jose L.; Murnane, Margaret M.; Kapteyn, Henry C. *Nano Letters* **2013**, 13(6), 2924 – 2930. © 2013 American Chemical Society.

Conceptually, the photoemission process can be divided into two parts: (i) electrons liberated from the interior of the QDs and (ii) electrons liberated from the exterior of the QDs. Following the three-step model of surface photoemission,[182] the interior electron is first excited into a Bloch state in the material (step 1), then experiences electron-electron and electron-phonon scattering while traveling to the surface (step 2), before finally passing through the interface between material and vacuum (step 3). Within this three-step model, the probability of photoemission from

the interior is limited for the following two reasons. First, in step 1, the transition from the initial exciton state to the final Bloch state of the material depends on the density of states of the final state.[205] Since hot exciton states are bulk-like,[178] we can estimate the density of states based on the bulk, i.e. the density of states is proportional to $m_e^{1.5}$, where m_e is the effective mass. The electron effective mass in CdSe is only 13% of the rest electron mass. Therefore, the density of states in CdSe is only 5% of the density of states of the same final states in vacuum. Second, in step 3, the electrons refract when exiting the QD, and the acceptance cone for low kinetic energy electrons is small. The transmission factor decreases as the initial position of the electron moves closer to the interface, and on average is below 0.3. The net result of these two effects is that the probability of photoemission from the interior of the material is significantly reduced, as shown in Figure 6.3b, which plots the effective electron density available for photoemission after the surface refraction and density of states are taken into account.

In contrast to the interior electrons, the evanescent electrons are intrinsically easier to liberate because they are located on the outside of the QDs and can be ejected into the vacuum directly. Therefore the photoelectron yield from the evanescent electron should follow Fermi's golden rule, which can be simplified to the integral $<\phi_{initial}|r|\phi_{final}>$. Since the final states are free electron wave functions for all three samples, the amount of evanescent electron density in the initial state determines the intensity of the photoelectron yield. Therefore, the increasing evanescent electron densities with smaller QD size (Figure 6.3) can qualitatively explain the trend of different photoelectron yields (Figure 6.2). More advanced theoretical calculations will likely be required to achieve precise quantitative agreement with the experimentally observed photoelectron yield.

Our observed connection between the evanescent electron densities and the photoelectron yield agrees well with previous surface photoemission studies using CdSe/ZnS core-shell quantum dots passivated with thiol ligands.[211] In their study, Naaman and coworkers found that smaller QD

cores have better coupling to the surface trap states through the shells, and explained this effect as a result of greater extension of the electron densities. In our study, we directly measure the extension of the exciton electronic wave function outside of the QD, and find that the wave function extends farther outside of the QDs in the case of smaller diameter QDs, in agreement with the results of the surface photoemission study[211] and previous transient absorption studies.[54, 117, 119, 162] Our approach also provides a straightforward and general way to measure the evanescent electron density in the QDs and other nanoparticles.

Interestingly, our finding that the photoelectron yield is inversely proportional to the QD size is a striking demonstration of how photoemission from nanoparticles can be dramatically different from bulk materials. At flat surfaces, the photoemission process must preserve momentum, and as a result, states far outside of the material (such as image potential states), do not have large transition probabilities.[212] However, our results show that the evanescent electron wave function outside of the QDs contributes significantly to the photoelectron signal. This phenomenon can be explained by the following two reasons. First, because the electron wave function is confined by the physical size of the quantum dots, which is around 2.5 nm, the uncertainty in the momentum k is 0.2 nm^{-1}, based on the Heisenberg uncertainty principle. The lattice constants of CdSe are a = 0.5 nm and c = 0.7 nm, and the corresponding unit vectors in k space are 2 nm^{-1} and 1.4 nm^{-1} respectively. Therefore, the momentum k uncertainty from the quantum confinement is 10% of the unit vector. This uncertainty in k mitigates the conservation of momentum constraints that are normally present in bulk photoemission from surfaces. In addition, the evanescent electron wave function is only 1 Å away from the interface due to quantum confinement, whereas image potential states are typically tens of angstroms away. Moreover, the evanescent electrons are part of the total electron wave function that permeates inside and outside the QD, enabling exchange of momentum

with the lattice. Thus, photoemission from small quantum dots resembles that from molecular systems rather than from bulk materials.

6.3.5 Conclusion

By combining a nanoparticle aerosol source with a velocity map imaging spectrometer, we studied two-photon photoelectron spectroscopy from quantum dots with a range of sizes. We found that the photoelectron yield per exciton decreases as the diameter of the quantum dot increases. Using effective mass modeling, we explained this trend as resulting from the different evanescent electron densities that extend outside the surface of the QDs. Thus, we showed that photoelectron spectroscopy of a nanoparticle aerosol provides a straightforward and robust method to compare exciton delocalization in different quantum confined materials. By better understanding the various factors influencing exciton delocalization and coupling, complex nanostructures can be designed for better efficiency.

In the future, photoelectron spectroscopy can provide additional information about the electronic structure of nanomaterials by incorporating electrospray aerosol sources that create physically isolated quantum dots and using higher photon-energy extreme-ultraviolet light sources such as high harmonic generation or synchrotron radiation. When combined with angular information obtained from velocity map imaging techniques, exciton orbitals can be imaged to provide direct fundamental insights into the quantum-confined dynamics of quantum dots and other nanoscale systems.

6.4 Solvent Effects on Femtosecond Charge Transfer

6.4.1 Abstract

To predict and understand the performance of nano-devices in different environments, the influence of the solvent must be explicitly understood. In this section, this important but largely unexplored question is addressed through a comparison of quantum dot charge transfer processes occurring in both liquid phase and in vacuum. By comparing solution phase transient absorption spectroscopy and gas-phase photoelectron spectroscopy, we show that hexane, a common nonpolar solvent for quantum dots, has negligible influence on charge transfer dynamics. Our experimental and theoretical results indicate that the reorganization energy of nonpolar solvents plays a minimal role in the energy landscape of charge transfer in quantum dot devices. Thus, this study confirms that measurements conducted in nonpolar solvents can indeed provide insight into nano-device performance in a wide variety of environments.

6.4.2 Introduction

To design efficient devices using nanoscale components (nano-devices), the charge transfer pathways between nanostructures must be understood in a predictive way. Numerous studies have used time-resolved spectroscopic techniques to determine the rate limiting steps in charge transfer between individual components in nanocrystal based optoelectronic devices.[6, 56, 116, 181-182, 213-215] These studies are typically conducted using liquid phase samples and the effect of the local solvent environment on the charge transfer process has proven difficult to investigate.[214, 216] Understanding the influence of the solvent is important since nano-devices are often synthesized and tested in one environment, but ultimately deployed in a different environment. For example, colloidal semiconductor quantum dots (QDs) are typically prepared and characterized in organic solvents, but often attached to surfaces as films in photovoltaics.[5] Solvent molecules can alter the charge transfer

process by perturbing the dielectric layer, or through the dynamic configuration rearrangements (electronic and conformational) of the solvent molecules at the nanomaterial surface during the charge transfer process.[214] Therefore, rational design and characterization of nanomaterials requires a firm understanding of solvent effects.

Prior investigations utilized solution-phase transient absorption spectroscopy (TA) to show that polar solvents can significantly alter the charge transfer rate.[217] However, to dissolve nanoparticles into solvents with different polarities, it is typically necessary to alter the ligand coverage or swap ligands entirely, convolving solvent effects with ligand effects. This makes it difficult to isolate the effect of the solvent alone.

6.4.3 Experimental approach

We overcome this technical challenge by utilizing a velocity map imaging spectrometer[184-185] coupled to a nanoparticle aerosol source (nano-VMI).[120, 218-219] Using this instrument, described in Section 6.2 and Figure 6.1, allows us to perform a time-resolved photoelectron spectroscopy experiment (PES, Figure 6.4a) on isolated nanoparticles in vacuum. To eliminate complications that would naturally arise from the use of different ligands, we implement gas phase nano-VMI spectroscopy on quantum dots with identical ligand coverage as in solution phase. Here we unambiguously characterize the influence of hexane, a commonly used nonpolar solvent, on charge transfer by comparing nano-VMI data with solution phase TA measurements conducted on the same quantum dot sample. Solution-phase TA was performed using the experimental setup described in Chapter 2. Specifically, we compare gas-phase PES and solution-phase TA measurements of the charge transfer rate between CdSe QDs and methyl viologen (MV) cations (Figure 6.4) to characterize the influence of the solvent (hexane) on this process. Hexane is frequently used as a solvent in the characterization of QDs and it is this important to determine whether it influences charge transfer between the QD and an electron acceptor. We selected the

CdSe-methyl viologen system for these studies because it is a well characterized system that exhibits fast and efficient charge transfer.[30, 116, 215, 220-221]

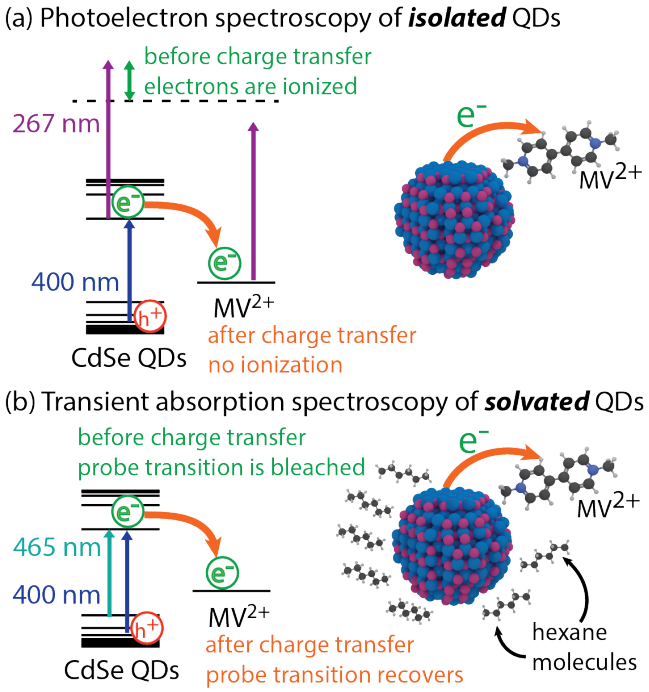

Figure 6.4: Schematic comparison of PES and TA measurements. (a) Photoelectron spectroscopy (PES) detects electrons in order to follow charge transfer dynamics in solvent-free quantum dots (QDs). A 400 nm pump pulse photoexcites electrons, and before (or without) charge transfer they can be ionized by a delayed 267 nm probe pulse. Once transferred to MV, the probe photon energy is insufficient to ionize the electron. (b) The transient absorption (TA) measurement follows the same dynamics by observing a time-dependent absorption change in solvated QDs. Here, before (or without) charge transfer the 1S(e)-1S3/2(h) transition is bleached due to the presence of the photoexcited electron, resulting in a decrease in absorption. By comparing PES and TA, we can isolate the effect of the solvent, hexane, on charge transfer. Ligands are present on the surface of the QDs, though not depicted here. Reproduced with permission from Ellis, Jennifer L.; Hickstein, Daniel D.; Schnitzenbaumer, Kyle J.; Wilker, Molly, B.; Palm, Brett B.; Jimenez, Jose L.; Dukovic, Gordana; Murnane, Margaret M.; Kapteyn, Henry C. *J. Am. Chem. Soc.* **2015**, 137, 3759 – 3762. © 2015 American Chemical Society.

To prepare the charge-transfer system, we adsorbed methyl viologen dye (MV, Sigma-Aldrich) to octadecylamine-capped CdSe QDs with a diameter of 2.3 nm (NN-Labs) in the solution phase. We added methanol (dropwise) to 12 mg of MV powder until the powder was completely dissolved, and then added this solution to a 0.01 mg/mL solution of QDs in hexane. This concentration corresponds to ~100 MV molecules per QD in solution. The control sample consisted of CdSe QDs also diluted to 0.01 mg/mL in hexane, but otherwise used as received. We then used ultraviolet-visible absorption and steady state fluorescence spectroscopies to characterize

the static spectral features of CdSe QDs and CdSe-MV complexes. The absorption spectra of both samples show a peak at 480 nm (Figure 6.5a) that corresponds to the 1S(e)-$1S_{3/2}$(h) transition. The CdSe-MV spectrum shows slightly broadened peaks, which is likely due to the excitonic coupling of the 1S(e) exciton state to the LUMO level of MV.[222] The fact that all of the peaks are preserved demonstrates that adding MV to the CdSe does not significantly influence either quantum confinement or solubility of the QDs. The quenching of the CdSe fluorescence peak upon the addition of MV (Figure 6.5b) indicates that the MV molecules successfully adsorb to the QD surfaces and that excited electrons in the CdSe QDs migrate to the MV faster than the rate of radiative decay.[116, 220-221]

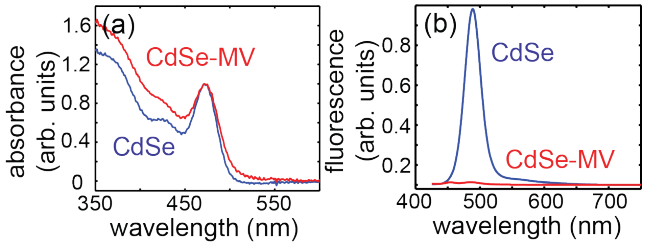

Figure 6.5: Absorption and fluorescence spectra of the CdSe-MV system. (a) The similarity of the UV-Vis absorption spectra of CdSe and the CdSe-MV in solution reveals that the addition of MV does not alter the quantum confinement of the CdSe QDs. (b) The quenching in the fluorescence spectra upon adsorption of MV indicates that photoexcited electrons in the CdSe QDs undergo electron transfer to MV before radiative recombination can take place. Reproduced with permission from Ellis, Jennifer L.; Hickstein, Daniel D.; Schnitzenbaumer, Kyle J.; Wilker, Molly, B.; Palm, Brett B.; Jimenez, Jose L.; Dukovic, Gordana; Murnane, Margaret M.; Kapteyn, Henry C. *J. Am. Chem. Soc.* **2015**, 137, 3759 – 3762. © 2015 American Chemical Society.

6.4.4 Comparison of TA and PES measurements

Before addressing the effect of solvent molecules on charge transfer processes, we first verified that PES can indeed be used to track excited state dynamics. This was accomplished through comparison with solution-phase TA measurements of electron dynamics occurring within CdSe QDs. In the PES experiment the 400 nm pump pulse excites electrons primarily to the 1S(e) level (leaving a deeper hole in the valence band, based on the assignment of features in UV-Vis absorption spectra[13, 66, 194, 201]), while a time-delayed 267 nm probe pulse ionizes the excited electron (Figure 6.4a). Therefore, immediately after the creation of 1S electrons, the photoelectron signal is

enhanced. The decay of the photoelectron signal reflects the decay of the 1S population due to both radiative and nonradiative relaxation. In the TA experiment, we monitor the dynamics of the bleach of the 1S(e)-$1S_{3/2}$(h) transition (Figure 6.4b) following excitation with a 400 nm pump pulse. The bleach of the 1S(e)-$1S_{3/2}$(h) transition also probes the population of electrons in the 1S state.[13] Therefore, both the TA and the PES measurements probe the 1S electron population. Because of the higher sensitivity of the PES measurement described in Section 6.2, different concentrations of the same solution were required for each experiment. After the PES experiment, a portion of the remaining sample solution was concentrated (up to 10x) immediately before use in the TA measurement. Samples were concentrated by evaporating the hexane solvent under vacuum and redispersing in hexane to reach the desired concentration. TA measurements of samples with different concentrations display similar kinetics. In both experiments, the fluence of the 400 nm pump pulse is selected so that an electron is excited in less than 10% of QDs in the interaction region, in order to minimize the effects from multiple excitons in a single quantum dot.

In the absence of charge transfer (i.e. no adsorbed MV), the difference between the two measurements is the presence (TA) or absence (PES) of surrounding solvent molecules. We expect identical results from TA and PES, because the solvent should not strongly affect the dynamics that take place inside of the QD. Indeed, we do observe good agreement between the TA and PES measurements (Figure 6.6a, Table 6.2) demonstrating that PES has the ability to follow exciton dynamics. Both measurements of CdSe QDs (Figure 6.6a) show a strong enhancement in signal at zero time delay, followed by a small initial decay and a long plateau. To quantify these dynamics from both instruments, they were fit with a double exponential decay convoluted with the instrument response function (IRF, Table 6.2).

$$S(t) = IRF \otimes \left(a_1 e^{-(t-t_0)/\tau_1} + a_2 e^{-(t-t_0)/\tau_2} \right) \qquad \text{Eqn. 6.2}$$

The slow component (τ_1, 120 ps) is beyond the temporal range of the delay stage used, which is consistent with the few nanosecond radiative lifetime of the 1S electron.[165] The small fast component (τ_2, 100s of fs) results from the small fraction of electrons that undergo faster decay. We note that the difference between the two measurements at negative time delays results from the fact that the 267 nm pulse used in the PES experiment excites hot electrons, which can then be ionized by the 400 nm pulse. Thus, the TA experiment and the PES experiment probe different processes in the pre-t_0 regime. In this paper, we focus only on the band edge electron dynamics (positive time delays), where TA and PES can be directly compared.

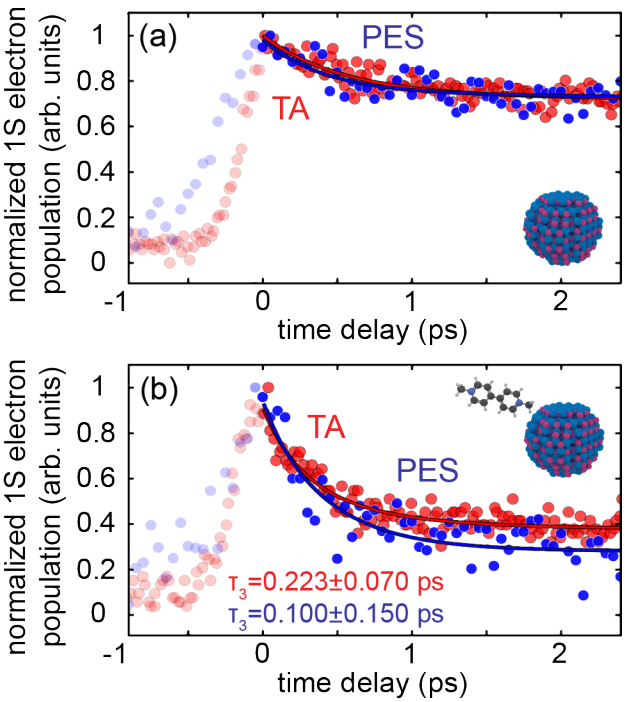

Figure 6.6: Comparison of gas phase PES and solution phase TA dynamics of CdSe QDs with and without absorbed MV. (a) In the absence of MV molecules, the 1S electron population only decays slightly on a few picosecond timescale. (b) When MV is attached to the QDs, a ~100 fs decay is seen, indicating charge transfer from the QD to the MV. There is no significant difference between the decay rates obtained from the TA and PES experiments, indicating that the hexane solvent molecules have a minimal effect on the charge transfer process. Reproduced with permission from Ellis, Jennifer L.; Hickstein, Daniel D.; Schnitzenbaumer, Kyle J.; Wilker, Molly, B.; Palm, Brett B.; Jimenez, Jose L.; Dukovic, Gordana; Murnane, Margaret M.; Kapteyn, Henry C. *J. Am. Chem. Soc.* **2015**, 137, 3759 – 3762. © 2015 American Chemical Society.

Having verified that PES can track charge dynamics in CdSe QDs, we can now apply it to study charge transfer in the CdSe-MV complex. In this case we see a faster decay of the PES signal

(Figure 6.6b), and therefore the 1S electron population, due to electron transfer to the MV LUMO (from which the electron cannot be ionized by the 267 nm probe, Figure 6.4a). The TA measurements conducted on the same sample also shows a faster decay in the 1S electron population when MV is adsorbed, seen as the faster recovery of the bleach of the 1S(e)-1$S_{3/2}$(h) transition. We fit the CdSe-MV kinetics from each instrument using a triple exponential decay convolved with the IRF.

$$S(t) = IRF \otimes \left(a_1 e^{-(t-t_0)/\tau_1} + a_2 e^{-(t-t_0)/\tau_2} + a_{et} e^{-(t-t_0)/\tau_{et}} \right) \quad \text{Eqn. 6.3}$$

Two of the time constants (τ_1 and τ_2) are fixed from the fits of the CdSe kinetics. The third time constant (τ_{et}) is taken to be indicative of the additional deactivation channel (electron transfer) of the 1S(e) state introduced by the adsorption of MV. The time constants for electron transfer from CdSe to MV extracted here of 220 ± 70 fs (TA) and 100 ± 150 fs (PES) (Figure 6.6b, Table 6.2), which are in agreement with previous studies.[116, 220] The charge transfer rates obtained in both measurements are the same within the fitting error (one standard deviation). This indicates that the presence of hexane has a negligible effect on the charge transfer process. We note that these recovered τ_{et} values are very close to the timescale of the instrument response functions of the TA and PES experiments, leading to the large errors seen in the fit values (Table 6.2).

Table 6.2: Fitting parameters of TA and PES kinetics for CdSe and CdSe-MV.

	CdSe		CdSe-MV	
	TA	PES	TA	PES
IRF (ps)	0.25	0.12	0.25	0.12
a_1 (%)	64 ± 1	64 ± 1	25 ± 5	9 ± 1
τ_1 (ps)	120	120	120	120
a_2 (%)	36 ± 2	36 ± 5	30 ± 11	47 ± 14
τ_2 (fs)	525 ± 50	415 ± 100	525	415
a_{et} (%)	n/a	n/a	45 ± 9	44 ± 4
τ_{et} (fs)	n/a	n/a	223 ± 70	100 ± 150

6.4.5 Solvent electronic polarization model

The negligible influence of the hexane solvent molecules can be understood through the solvent electronic polarization model developed by Kim and Hynes.[223-227] In this model, solvent molecules contribute to the charge transfer reorganization energy through both the electronic polarization and the orientational polarization. Since hexane is nonpolar, reorientation of the molecules does not alter the electron distribution. Therefore, the orientational contribution vanishes. Alternatively, the solvent molecules can influence the charge transfer by the redistribution of their electron populations. The electronic contribution will only be significant when the charge transfer reaction is fast compared to the solvent electronic polarization rate.

This can be characterized by the ratio between the rates of charge transfer and solvent electronic polarization, $\rho=2\beta/(\hbar\omega)$, where, β is the electronic coupling factor and ω is the electronic transition frequency of the solvent[226] We estimated β using the broadening[222] of the absorption spectra of the QDs upon the MV adsorption (Figure 6.5a), which is approximately 0.05 eV. Since hexane does not absorb in the visible region, its electronic transition energy, $\hbar\omega$, is >3 eV.[226-227] Therefore $\rho<0.02$, which means that the solvent electronic polarization is rapid compared to the charge transfer process (non-adiabatic). As a result, neither the electronic nor the orientational polarization of hexane contribute significantly to the reorganization energy, and consequently, one would not expect solvent reorganization to have a large influence on the charge migration dynamics of the CdSe-MV complex. Furthermore, from this analysis we predict that the influence on QD charge transfer of *any* nonpolar transparent solvent should be minimal, as long as the charge transfer process is slower than a few femtoseconds, which is true for most charge-transfer processes. This is not necessarily the case for polar solvents, where the orientational reorganization energy can affect the charge transfer process. Dynamic solvent effects of polar solvents must be considered.[228-229]

6.4.6 Conclusions

In conclusion, we investigated the influence of the solvent on charge transfer between quantum dots and methyl viologen by comparing dynamics measured using solvent-free two-photon photoelectron spectroscopy with those measured by solution-phase transient absorption spectroscopy. We first verified that photoelectron spectroscopy is a viable method of measuring excited electron dynamics in quantum dots. After this verification we applied this technique to study a charge transfer reaction. The good agreement in the charge transfer dynamics obtained by solvent-free and solution phase spectroscopies indicates that common nonpolar organic solvents, such as hexane, have a negligible influence on the charge transfer process between quantum dots and electron acceptor molecules. This observation supports the assumption that kinetic data measured by transient absorption spectroscopy, under nonpolar solvent environments, can be used to accurately infer nano-device behavior in air or vacuum. In the future, this approach can also be used to investigate polar solvents, to gain a full picture of the solvent effects on charge transfer on the nanoscale. This knowledge will provide another tunable parameter to manipulate the charge transfer characteristics of nanocrystal-based optoelectronic devices.

Chapter 7. Summary and Outlook

> "They are ill discoverers that think there is no land when they can see nothing but sea."
>
> - Francis Bacon

7.1 Overview

This dissertation focused on how chalcogenide ligands affect the photoexcited state dynamics of cadmium chalcogenide QDs. Through the application of a theoretical framework to describe these systems, the experimental determinations of photophysical impacts, and the application of these methods to other research questions, this dissertation furthers our fundamental understanding of these systems.

Chapter 3 described the impact of chalcogenide ligand exchange on the band gap energy of CdTe QDs, which was decreased by up to 10%. By applying an effective mass approximation (EMA) model to chalcogenide ligand capped CdTe QDs, we found that they can be treated as core/shell heterostructures. The model, while simple, required no adjustable parameters to adequately describe the observed ligand dependent band gap energy ordering. Using this model, we calculated the ligand effects on excited state electron and hole distributions. The same model was applied to CdSe QDs in the gas phase in Chapter 6 to explain the observed dependence of photoelectron signal on QD size. Smaller QDs, exhibiting stronger quantum confinement as demonstrated by the EMA model, have a larger portion of the electron wave function leak into the

surrounding environment than do larger, less confined QDs. As this portion of the wave function is directly measureable by gas-phase photoelectron spectroscopy, smaller QDs yielded stronger signal.

Measurements of chalcogenide ligand capped QD photophysics demonstrated decreased excited state lifetimes compared to those capped with aliphatic ligands, both for CdSe QDs capped with S^{2-}, Se^{2-}, and Te^{2-} in Chapter 4 and CdTe QDs capped with Se^{2-} in Chapter 5. This is attributed to significantly increased excited state deactivation, through both electron and hole trapping. In CdSe-Te (Chapter 4) and CdTe-Se (Chapter 5), these trapping events were shown to even be competitive with carrier cooling to the band edges. For other systems investigated, however, ligand identity had no effect on the characteristic time scale of carrier cooling.

Considering the interplay between photophysical and photochemical processes outlined in Chapter 1, knowledge of these time constants for excited state deactivation are integral for device design. For example, Chapter 4 describes 20 time constants that have not been previously measured. In conjunction with reported electron transfer rates in devices, we can elucidate the benefits and drawbacks of the chalcogenide ligand family. Considering the time constant for electron transfer reported for CdSe-S/TiO_2 QDSSC (7.6 ns)[100] and our measured CdSe-S 1S(e) band edge lifetime in Chapter 4 (1.8 ns), Eqn. 1.1 predicts a QE_{et} of 20%. While this QE_{et} is lower than the ideal for an operational device, it is high enough for a device to successfully convert photons to current, which suggests that much can be learned from these comparisons.

The application of the EMA model described in Chapter 2 and Chapter 3 to chalcogenide capped CdSe QDs demonstrated that Se^{2-} and Te^{2-} ligands aren't expected to increase electron transfer rates over S^{2-}. With the relatively slow electron transfer reported for CdSe-S/TiO_2 and our measured 1S(e) lifetimes of CdSe-Se (70 ps) and CdSe-Te (10 ps), Eqn. 1.1 predicts QE_{et} of 1% and 0.1%, respectively. These low QE_{et} values suggest that Se^{2-} and Te^{2-} ligands should generally be

avoided for QDSSC or other applications with relatively slow electron transfer from the band edge 1S(e) state.

Other devices, however, provide a different story. As mentioned in Chapter 4, field effect transistors utilizing CdSe-S arrays have electron hopping time constants on the subpicosecond timescale.[50, 95] In conjunction with an electron transfer time constant of 500 fs, the 1S(e) lifetimes of CdSe-Se (70 ps) and CdSe-Te (10 ps) yield QE_{et} values of 99% and 95%, respectively, according to Eqn. 1.1. These suggest that any of the chalcogenide ligands should be expected to perform well in QD arrays with such fast hopping rates. Depending on the charge transfer mechanism of interest, the increased trapping in CdSe-Se and CdSe-Te may even be desirable.

The values reported in Chapter 4 demonstrate the drastic impact that surface modification can have on cadmium chalcogenide QDs. The impact of very thin CdSe shell growth and Se^{2-} ligand exchange were also investigated and compared in Chapter 5. Compared to CdTe QDs, both of these modifications decreased photoexcited electron lifetimes. Chapter 5 also described the first observation of exciton-phonon coupling in chalcogenide capped nanocrystals. A noteworthy difference between the two surface modifications is that the Se^{2-} ligand exchange effectively decreased coupling between the X1, X2, and X3 excitons and the longitudinal acoustic phonon to zero.

The theoretical and experimental methods employed in investigating these effects of ligand exchange on QD photophysics also provided significant insight into the interpretation of gas-phase photoionization spectroscopy experiments. The comparison of solution-phase transient absorption and gas-phase photoelectron measurements in Chapter 6 confirmed the ability of time-resolved photoelectron spectroscopy to monitor photoexcited electron dynamics. The electron transfer process was investigated in the presence (TA) and absence (PES) of hexane solvent by coupling the electron acceptor methyl viologen to CdSe-ODA QDs. Similarly fast electron transfer was measured

in both the solvated and solvent-free environments. Although this result is not terribly surprising given the nonpolar nature of hexane, it represents one of the only experimental verifications of the widely applied assumption that charge transfer dynamics from CdSe QDs are not strongly influenced by changes in the solvent environment.

7.2 Future Directions

As is often the case in scientific research, addressing one question raises a multitude of others. While the results presented throughout this dissertation represent a deeper understanding of the role chalcogenide ligands play in determining QD photophysics, many questions remain. The following subsections address future research directions based upon the work described in this dissertation.

7.2.1 Exploring limitations

One obvious focus of future research is developing a firmer understanding of the limitations of the work described here. There is much to be learned by determining exactly what conditions push a theoretical model or experimental technique to its limits. For example, the treatment of chalcogenide ligand capped CdTe QDs as core/shell heterostructures in Chapter 3 focused on band gap energies. This is due to the limitations of the model. Utilizing a multi-band model (rather than the single-band model used here) would be necessary to investigate higher energy transitions. The QDs used for the study presented in Chapter 3 were small and strongly confined, leading to significant perturbations following ligand exchange. Surely, there is a limit to the analogy between chalcogenide ligand capped QDs and core/shell heterostructures. Finding this limit, whether it be due to QD size or particular ligand characteristics, would provide information about when a coarse-grain model, as used here, is an appropriate theoretical construct and when a more detailed approach

is necessary. This type of deeper understanding would further inform device design using particular QD-ligand systems.

Another limitation that would be beneficial to explore in further depth is the application of the state-specific transient absorption experimental approach to nanocrystalline heterostructures. Since the state specific approach is often employed to deduce the electronic structure of nanocrystalline heterostructures, it is critical to evaluate whether this is a reliable method for experimentally evaluating electronic structure. As highlighted by the discussion of transient absorption measurements on two different sizes of CdTe QD in Chapter 5, the interpretation of TA kinetics can be ambiguous even with a firm understanding of the sample's electronic structure. Further application of the state specific approach to better understood systems can elucidate its usefulness when employed with less understood systems. Ultrafast transient absorption with a broadband probe is an excellent tool for exploring these limitations.

7.2.2 Continuation of CdTe work

Further work could be undertaken to build upon the work presented in Chapter 5. To date, photophysical measurements evaluating the analogy between chalcogenide ligand capped and core/shell QDs exist for only one size of CdTe QD. Since size is a readily controllable parameter, it would be informative to investigate how the photophysics of these samples compares for different QD core sizes. In a previous report,[63] the percentage of the bleach recovery associated with the subpicosecond to single picosecond timescales was correlated with CdTe QD age. The question of exactly how and by what mechanism QD aging may affect excited state dynamics is largely unknown and worth further consideration. The potential for aging concerns in CdTe QDs therefore warrants a quantitative study of how exactly the age of a sample, along with other variables, impacts excited state lifetime. These effects are readily measureable using our TA setup, require fairly simple analysis, and represent an excellent step in further understanding the photophysics of CdTe QDs. Recent

unpublished results in the Dukovic group suggest that post-synthetic purification, rather than QD age, is the variable closely tied to B1 lifetimes in CdTe QDs. Due to the incorporation of CdTe into many nanoheterostructures, knowledge of how to mitigate the decrease in excited state lifetime associated with post-synthetic purification and/or aging is expected to be of interest to the research community. A quantitative description of how these variable affect excited state lifetimes in CdTe QDs also informs our material choice for future studies of ligand dependent behavior. If aging or purification concerns in CdTe are deemed to be significant, CdSe QDs may prove to be a more attractive system for future studies that seek to isolate ligand induced effects.

7.2.3 Investigation of metal chalcogenide complex ligands

The same questions explored in this dissertation for chalcogenide ligands can be asked of metal chalcogenide complex (MCC) ligands. These are among the ligands discussed in Chapter 1 that combine the small size and high conductivity desired for photovoltaic and photochemical applications.[36-37] Preliminary TA kinetics of the MCC ligand $Sn_2S_6^{4-}$ capped CdSe QDs suggest that as least some MCC ligands do not shorten excited state lifetimes to the same extent as observed for Se^{2-} and Te^{2-} ligands. The use of MCC capped QDs therefore has the potential to utilize the benefits of small, conductive ligand shells without the drawback of increased carrier trapping as described for Se^{2-} and Te^{2-} ligands in Chapter 4.

7.2.4 Photochemical measurements and lengthening excited state lifetimes

The interplay of photochemistry and photophysics ultimately dictates the efficiency of a charge transfer process. For this reason, measurements of charge transfer involving chalcogenide ligand capped QDs would nicely complement the measurements discussed in this dissertation. This is often done by coupling dye molecules with QDs and monitoring the dynamics of relatively simple

single electron redox reactions, as done in Chapter 4 to assign the various features of CdSe-ODA TA spectra and in Chapter 6 to probe solvent effects on charge transfer.

To investigate complementary photochemistry of systems involving chalcogenide ligands, however, the choice of proper experimental systems will be critical. It is imperative to avoid any undesired side reactions, which would be a challenge considering that chalcogenide ions readily participate in solution phase redox chemistry. Another complicating factor would be the propensity for adsorbed dye molecules to exhibit different reaction chemistry than those in solution due to dye sensitization or degradation.[230] For any definitive conclusions to be drawn from these single electron transfer experiments, the influence of both undesired redox reactions and surface effects would have to be mitigated.

7.2.5 Exciton-phonon coupling

This dissertation barely scratches the surface of the exciton-phonon coupling that can be measured with our experimental setup. Given that many details of exciton-phonon coupling in QDs remain unknown, further experiments would be of great value to the research community. The finding presented in Chapter 6 that ligand exchange to Se^{2-} critically damps or shuts off the coupling between all excitons and the longitudinal acoustic phonon is an intriguing result. At this time, the cause for the lack of an acoustic phonon mode is unclear. Exploration of different ligands and how they affect the phonon modes of the QD crystal lattice could prove illuminating. Exploring the exciton-phonon coupling in nanocrystalline heterostructures may prove useful both for determining the mechanism behind coupling and learning about the electronic structure of these systems from the observed coupling.

7.2.6 Effects of polar solvent on charge transfer

The ability to make a direct comparison between solution phase transient absorption and gas phase photoelectron spectroscopies is unique. The complementary nature of these techniques and their ability to collectively explore challenging research questions warrant further studies. The investigation of charge transfer dynamics in the presence of a polar solvent represents an excellent next step. Solvent impacts on charge transfer can be quantified through the study of electron transfer dynamics in the presence and absence of a series of solvents with differing polarities, providing an experimental determination of reorganization energy in QD-acceptor systems.

7.3 Conclusion

This dissertation describes the photophysical behavior of chalcogenide ligand capped QDs. Through the application of theoretical and experimental methods, this dissertation deepens our understanding of the promising family of chalcogenide ligands. Among the results described here are:

- The successful application of an effective mass approximation model to chalcogenide ligand capped QDs, describing them as core/shell structures.
- The measurement of excited state decay rates in chalcogenide ligand capped CdSe QDs, including both electron and hole cooling. Along with values for CdTe-Se, these are among the 23 photoexcited state relaxation time constants measured in this dissertation that have not been previously reported.
- The first observation of exciton-phonon coupling in QD systems using the commercially available Helios transient absorption spectrometer, and the first observation of exciton-phonon coupling in a chalcogenide ligand capped QD system.

- The comparison of measured electron transfer rates in the presence and absence of solvent, demonstrating a technique for directly determining the impact of any solvent on charge transfer processes.

These findings are striking demonstrations of how the physical properties of a QD, and specifically the ligand layer that surrounds it, drastically impact its energetics and excited state behavior. Taken collectively, these results provide substantial insight for more informed design of solar energy harvesting systems.

"I must always search for the remarkable combinations, add unknowns, mix things that were clearly marked with things beyond marking. I would leave the simulated test and enter the forbidden territory. I would look for that moment when I would begin to pour alone in wonder. I would always try to seize that moment and accept its challenge. I wanted to become the seeker, the aroused and passionate explorer, and it was better to go at it knowing nothing at all, always choosing the unmarked bottle, always choosing your own unproven method, armed with nothing but faith and a belief in astonishment."

- Pat Conroy, Lords of Discipline

References

1. Climate Change 2013: The Physical Science Basis. Intergovernmental Panel on Climate Change: 2013.
2. Basic Research Needs for Solar Energy Utilization. US Department of Energy: 2005.
3. Nozik, A. J.; Beard, M. C.; Luther, J. M.; Law, M.; Ellingson, R. J.; Johnson, J. C., Semiconductor Quantum Dots and Quantum Dot Arrays and Applications of Multiple Exciton Generation to Third-Generation Photovoltaic Solar Cells. *Chem. Rev.* **2010,** *110*, 6873-6890.
4. Talapin, D. V.; Lee, J.-S.; Kovalenko, M. V.; Shevchenko, E. V., Prospects of Colloidal Nanocrystals for Electronic and Optoelectronic Applications. *Chem. Rev.* **2010,** *110*, 389-458.
5. Kamat, P. V.; Tvrdy, K.; Baker, D. R.; Radich, J. G., Beyond Photovoltaics : Semiconductor Nanoarchitectures for Liquid-Junction Solar Cells. *Chem. Rev.* **2010,** *110*, 6664-6688.
6. Wilker, M. B.; Schnitzenbaumer, K. J.; Dukovic, G., Recent Progress in Photocatalysis Mediated by Colloidal II-VI Nanocrystals. *Isr. J. Chem.* **2012,** *52*, 1002-1015.
7. Osterloh, F. E., Inorganic Materials as Catalysts for Photochemical Splitting of Water. *Chem. Mater.* **2008,** *20*, 35-54.
8. Osterloh, F. E., Inorganic nanostructures for photoelectrochemical and photocatalytic water splitting. *Chem. Soc. Rev* **2013,** *42*, 2294-2320.
9. Scholes, G. D.; Rumbles, G., Excitons in nanoscale systems. *Nat. Mater.* **2006,** *5*, 683-696.
10. Brus, L. E., Electron–electron and electron-hole interactions in small semiconductor crystallites: The size dependence of the lowest excited electronic state. *J. Chem. Phys.* **1984,** *80*, 4403-4409.
11. Brus, L., Electronic Wave Functions in Semiconductor Slusters: Experiment and Theory. *J. Phys. Chem.* **1986,** *90*, 2555-2560.
12. Smith, A. M.; Nie, S., Semiconductor Nanocrystals: Structure, Properties, and Band gap Engineering. *Acc. Chem. Res.* **2010,** *43*, 190-200.
13. Klimov, V. I., Spectral and Dynamical Properties of Multiexcitons in Semiconductor Nanocrystals. *Annu. Rev. Phys. Chem.* **2007,** *58*, 635-673.
14. Kamat, P. V., Meeting the Clean Energy Demand: Nanostructure Architectures for Solar Energy Conversion. *J. Phys. Chem. C* **2007,** *111*, 2834-2860.
15. Kamat, P. V., Quantum Dot Solar Cells. Semiconductor Nanocrystals as Light Harvesters. *J. Phys. Chem. C* **2008,** *112*, 18737-18753.
16. Kim, M. R.; Ma, D., Quantum-Dot-Based Solar Cells: Recent Advances, Strategies, and Challenges. *J. Phys. Chem. Lett.* **2015,** *6*, 85-99.
17. Choi, C. L.; Alivisatos, A. P., From Artificial Atoms to Nanocrystal Molecules: Preparation and Properties of More Complex Nanostructures. *Annu. Rev. Phys. Chem.* **2010,** *61*, 369-389.
18. Zhu, H.; Lian, T., Wavefunction engineering in quantum confined semiconductor nanoheterostructures for efficient charge separation and solar energy conversion. *Energy Environ. Sci.* **2012,** *5*, 9406-9406.
19. de Mello Donegá, C., Synthesis and properties of colloidal heteronanocrystals. *Chem. Soc. Rev.* **2011,** *40*, 1512-1546.
20. Garnweitner, G.; Niederberger, M., Organic chemistry in inorganic nanomaterials synthesis. *J. Mater. Chem.* **2008,** *18*, 1171-1182.
21. Yin, Y.; Alivisatos, A. P., Colloidal Nanocrystal Synthesis and the Organic-Inorganic Interface. *Nature* **2005,** *437*, 664-670.

22. Peng, X.; Wickham, J.; Alivisatos, A. P., Kinetics of II-VI and III-V Colloidal Semiconductor Nanocrystal Growth: "Focusing" of Size Distributions. *J. Am. Chem. Soc.* **1998,** *7863*, 5343-5344.
23. Yu, W. W.; Wang, Y. A.; Peng, X. G., Formation and Stability of Size-, Shape-, and Structure-Controlled CdTe Nanocrystals: Ligand Effects on Monomers and Nanocrystals. *Chem. Mater.* **2003,** *15*, 4300-4308.
24. Knowles, K. E.; Frederick, M. T.; Tice, D. B.; Morris-Cohen, A. J.; Weiss, E. A., Colloidal Quantum Dots: Think Outside the (Particle-in-a-)Box. *J. Phys. Chem. Lett.* **2012,** *3*, 18-26.
25. Hines, D. A.; Kamat, P. V., Recent Advances in Quantum Dot Surface Chemistry. *ACS Appl. Mater. & Interfaces* **2014,** *6*, 3041-3057.
26. Kamat, P. V., Manipulation of Charge Transfer Across Semiconductor Interface. *J. Phys. Chem. Lett.* **2012,** *3*, 663 - 672.
27. Kamat, P. V., Boosting the Efficiency of Quantum Dot Sensitized Solar Cells through Modulation of Interfacial Charge Transfer. *Acc. Chem. Res.* **2012,** *45*, 1906-1915.
28. Dibbell, R. S.; Watson, D. F., Distance-Dependent Electron Transfer in Tethered Assemblies of CdS Quantum Dots and TiO 2 Nanoparticles. *J. Phys. Chem. C* **2009,** *113*, 3139-3149.
29. Dibbell, R. S.; Youker, D. G.; Watson, D. F., Excited-State Electron Transfer from CdS Quantum Dots to TiO 2 Nanoparticles via Molecular Linkers with Phenylene Bridges. *J. Phys. Chem. C* **2009,** *113*, 18643-18651.
30. Tagliazucchi, M.; Tice, D. B.; Sweeney, C. M.; Morris-cohen, A. J.; Weiss, E. A., Ligand-Controlled Rates of Photoinduced Electron Transfer in Hybrid CdSe. *ACS Nano* **2011,** *5*, 9907-9917.
31. Pernik, D. R.; Tvrdy, K.; Radich, J. G.; Kamat, P. V., Tracking the Adsorption and Electron Injection Rates of CdSe Quantum Dots on TiO2: Linked Versus Direct Attachment. *J. Phys. Chem. C* **2011**, ACS Just Accepted-ACS Just Accepted.
32. Hines, D. A.; Kamat, P. V., Quantum Dot Surface Chemistry: Ligand Effects and Electron Transfer Reactions. *J. Phys. Chem. C* **2013,** *117*, 14418.
33. Anderson, N. A.; Lian, T., Ultrafast Electron Transfer at the Molecule-Semiconductor Nanoparticle Interface. *Ann. Rev. Phys. Chem.* **2005,** *56*, 491-519.
34. Peterson, M. D.; Cass, L. C.; Harris, R. D.; Edme, K.; Sung, K.; Weiss, E. A., The Role of Ligands in Determining the Exciton Relaxation Dynamics in Semiconductor Quantum Dots. *Annu. Rev. Phys. Chem* **2014,** *65*, 317-339.
35. Talapin, D. V.; Murray, C. B., PbSe Nanocrystal Solids for n- and p-Channel Thin Film Field-Effect Transistors. *Science* **2005,** *310*, 86-89.
36. Kovalenko, M. V.; Scheele, M.; Talapin, D. V., Colloidal Nanocrystals with Molecular Metal Chalcogenide Surface Ligands. *Science* **2009,** *324*, 1417-1420.
37. Kovalenko, M. V.; Bodnarchuk, M. I.; Zaumseil, J.; Lee, J.-S.; Talapin, D. V., Expanding the Chemical Versatility of Colloidal Nanocrystals Capped with Molecular Metal Chalcogenide Ligands. *J. Am. Chem. Soc.* **2010,** *132*, 10085-10092.
38. Frederick, M. T.; Amin, V. A.; Cass, L. C.; Weiss, E. A., A Molecule to Detect and Perturb the Confinement of Charge Carriers in Quantum Dots. *Nano Lett.* **2011,** *11*, 5455-5460.
39. Dong, A.; Ye, X.; Chen, J.; Kang, Y.; Gordon, T.; Kikkawa, J. M.; Murray, C. B., A Generalized Ligand-Exchange Strategy Enabling Sequential Surface Functionalization of Colloidal Nanocrystals. *J. Am. Chem. Soc.* **2011,** *133*, 998-1006.
40. Nag, A.; Kovalenko, M. V.; Lee, J. S.; Liu, W.; Spokoyny, B.; Talapin, D. V., Metal-Free Inorganic Ligands for Colloidal Nanocrystals: S2-, HS-, Se2-, HSe-, Te2-, HTe-, TeS3(2-), OH-, and NH2- as Surface Ligands. *J. Am. Chem. Soc.* **2011,** *133*, 10612-10620.

41. Caldwell, M. A.; Albers, A. E.; Levy, S. C.; Pick, T. E.; Cohen, B. E.; Helms, B. A.; Milliron, D. J., Driving Oxygen Coordinated Ligand Exchange at Nanocrystal Surfaces using Trialkylsilylated Chalcogenides. *Chem. Commun.* **2011,** *47*, 556-558.
42. Anderson, N. C.; Owen, J. S., Soluble, Chloride-Terminated CdSe Nanocrystals: Ligand Exchange Monitored by 1 H and 31 P NMR Spectroscopy. *Chem. Mater.* **2013,** *25*, 69-76.
43. Fafarman, A. T.; Koh, W.-K.; Diroll, B. T.; Kim, D. K.; Ko, D.-K.; Oh, S. J.; Ye, X.; Doan-Nguyen, V.; Crump, M. R.; Reifsnyder, D. C., et al., Thiocyanate-Capped Nanocrystal Colloids: Vibrational Reporter of Surface Chemistry and Solution-Based Route to Enhanced Coupling in Nanocrystal Solids. *J. Am. Chem. Soc.* **2011,** *133*, 15753-15761.
44. Rosen, E. L.; Buonsanti, R.; Llordes, A.; Sawvel, A. M.; Milliron, D. J.; Helms, B. A., Exceptionally Mild Reactive Stripping of Native Ligands from Nanocrystal Surfaces by Using Meerwein's Salt. *Angew. Chem. Int. Ed.* **2012,** *51*, 684-689.
45. Zhang, H.; Hu, B.; Sun, L.; Hovden, R.; Wise, F. W.; Muller, D. A.; Robinson, R. D., Surfactant Ligand Removal and Rational Fabrication of Inorganically Connected Quantum Dots. *Nano Lett.* **2011,** *11*, 5356-5361.
46. Beard, M. C.; Midgett, A. G.; Law, M.; Semonin, O. E.; Ellingson, R. J.; Nozik, A. J., Variations in the Quantum Efficiency of Multiple Exciton Generation for a Series of Chemically Treated PbSe Nanocrystal Films. *Nano Lett.* **2009,** *9*, 836-845.
47. Zanella, M.; Maserati, L.; Pernia Leal, M.; Prato, M.; Lavieville, R.; Povia, M.; Krahne, R.; Manna, L., Atomic Ligand Passivation of Colloidal Nanocrystal Films via their Reaction with Propyltrichlorosilane. *Chem. Mater.* **2013,** *25*, 1423-1429.
48. Buckley, J. J.; Couderc, E.; Greaney, M. J.; Munteanu, J.; Riche, C. T.; Bradforth, S. E.; Brutchey, R. L., Chalcogenol Ligand Toolbox for CdSe Nanocrystals and Their Influence on Exciton Relaxation Pathways. *ACS Nano* **2014,** *8*, 2512-2521.
49. Webber, D. H.; Brutchey, R. L., Ligand Exchange on Colloidal CdSe Nanocrystals using Thermally Labile tert-Butylthiol for Improved Photocurrent in Nanocrystal Films. *J. Am. Chem. Soc.* **2012,** *134*, 1085-1092.
50. Nag, A.; Chung, D. S.; Dolzhnikov, D. S.; Dimitrijevic, N. M.; Chattopadhyay, S.; Shibata, T.; Talapin, D. V., Effect of Metal Ions on Photoluminescence, Charge Transport, Magnetic and Catalytic Properties of All-Inorganic Colloidal Nanocrystals and Nanocrystal Solids. *J. Am. Chem. Soc.* **2012,** *134*, 13604-13615.
51. Megerle, U.; Pugliesi, I.; Schriever, C.; Sailer, C. F.; Riedle, E., Sub-50 fs broadband absorption spectroscopy with tunable excitation: putting the analysis of ultrafast molecular dynamics on solid ground. *Appl. Phys. B* **2009,** *96*, 215-231.
52. Yu, W. W.; Qu, L.; Guo, W.; Peng, X., Experimental Determination of the Extinction Coefficient of CdTe, CdSe, and CdS Nanocrystals. *Chem. Mater.* **2003,** *15*, 2854-2860.
53. Oron, D.; Kazes, M.; Banin, U., Multiexcitons in Type-II Colloidal Semiconductor Quantum Dots. *Phys. Rev. B* **2007,** *75*.
54. Kim, S.; Fisher, B.; Eisler, H.-J.; Bawendi, M., Type-II Quantum Dots: CdTe/CdSe(Core/Shell) and CdSe/ZnTe(Core/Shell) Heterostructures. *J. Am. Chem. Soc.* **2003,** *125*, 11466-11467.
55. Brown, K. A.; Wilker, M. B.; Boehm, M.; Dukovic, G.; King, P. W., Characterization of Photochemical Processes for H2 Production by CdS Nanorod-[FeFe] Hydrogenase Complexes. *J. Am. Chem. Soc.* **2012,** *134*, 5627-5636.
56. Tseng, H.-W.; Wilker, M. B.; Damrauer, N. H.; Dukovic, G., Charge Transfer Dynamics Between Photoexcited CdS Nanorods and Mononuclear Ru Water-Oxidation Catalysts. *J. Am. Chem. Soc.* **2013,** *135*, 3383-3386.

57. Wilker, M. B.; Shinopoulos, K. E.; Brown, K. A.; Mulder, D. W.; King, P. W.; Dukovic, G., Electron Transfer Kinetics in CdS Nanorod-[FeFe]-Hydrogenase Complexes and Implications for Photochemical H2 Generation. *J. Am. Chem. Soc.* **2014,** *136*, 4316-4324.
58. McGuire, J. A.; Joo, J.; Pietryga, J. M.; Schaller, R. D.; Klimov, V. I., New Aspects of Carrier Multiplication in Semiconductor Nanocrystals. *Acc. Chem. Res.* **2008,** *41*, 1810-1819.
59. Beard, M. C.; Ellingson, R. J., Multiple exciton generation in semiconductor nanocrystals: Toward efficient solar energy conversion. *Laser Photon Rev.* **2008,** *2*, 377-399.
60. Beard, M. C., Multiple Exciton Generation in Semiconductor Quantum Dots. *J. Phys. Chem. Lett.* **2011,** *2*, 1282-1288.
61. Nozik, A. J., Multiple exciton generation in semiconductor quantum dots. *Chem. Phys. Lett.* **2008,** *457*, 3-11.
62. Klimov, V. I., Quantization of Multiparticle Auger Rates in Semiconductor Quantum Dots. *Science* **2000,** *287*, 1011-1013.
63. Saari, J. I.; Dias, E. A.; Reifsnyder, D.; Krause, M. M.; Walsh, B. R.; Murray, C. B.; Kambhampati, P., Ultrafast Electron Trapping at the Surface of Semiconductor Nanocrystals: Excitonic and Biexcitonic Processes. *J. Phys. Chem. B* **2013,** *117*, 4412-4421.
64. Knowles, K. E.; McArthur, E. A.; Weiss, E. A., A Multi-Timescale Map of Radiative and Nonradiative Decay Pathways for Excitons in CdSe Quantum Dots. *ACS Nano* **2011,** *5*, 2026-2035.
65. Trinh, M. T.; Sfeir, M. Y.; Choi, J. J.; Owen, J. S.; Zhu, X., A Hot Electron-Hole Pair Breaks the Symmetry of a Semiconductor Quantum Dot. *Nano Lett.* **2013,** *13*, 6091-6097.
66. Sewall, S. L.; Cooney, R. R.; Anderson, K. E. H.; Dias, E. A.; Kambhampati, P., State-to-state exciton dynamics in semiconductor quantum dots. *Phys. Rev. B* **2006,** *74*, 235328-235328.
67. Kambhampati, P., Hot Exciton Relaxation Dynamics in Semiconductor Quantum Dots: Radiationless Transitions on the Nanoscale. *J. Phys. Chem. C* **2011,** *115*, 22089-22109.
68. Kambhampati, P., Unraveling the Structure and Dynamics of Excitons in Semiconductor Quantum Dots. *Acc. Chem. Res.* **2011,** *44*, 1-13.
69. Kovalenko, S. A.; Ernsting, N. P.; Ruthmann, J., Femtosecond hole-burning spectroscopy of the dye DCM in solution: the transition from the locally excited to a charge-transfer state. *Chem. Phys. Lett.* **1996,** *258*, 445 - 454.
70. Kovalenko, S.; Dobryakov, A.; Ruthmann, J.; Ernsting, N., Femtosecond spectroscopy of condensed phases with chirped supercontinuum probing. *Phys. Rev. A* **1999,** *59*, 2369-2384.
71. Lorenc, M.; Ziolek, M.; Naskrecki, R.; Karolczak, J.; Kubicki, J.; Maciejewski, A., Artifacts in femtosecond transient absorption spectroscopy. *Appl. Phys. B* **2002,** *74*, 19-27.
72. Schooss, D.; Mews, A.; Eychmuller, A.; Weller, H., Quantum-Dot Quantum Well CdS/HgS/CdS: Theory and Experiment. *Phys. Rev. B* **1994,** *49*, 17072-17078.
73. Dabbousi, B. O.; Mikulec, F. V.; Heine, J. R.; Mattoussi, H.; Ober, R.; Jensen, K. F.; Bawendi, M. G., (CdSe)ZnS Core-Shell Quantum Dots: Synthesis and Characterization of a Size Series of Highly Luminescent Nanocrystallites. *J. Phys. Chem. B* **1997,** *101*, 9463-9475.
74. Haus, J. W.; Zhou, H. S.; Homma, I.; Komiyama, H., Quantum Confinement in Semiconductor Heterostructure Nanometer-Size Particles. *Phys. Rev. B* **1993,** *47*, 1359-1365.
75. Tyrrell, E. J.; Smith, J. M., Effective Mass Modeling of Excitons in Type-II Quantum Dot Heterostructures. *Phys. Rev. B* **2011,** *84*, 165328.
76. Newhouse, P. F.; McGill, K. C., Schrödinger Equation Solutions That Lead to the Solution for the Hydrogen Atom. *J. Chem. Ed.* **2004,** *81*, 424-426.
77. Flugge, S., *Practical Quantum Mechanics*. Springer: Berlin, 1974.
78. BenDaniel, D. J.; Duke, C. B., Space-Charge Effects on Electron Tunneling. *Phys. Rev.* **1966,** *152*, 683 - 692.

79. Brus, L. E., A Simple Model for the Ionization Potential, Electron Affinity, and Aqueous Redox Potentials of Small Semiconductor Crystallites. *J. Chem. Phys.* **1983,** *79*, 5566-5571.
80. Brovelli, S.; Schaller, R. D.; Crooker, S. A.; García-Santamaría, F.; Chen, Y.; Viswanatha, R.; Hollingsworth, J. A.; Htoon, H.; Klimov, V. I., Nano-Engineered Electron-Hole Exchange Interaction Controls Exciton Dynamics in Core-Shell Semiconductor Nanocrystals. *Nat. Commun.* **2011,** *2*, 280.
81. Tyagi, P.; Cooney, R. R.; Sewall, S. L.; Sagar, D. M.; Saari, J. I.; Kambhampati, P., Controlling piezoelectric response in semiconductor quantum dots via impulsive charge localization. *Nano Lett.* **2010,** *10*, 3062-3067.
82. Piryatinski, A.; Ivanov, S. A.; Tretiak, S.; Klimov, V. I., Effect of Quantum and Dielectric Confinement on the Exciton − Exciton Interaction Energy in Type II Core / Shell Semiconductor Nanocrystals. *Nano Lett.* **2007,** *7*, 108-115.
83. Burda, C.; Chen, X.; Narayanan, R.; El-Sayed, M. A., Chemistry and Properties of Nanocrystals of Different Shapes. *Chem. Rev.* **2005,** *105*, 1025-1102.
84. Bawendi, M. G.; Steigerwald, M. L.; Brus, L. E., The Quantum-Mechanics of Larger Semiconductor Clusters (Quantum Dots). *Annu. Rev. Phys. Chem.* **1990,** *41*, 477-496.
85. Cozzoli, P. D.; Pellegrino, T.; Manna, L., Synthesis, Properties and Perspectives of Hybrid Nanocrystal Structures. *Chem. Soc. Rev.* **2006,** *35*, 1195-1208.
86. Kovalenko, M. V.; Bodnarchuk, M. I.; Talapin, D. V., Nanocrystal Superlattices with Thermally Degradable Hybrid Inorganic-Organic Capping Ligands. *J. Am. Chem. Soc.* **2010,** *132*, 15124-15126.
87. Chung, D. S.; Lee, J.-S.; Huang, J.; Nag, A.; Ithurria, S.; Talapin, D. V., Low Voltage, Hysteresis Free, and High Mobility Transistors from All-Inorganic Colloidal Nanocrystals. *Nano Lett.* **2012,** *12*, 1813-1820.
88. Ip, A. H.; Thon, S. M.; Hoogland, S.; Voznyy, O.; Zhitomirsky, D.; Debnath, R.; Levina, L.; Rollny, L. R.; Carey, G. H.; Fischer, A., et al., Hybrid Passivated Colloidal Quantum Dot Solids. *Nat. Nanotechnol.* **2012,** *7*, 577-582.
89. Gao, Y.; Aerts, M.; Sandeep, C. S. S.; Talgorn, E.; Savenije, T. J.; Kinge, S.; Siebbeles, L. D. A.; Houtepen, A. J., Photoconductivity of PbSe Quantum-Dot Solids: Dependence on Ligand Anchor Group and Length. *ACS Nano* **2012,** *6*, 9606-9614.
90. Niu, G.; Wang, L.; Gao, R.; Li, W.; Guo, X.; Dong, H.; Qiu, Y., Inorganic Halogen Ligands in Quantum Dots: I-, Br-, Cl- and Film Fabrication Through Electrophoretic Deposition. *Phys. Chem. Chem. Phys.* **2013,** *15*, 19595-19600.
91. Liu, W.; Lee, J.-S.; Talapin, D. V., III-V Nanocrystals Capped with Molecular Metal Chalcogenide Ligands: High Electron Mobility and Ambipolar Photoresponse. *J. Am. Chem. Soc.* **2013,** *135*, 1349-1357.
92. Dong, A.; Jiao, Y.; Milliron, D. J., Electronically Coupled Nanocrystal Super lattice Films by in Situ Ligand Exchange at the Liquid-Air Interface. *ACS Nano* **2013,** *7*, 10978-10984.
93. Liu, F.; Zhu, J.; Wei, J.; Li, Y.; Hu, L.; Huang, Y.; Takuya, O.; Shen, Q.; Toyoda, T.; Zhang, B., et al., Ex Situ CdSe Quantum Dot-Sensitized Solar Cells Employing Inorganic Ligand Exchange To Boost Efficiency. *J. Phys. Chem. C* **2014,** *118*, 214-222.
94. Tang, J.; Kemp, K. W.; Hoogland, S.; Jeong, K. S.; Liu, H.; Levina, L.; Furukawa, M.; Wang, X.; Debnath, R.; Cha, D., et al., Colloidal-Quantum-Dot Photovoltaics using Atomic-Ligand Passivation. *Nat. Mater.* **2011,** *10*, 765-771.
95. Lee, J.-S.; Kovalenko, M. V.; Huang, J.; Chung, D. S.; Talapin, D. V., Band-Like Transport, High Electron Mobility and High Photoconductivity in All-Inorganic Nanocrystal Arrays. *Nat. Nanotechnol.* **2011,** *6*, 348-352.

96. Liu, Y.; Gibbs, M.; Puthussery, J.; Gaik, S.; Ihly, R.; Hillhouse, H. W.; Law, M., Dependence of Carrier Mobility on Nanocrystal Size and Ligand Length in PbSe Nanocrystal Solids. *Nano Lett.* **2010,** *10*, 1960-1969.
97. Vanmaekelbergh, D.; Liljeroth, P., Electron-Conducting Quantum Dot Solids: Novel Materials Based on Colloidal Semiconductor Nanocrystals. *Chem. Soc. Rev.* **2005,** *34*, 299-312.
98. Choi, J. H.; Fafarman, A. T.; Oh, S. J.; Ko, D. K.; Kim, D. K.; Diroll, B. T.; Muramoto, S.; Gillen, J. G.; Murray, C. B.; Kagan, C. R., Bandlike Transport in Strongly Coupled and Doped Quantum Dot Solids: A Route to High-PerformanceThin-Film Electronics. *Nano Lett.* **2012,** *12*, 2631-2638.
99. Talgorn, E.; Gao, Y.; Aerts, M.; Kunneman, L. T.; Schins, J. M.; Savenije, T. J.; van Huis, M. A.; van der Zant, H. S. J.; Houtepen, A. J.; Siebbeles, L. D. A., Unity Quantum Yield of Photogenerated Charges and Band-Like Transport in Quantum-Dot Solids. *Nat. Nanotechnol.* **2011,** *6*, 733-739.
100. Yun, H. J.; Paik, T.; Edley, M. E.; Baxter, J. B.; Murray, C. B., Enhanced Charge Transfer Kinetics of CdSe Quantum Dot-Sensitized Solar Cell by Inorganic Ligand Exchange Treatments. *Appl. Mater. Interfaces* **2014,** *6*, 3721-3728.
101. Esch, V.; Fluegel, B.; Khitrova, G.; Gibbs, H. M.; Jiajin, X.; Kang, K.; Koch, S. W.; Liu, L. C.; Risbud, S. H.; Peyghambarian, N., State Filling, Coulomb, and Trapping Effects in the Optical Nonlinearity of CdTe Quantum Dots in Glass. *Phys. Rev. B* **1990,** *42*, 7450-7453.
102. Donega, C. d. M.; Koole, R., Size Dependence of the Spontaneous Emission Rate and Absorption Cross Section of CdSe and CdTe Quantum Dots. *J. Phys. Chem. C* **2009,** *113*, 6511-6520.
103. Kamal, J. S.; Omari, A.; Van Hoecke, K.; Zhao, Q.; Vantomme, A.; Vanhaecke, F.; Capek, R. K.; Hens, Z., Size-Dependent Optical Properties of Zinc Blende Cadmium Telluride Quantum Dots. *J. Phys. Chem. C* **2012,** *116*, 5049-5054.
104. Guyot-Sionnest, P.; Lhuillier, E.; Liu, H., A Mirage Study of CdSe Colloidal Quantum Dot Films, Urbach Tail, and Surface States. *J. Chem. Phys.* **2012,** *137*, 154704.
105. Leatherdale, C.; Bawendi, M., Observation of Solvatochromism in CdSe Colloidal Quantum Dots. *Phys. Rev. B* **2001,** *63*, 165315.
106. Fritzinger, B.; Capek, R. K.; Lambert, K.; Martins, J. C.; Hens, Z., Utilizing Self-Exchange to Address the Binding of Carboxylic Acid Ligands to CdSe Quantum Dots. *J. Am. Chem. Soc.* **2010,** *132*, 10195-10201.
107. Morris-Cohen, A. J.; Frederick, M. T.; Lilly, G. D.; McArthur, E. A.; Weiss, E. A., Organic Surfactant-Controlled Composition of the Surfaces of CdSe Quantum Dots. *J. Phys. Chem. Lett.* **2010,** *1*, 1078-1081.
108. Morris-Cohen, A. J.; Donakowski, M. D.; Knowles, K. E.; Weiss, E. A., The Effect of a Common Purification Procedure on the Chemical Composition of the Surfaces of CdSe Quantum Dots Synthesized with Trioctylphosphine Oxide. *J. Phys. Chem. C* **2010,** *114*, 897-906.
109. Taylor, J.; Kippeny, T.; Rosenthal, S. J., Surface Stoichiometry of CdSe Nanocrystals Determined by Rutherford Backscattering Spectroscopy. *J. Clust. Sci.* **2002,** *12*, 571-582.
110. Li, J. J.; Wang, Y. A.; Guo, W.; Keay, J. C.; Mishima, T. D.; Johnson, M. B.; Peng, X., Large-Scale Synthesis of Nearly Monodisperse CdSe/CdS Core/Shell Nanocrystals Using Air-Stable Reagents via Successive Ion Layer Adsorption and Reaction. *J. Am. Chem. Soc.* **2003,** *125*, 12567-12575.
111. Chuang, C.-H.; Lo, S. S.; Scholes, G. D.; Burda, C., Charge Separation and Recombination in CdTe/CdSe Core/Shell Nanocrystals as a Function of Shell Coverage: Probing the Onset of the Quasi Type-II Regime. *J. Phys. Chem. Lett.* **2010,** *1*, 2530-2535.
112. Chang, K.; Xia, J.-B., Spatially Separated Excitons in Quantum-Dot Quantum Well Structures. *Phys. Rev. B* **1998,** *57*, 9780-9786.

113. Dorfs, D.; Henschel, H.; Kolny, J.; Eychmüller, A., Multilayered Nanoheterostructures: Theory and Experiment. *J. Phys. Chem. B* **2004,** *108*, 1578-1583.
114. Early, K. T.; Nesbitt, D. J., Size-Dependent Photoionization in Single CdSe/ZnS Nanocrystals. *Nano Lett.* **2013,** *13*, 4844-4849.
115. Wu, K.; Song, N.; Liu, Z.; Zhu, H.; Rodríguez-Córdoba, W.; Lian, T., Interfacial Charge Separation and Recombination in InP and Quasi-Type II InP/CdS Core/Shell Quantum Dot-Molecular Acceptor Complexes. *J. Phys. Chem. A* **2013,** *117*, 7561-7570.
116. Zhu, H.; Song, N.; Rodríguez-Córdoba, W.; Lian, T., Wave Function Engineering for Efficient Extraction of up to Nineteen Electrons from one CdSe/CdS Quasi-Type II Quantum Dot. *J. Am. Chem. Soc.* **2012,** *134*, 4250-4257.
117. Jin, S.; Zhang, J.; Schaller, R. D.; Rajh, T.; Wiederrecht, G. P., Ultrafast Charge Separation from Highly Reductive ZnTe/CdSe Type II Quantum Dots. *J. Phys. Chem. Lett.* **2012,** *3*, 2052-2058.
118. He, J.; Zhong, H.; Scholes, G. D., Electron-Hole Overlap Dictates the Hole Spin Relaxation Rate in Nanocrystal Heterostructures. *Phys. Rev. Lett.* **2010,** *105*, 046601.
119. Zhu, H.; Song, N.; Lian, T., Controlling Charge Separation and Recombination Rates in CdSe/ZnS Type I Core - Shell Quantum Dots by Shell Thicknesses. *J. Am. Chem. Soc.* **2010,** *132*, 15038-15045.
120. Xiong, W.; Hickstein, D. D.; Schnitzenbaumer, K. J.; Ellis, J. L.; Palm, B. B.; Keister, K. E.; Ding, C.; Miaja-Avila, L.; Dukovic, G.; Jimenez, J. L., et al., Photoelectron Spectroscopy of CdSe Nanocrystals in the Gas Phase: A Direct Measure of the Evanescent Electron Wave Function of Quantum Dots. *Nano Lett.* **2013,** *13*, 2924-2930.
121. Madelung, O., *Semiconductors - Basic Data*. 2 ed.; Springer: 1996.
122. Triboulet, R.; Siffert, P., *CdTe and Related Compounds: Physics, Defects, Hetero- and Nano-structures, Crystal Growth, Surfaces and Applications*. Elsevier: 2010.
123. Martienssen, W.; Warlimont, H., *Springer Handbook of Condensed Matter and Materials Data*. Springer: 2005.
124. Madden, C.; Vaughn, M. D.; Díez-Pérez, I.; Brown, K. A.; King, P. W.; Gust, D.; Moore, A. L.; Moore, T. A., Catalytic Turnover of [FeFe]-Hydrogenase Based on Single-Molecule Imaging. *J. Am. Chem. Soc.* **2012,** *134*, 1577-1582.
125. Wei, S.-H.; Zhang, S. B.; Zunger, A., First-Principles Calculation of Band Offsets, Optical Bowings, and Defects in CdS, CdSe, CdTe, and their Alloys. *J. Appl. Phys.* **2000,** *87*, 1304-1311.
126. Pandey, A.; Guyot-Sionnest, P., Slow Electron Cooling in Colloidal Quantum Dots. *Science* **2008,** *322*, 929-932.
127. Nanda, J.; Ivanov, S. A.; Htoon, H.; Bezel, I.; Piryatinski, A.; Tretiak, S.; Klimov, V. I., Absorption Cross Sections and Auger Recombination Lifetimes in Inverted Core-Shell Nanocrystals: Implications for Lasing Performance. *J. Appl. Phys.* **2006,** *99*, 034309.
128. García-Santamaría, F.; Chen, Y.; Vela, J.; Schaller, R. D.; Hollingsworth, J. A.; Klimov, V. I., Suppressed Auger Recombination in "Giant" Nanocrystals Boosts Optical Gain Performance. *Nano Lett.* **2009,** *9*, 3482-3488.
129. Eshet, H.; Grunwald, M.; Rabani, E., The Electronic Structure of CdSe/CdS Core/Shell Seeded Nanorods: Type-I or Quasi-Type-II? *Nano Lett.* **2013,** *13*, 5880-5855.
130. Foos, E. E., The Complex Interaction of Spectroscopic Shifts and Electronic Properties in Semiconductor Nanocrystal Films. *J. Phys. Chem. Lett.* **2013,** *4*, 625-632.
131. Williams, K. J.; Tisdale, W. A.; Leschkies, K. S.; Haugstad, G.; Norris, D. J.; Aydil, E. S.; Zhu, X. Y., Strong Electronic Coupling in Two-Dimensional Assemblies of Colloidal PbSe Quantum Dots. *ACS Nano* **2009,** *3*, 1532-1538.
132. Bang, J. H.; Kamat, P. V., CdSe Quantum Dot-Fullerene Hybrid Nanocomposite for Solar Energy Conversion: Electron Transfer and Photoelectrochemistry. *ACS Nano* **2011,** *5*, 9421-9427.

133. Robel, I.; Subramanian, V.; Kuno, M.; Kamat, P. V., Quantum Dot Solar Cells. Harvesting Light Energy with CdSe Nanocrystals Molecularly Linked to Mesoscopic TiO2 Films. *J. Am. Chem. Soc.* **2006,** *128*, 2385-2393.
134. Alivisatos, A. P., Perspectives on the Physical Chemistry of Semiconductor Nanocrystals. *J. Phys. Chem.* **1996,** *100*, 13226-13239.
135. Crisp, R. W.; Schrauben, J. N.; Beard, M. C.; Luther, J. M.; Johnson, J. C., Coherent Exciton Delocalization in Strongly Coupled Quantum Dot Arrays. *Nano Lett.* **2013,** *13*, 4862-4869.
136. Schnitzenbaumer, K. J.; Dukovic, G., Chalcogenide-Ligand Passivated CdTe Quantum Dots Can Be Treated As Core/Shell Semiconductor Nanostructures. *J. Phys. Chem. C* **2014,** *118*, 28170 - 28178.
137. Klimov, V. I.; McBranch, D. W., Femtosecond 1P-to-1S Electron Relaxation in Strongly Confined Semiconductor Nanocrystals. *Phys. Rev. Lett.* **1998,** *80*, 4028 - 4031.
138. Huang, J.; Huang, Z.; Yang, Y.; Zhu, H.; Lian, T., Multiple Exciton Dissociation in CdSe Quantum Dots by Ultrafast Electron Transfer to Adsorbed Methylene Blue. *J. Am. Chem. Soc.* **2010,** *132*, 4858-4864.
139. Sykora, M.; Petruska, M. A.; Alstrum-Acevedo, J.; Bezel, I.; Meyer, T. J.; Klimov, V. I., Photoinduced Charge Transfer between CdSe Nanocrystal Quantum Dots and Ru-Polypyridine Complexes. *J. Am. Chem. Soc.* **2006,** *128*, 9984-9985.
140. Huang, J.; Huang, Z.; Jin, S.; Lian, T., Exciton Dissociation in CdSe Quantum Dots by Hole Transfer to Phenothiazine. *J. Phys. Chem. C* **2008,** *112*, 19734-19738.
141. Burda, C.; Link, S.; Green, T. C.; El-Sayed, M. A., New Transient Absorption Observed in the Spectrum of Colloidal CdSe Nanoparticles Pumped with High-Power Femtosecond Pulses. *J. Phys. Chem. B.* **1999,** *103*, 10775-10780.
142. McArthur, E. A.; Morris-Cohen, A. J.; Knowles, K. E.; Weiss, E. A., Charge Carrier Resolved Relaxation of the First Excitonic State in CdSe Quantum Dots Probed with Near-Infrared Transient Absorption Spectroscopy. *J. Phys. Chem. B* **2010,** *114*, 14514-14520.
143. Sewall, S. L.; Cooney, R. R.; Anderson, K. E. H.; Dias, E. A.; Sagar, D. M.; Kambhampati, P., State-resolved studies of biexcitons and surface trapping dynamics in semiconductor quantum dots. *J. Chem. Phys.* **2008,** *129*, 084701.
144. Lakowicz, J. R., *Principles of Fluorescence Spectroscopy*. Springer: New York, NY, 2006.
145. Baker, D. R.; Kamat, P. V., Tuning the Emission of CdSe Quantum Dots by Controlled Trap Enhancement. *Langmuir* **2010,** *26*, 11272-11276.
146. Cooney, R.; Sewall, S.; Dias, E.; Sagar, D.; Anderson, K.; Kambhampati, P., Unified picture of electron and hole relaxation pathways in semiconductor quantum dots. *Phys. Rev. B* **2007,** *75*, 245311-245311.
147. Guyot-Sionnest, P.; Shim, M.; Matranga, C.; Hines, M., Intraband relaxation in CdSe quantum dots. *Phys. Rev. B* **1999,** *60*, 2181-2184.
148. Klimov, V.; Mikhailovsky, A.; McBranch, D.; Leatherdale, C.; Bawendi, M., Mechanisms for intraband energy relaxation in semiconductor quantum dots: The role of electron-hole interactions. *Phys. Rev. B* **2000,** *61*, R13349-R13352.
149. Chuang, C.-H.; Chen, X.; Burda, C., Femtosecond time-resolved hot carrier energy distributions of photoexcited semiconductor quantum dots. *Ann. Phys.* **2013,** *525*, 43-48.
150. Kilina, S.; Ivanov, S.; Tretiak, S., Effect of Surface Ligands on Optical and Electronic Spectra of Semiconductor Nanoclusters. *J. Am. Chem. Soc.* **2009,** *131*, 7717-7726.
151. Kilina, S.; Velizhanin, K. A.; Ivanov, S.; Prezhdo, O. V.; Tretiak, S., Surface Ligands Increase Photoexcitation Relaxation Rates in CdSe Quantum Dots. *ACS Nano* **2012,** *6*, 6515-6524.

152. Rainò, G.; Moreels, I.; Hassinen, A.; Stöferle, T.; Hens, Z.; Mahrt, R. F., Exciton Dynamics within the Band-Edge Manifold States: The Onset of an Acoustic Phonon Bottleneck. *Nano Lett.* **2012,** *12*, 5224-5229.
153. Shabaev, A.; Efros, A. L.; Nozik, A. J., Multiexciton Generation by a Single Photon in Nanocrystals. *Nano Lett.* **2006,** *6*, 2856-2863.
154. Sadhu, S.; Tachiya, M.; Patra, A., A Stochastic Model for Energy Transfer from CdS Quantum Dots/Rods (Donors) to Nile Red Dye (Acceptors). *J. Phys. Chem. C* **2009,** *113*, 19488-19492.
155. Sadhu, S.; Patra, A., Relaxation Dynamics of Anisotropic Shaped CdS Nanoparticles. *J. Phys. Chem. C* **2011,** *115*, 16867-16872.
156. Jiang, Z.-J.; Kelley, D. F., Hot and Relaxed Electron Transfer from the CdSe Core and Core/Shell Nanorods. *J. Phys. Chem. C* **2011,** *115*, 4594-4602.
157. Bang, J. H.; Kamat, P. V., Quantum Dot Sensitized Solar Cells. A Tale of Two Semiconductor Nanocrystals: CdSe and CdTe. *ACS Nano* **2009,** *3*, 1467-1476.
158. Yan, Y.; Chen, G.; Patten, P. G. V., Ultrafast Exciton Dynamics in CdTe Nanocrystals and Core / Shell CdTe / CdS Nanocrystals. *J. Phys. Chem. C* **2011,** *115*, 22717-22728.
159. Kobayashi, Y.; Chuang, C.-H.; Burda, C.; Scholes, G. D., Exploring Ultrafast Electronic Processes of Quasi-Type II Nanocrystals by Two-Dimensional Electronic Spectroscopy. *J. Phys. Chem. C* **2014,** *118*, 16255-16263.
160. Kaniyankandy, S.; Rawalekar, S.; Verma, S.; Palit, D. K.; Ghosh, H. N., Charge carrier dynamics in thiol capped CdTe quantum dots. *Phys. Chem. Chem. Phys.* **2010,** *12*, 4210-4216.
161. Groeneveld, E.; Delerue, C.; Allan, G.; Niquet, Y.; de Mello Donegá, C., Size Dependence of the Exciton Transitions in Colloidal CdTe Quantum Dots. *J. Phys. Chem. C* **2012,** *116*, 23160-23167.
162. Chuang, C.-H.; Doane, T.; Lo, S. S.; Scholes, G. D.; Burda, C., Measuring Electron and Hole Transfer in Core/Shell Nanoheterostructures. *ACS Nano* **2011,** *5*, 6016-6024.
163. Hewa-Kasakarage, N.; El-Khoury, P. Z.; Tarnovsky, A. N.; Kirsanova, M.; Nemitz, I.; Nemchinov, A.; Zamkov, M., Ultrafast Carrier Dynamics in Type II ZnSe/CdS/ZnSe Nanobarbells. *ACS Nano* **2010,** *4*, 1837-1844.
164. Klimov, V. I., Optical Nonlinearities and Ultrafast Carrier Dynamics in Semiconductor Nanocrystals. *J. Phys. Chem. B* **2000,** *104*, 6112-6123.
165. Klimov, V.; McBranch, D.; Leatherdale, C.; Bawendi, M., Electron and hole relaxation pathways in semiconductor quantum dots. *Phys. Rev. B* **1999,** *60*, 13740-13749.
166. Hewa-Kasakarage, N.; Kirsanova, M.; Nemchinov, A.; Schmall, N.; El-Khoury, P. Z.; Tarnovsky, A. N.; Zamkov, M., Radiative Recombination of Spatially Extended Excitons in (ZnSe/CdS)/CdS Heterostructured Nanorods. *J. Am. Chem. Soc.* **2009,** *131*, 1328-1334.
167. Bang, J. H.; Kamat, P. V., Solar Cells by Design: Photoelectrochemistry of TiO2 Nanorod Arrays Decorated with CdSe. *Adv. Func. Mater.* **2010,** *20*, 1970-1976.
168. Lo, S. S.; Mirkovic, T.; Chuang, C. H.; Burda, C.; Scholes, G. D., Emergent Properties Resulting from Type-II Band Alignment in Semiconductor Nanoheterostructures. *Adv. Mater.* **2011,** *23*, 180-197.
169. Hassan, Y.; Chuang, C.-h.; Kobayashi, Y.; Coombs, N.; Gorantla, S.; Botton, G. A.; Winnik, M. A.; Burda, C.; Scholes, G. D., Synthesis and Optical Properties of Linker-Free TiO2/CdSe Nanorods. *J. Phys. Chem. C* **2014,** *118*, 3347-3358.
170. Empedocles, S. A.; Bawendi, M. G., Quantum-Confined Stark Effect in Single CdSe Nanocrystallite Quantum Dots. *Science* **1997,** *278*, 2114-2117.
171. Sagar, D.; Cooney, R.; Sewall, S.; Dias, E.; Barsan, M.; Butler, I.; Kambhampati, P., Size dependent, state-resolved studies of exciton-phonon couplings in strongly confined semiconductor quantum dots. *Phys. Rev. B* **2008,** *77*, 235321-235321.

172. Kelley, A. M., Electron−Phonon Coupling in CdSe Nanocrystals. *J. Phys. Chem. Lett.* **2010,** *1*, 1296-1300.
173. Klein, M. C.; Hache, F.; Ricard, D.; Flytzanis, C., Size dependence of electron-phonon coupling in semiconductor nanospheres: The case of CdSe. *Phys. Rev. B* **1990,** *42*, 11123-11132.
174. Takagahara, T., Electron-Phonon Interactions and Excitonic Dephasing in Semiconductor Nanocrystals. *Phys. Rev. Lett.* **1993,** *71*, 3577-3580.
175. Groeneveld, E.; Donega, C. D. M., Enhanced Exciton − Phonon Coupling in Colloidal Type-II CdTe-CdSe Heteronanocrystals. *J. Phys. Chem. C* **2012,** *116*, 16240 - 16250.
176. Jonas, D. M.; Bradforth, S. E.; Passino, S. A.; Fleming, G. R., Femtosecond Wavepacket Spectroscopy: Influence of Temperature, Wavelength, and Pulse Duration. *J. Phys. Chem.* **1995,** *99*, 2594-2608.
177. Dworak, L.; Matylitsky, V. V.; Braun, M.; Wachtveitl, J., Coherent Longitudinal-Optical Ground-State Phonon in CdSe Quantum Dots Triggered by Ultrafast Charge Migration. *Phys. Rev. Lett.* **2011,** *107*, 247401-247401.
178. Cho, B.; Peters, W. K.; Hill, R. J.; Courtney, T. L.; Jonas, D. M., Bulklike Hot Carrier Dynamics in Lead Sulfide Quantum Dots. *Nano Lett.* **2010,** *10*, 2498-2505.
179. Schaller, R. D.; Pietryga, J. M.; Goupalov, S. V.; Petruska, M. A.; Ivanov, S. A.; Klimov, V. I., Breaking the Phonon Bottleneck in Semiconductor Nanocrystals via Multiphonon Emission Induced by Intrinsic Nonadiabatic Interactions. *Phys. Rev. Lett.* **2005,** *95*, 196401-196401.
180. Gesuele, F.; Sfeir, M. Y.; Murray, C. B.; Heinz, T. F.; Wong, C. W., Ultrafast Supercontinuum Spectroscopy of Carrier Multiplication and Biexcitonic E ff ects in Excited States of PbS Quantum Dots. *Nano Lett.* **2012,** *12*.
181. Hendry, E.; Koeberg, M.; Wang, F.; Zhang, H.; de Mello Donegá, C.; Vanmaekelbergh, D.; Bonn, M., Direct Observation of Electron-to-Hole Energy Transfer in CdSe Quantum Dots. *Phys. Rev. Lett.* **2006,** *96*, 057408-057408.
182. Miaja-Avila, L.; Tritsch, J. R.; Wolcott, A.; Chan, W. L.; Nelson, C. A.; Zhu, X. Y., Direct Mapping of Hot-Electron Relaxation and Multiplication Dynamics in PbSe Quantum Dots. *Nano Lett.* **2012,** *12*, 1588-1591.
183. Harris, C. B.; Ge, N.; Lingle, R. L.; McNeill, J. D.; Wong, C. M., Femtosecond Dynamics of Electrons on Surfaces and at Interfaces. *Annu. Rev. Phys. Chem.* **1997,** *48*, 711-744.
184. Eppink, A. T. J. B.; Parker, D. H., Velocity map imaging of ions and electrons using electrostatic lenses: Application in photoelectron and photofragment ion imaging of molecular oxygen. *Rev. Sci. Instrum.* **1997,** *68*, 3477-3484.
185. Hickstein, D.; Ranitovic, P.; Witte, S.; Tong, X.-M.; Huismans, Y.; Arpin, P.; Zhou, X.; Keister, K.; Hogle, C.; Zhang, B., et al., Direct Visualization of Laser-Driven Electron Multiple Scattering and Tunneling Distance in Strong-Field Ionization. *Phys. Rev. Lett.* **2012,** *109*, 073004-073004.
186. Zhang, X.; Smith, K. A.; Worsnop, D. R.; Jimenez, J. L.; Jayne, J. T.; Kolb, C. E.; Morris, J.; Davidovits, P., Numerical Characterization of Particle Beam Collimation: Part II Integrated Aerodynamic-Lens–Nozzle System. *Aerosol Sci. Technol.* **2004,** *38*, 619-638.
187. Wilson, K. R.; Zou, S.; Shu, J.; Ruhl, E.; Leone, S. R.; Schatz, G. C.; Ahmed, M., Size-Dependent Angular Distributions of Low-Energy Photoelectrons Emitted from NaCl Nanoparticles. *Nano Lett.* **2007,** *7*, 2014-2019.
188. Zherebtsov, S.; Fennel, T.; Plenge, J.; Antonsson, E.; Znakovskaya, I.; Wirth, A.; Herrwerth, O.; Süßmann, F.; Peltz, C.; Ahmad, I., et al., Controlled near-field enhanced electron acceleration from dielectric nanospheres with intense few-cycle laser fields. *Nature Phys.* **2011,** *7*, 656-662.

189. Liu, P.; Ziemann, P. J.; Kittelson, D. B.; McMurry, P. H., Generating Particle Beams of Controlled Dimensions and Divergence: II. Experimental Evaluation of Particle Motion in Aerodynamic Lenses and Nozzle Expansions. *Aerosol Sci. Technol.* **1995,** *22*, 314-324.
190. Canagaratna, M. R.; Jayne, J. T.; Jimenez, J. L.; Allan, J. D.; Alfarra, M. R.; Zhang, Q.; Onasch, T. B.; Drewnick, F.; Coe, H.; Middlebrook, A., et al., Chemical and Microphysical Characterization of Ambient Aerosols with the Aerodyne Aerosol Mass Spectrometer. *Mass. Spec. Rev.* **2007,** *26*, 185-222.
191. Murphy, D. M., The Design of Single Particle Laser Mass Spectrometers. *Mass. Spec. Rev.* **2007,** *26*, 150-165.
192. Pelton, M.; Smith, G.; Scherer, N. F.; Marcus, R. A., Evidence for a diffusion-controlled mechanism for fluorescence blinking of colloidal quantum dots. *Proc. Nat. Acad. Sci.* **2007,** *104*, 14249-14254.
193. Galland, C.; Ghosh, Y.; Steinbrück, A.; Hollingsworth, J. A.; Htoon, H.; Klimov, V. I., Lifetime blinking in nonblinking nanocrystal quantum dots. *Nat. Comm.* **2012,** *3908*, 1-7.
194. Norris, D.; Bawendi, M., Measurement and assignment of the size-dependent optical spectrum in CdSe quantum dots. *Phys. Rev. B* **1996,** *53*, 16338-16346.
195. Dribinski, V.; Ossadtchi, A.; Mandelshtam, V. A.; Reisler, H., Reconstruction of Abel-transformable images: The Gaussian basis-set expansion Abel transform method. *Rev. Sci. Instrum.* **2002,** *73*, 2634-2642.
196. Neumann, O.; Urban, A. S.; Day, J.; Lal, S.; Nordlander, P.; Halas, N. J., Solar Vapor Generation Enabled by Nanoparticles. *ACS Nano* **2013,** *7*, 42-49.
197. Loss, D.; Divincenzo, D. P., Quantum computation with quantum dots. *Phys. Rev. A* **1998,** *57*, 120-126.
198. Kirschbaum, J.; Hohberger, E. M.; Blick, R. H.; Wegscheider, W.; Bichler, M., Integrating suspended quantum dot circuits for applications in nanomechanics. *Appl. Phys. Lett.* **2002,** *81*, 280-282.
199. Lei, K. W.; West, T.; Zhu, X.-Y., Template-Assembly of Quantum Dot Molecules. *J. Phys. Chem. B* **2013,** *117*, 4582-4586.
200. Frederick, M. T.; Amin, V. A.; Swenson, N. K.; Ho, A. Y.; Weiss, E. A., Control of Exciton Confinement in Quantum Dot-Organic Complexes Through Energetic Alignment of Interfacial Orbitals. *Nano Lett.* **2013,** *13*, 287-292.
201. Sippel, P.; Albrecht, W.; Mitoraj, D.; Eichberger, R.; Hannappel, T.; Vanmaekelbergh, D., Two-Photon Photoemission Study of Competing Auger and Surface-Mediated Relaxation of Hot Electrons in CdSe Quantum Dot Solids. *Nano Lett.* **2013,** *13*, 1655-1661.
202. Henglein, A., Photochemistry of Colloidal Cadmium Sulfide. 2. Effects of Adsorbed Methyl Viologen and of Colloidal Platinum. *J. Phys. Chem. C* **1982,** *86*, 301-305.
203. Spanhel, L.; Haase, M.; Weller, H.; Henglein, A., Photochemistry of Colloidal Semiconductors. 20. Surface Modification and Stability of Strong Luminescing CdS Particles. *J. Am. Chem. Soc.* **1987,** *109*, 5649-5655.
204. Spanhel, L.; Weller, H.; Henglein, A., Photochemistry of Semiconductor Colloids. 22. Electron Injection from Illuminated CdS into Attached TiO2 and ZnO Particles. *J. Am. Chem. Soc.* **1987,** *109*, 6632-6635.
205. Berglund, C. N.; Spicer, W. E., Photoemission Studies of Copper and Silver: Theory. *Phys. Rev.* **1964,** *136*, 1030-1044.
206. Smeenk, C. T. L.; Arissian, L.; Zhou, B.; Mysyrowicz, a.; Villeneuve, D. M.; Staudte, A.; Corkum, P. B., Partitioning of the Linear Photon Momentum in Multiphoton Ionization. *Phys. Rev. Lett.* **2011,** *106*, 193002-193002.

207. Xie, Z.; Markus, T. Z.; Gotesman, G.; Deutsch, Z.; Oron, D.; Naaman, R., How Isolated Are the Electronic States of the Core in Core/Shell Nanopartciles. *ACS Nano* **2011,** *5*, 863-869.
208. Miaja-Avila, L.; Yin, J.; Backus, S.; Saathoff, G.; Aeschlimann, M.; Murnane, M.; Kapteyn, H., Ultrafast studies of electronic processes at surfaces using the laser-assisted photoelectric effect with long-wavelength dressing light. *Phys. Rev. A* **2009,** *79*, 030901-030901.
209. Van de Walle, C. G.; Neugebauer, J., Universal alignment of hydrogen levels in semiconductors, insulators and solutions. *Nature* **2003,** *423*, 626-628.
210. Borchert, H.; Talapin, D. V.; McGinley, C.; Adam, S.; Lobo, A.; de Castro, a. R. B.; Mo□ller, T.; Weller, H., High resolution photoemission study of CdSe and CdSe/ZnS core-shell nanocrystals. *J. Chem. Phys.* **2003,** *119*, 1800-1807.
211. Haight, R., Electron dynamics at surfaces. *Surf. Sci. Rep.* **1995,** *21*, 275-325.
212. Hofer, U.; Shumay, I. L.; Reuß, C.; Thomann, U.; Wallauer, W.; Fauster, T., Time-Resolved Coherent Photoelectron Spectroscopy of Quantized Electronic States on Metal Surfaces. *Science* **1997,** *277*, 1480-1482.
213. Knowles, K. E.; Peterson, M. D.; McPhail, M. R.; Weiss, E. A., Exciton Dissociation within Quantum Dot − Organic Complexes: Mechanisms, Use as a Probe of Interfacial Structure, and Applications. *J. Phys. Chem. C* **2013,** *117*, 10229-10243.
214. Hyun, B.-r.; Bartnik, A. C.; Lee, J.-K.; Imoto, H.; Sun, L.; Choi, J. J.; Chujo, Y.; Hanrath, T.; Ober, C. K.; Wise, F. W., Role of Solvent Dielectric Properties on Charge Transfer from PbS Nanocrystals to Molecules. *Nano Lett.* **2010,** *10*, 318-323.
215. Dworak, L.; Matylitsky, V. V.; Breus, V. V.; Braun, M.; Basché, T.; Wachtveitl, J., Ultrafast Charge Separation at the CdSe/CdS Core/Shell Quantum Dot/Methylviologen Interface: Implications for Nanocrystal Solar Cells. *The Journal of Physical Chemistry C* **2011,** *115*, 3949-3955.
216. Ai, X.; Jin, R.; Ge, C.; Wang, J.; Zou, Y.; Zhou, X.; Xiao, X., Femtosecond investigation of charge carrier dynamics in CdSe nanocluster films. *J. Chem. Phys.* **1997,** *106*, 3387-3392.
217. Hyun, B.-r.; Zhong, Y.-W.; Bartnik, A. C.; Sun, L.; Abrun, H. D.; Wise, F. W.; Goodreau, J. D.; Matthews, J. R.; Leslie, T. M.; Borrelli, N. F., Electron Injection from Colloidal PbS Nanoparticles. *ACS Nano* **2008,** *2*, 2206-2212.
218. Hickstein, D. D.; Dollar, F.; Gaffney, J. A.; Foord, M. E.; Petrov, G. M.; Palm, B. B.; Keister, K. E.; Ellis, J. L.; Ding, C.; Libby, S. B., et al., Observation and Control of Shock Waves in Individual Nanoplasmas. *Phys. Rev. Lett.* **2014,** *112*, 115004-115004.
219. Hickstein, D. D.; Dollar, F.; Ellis, J. L.; Schnitzenbaumer, K. J.; Keister, K. E.; Petrov, G. M.; Ding, C.; Palm, B. B.; Gaffney, J. A.; Foord, M. E., et al., Mapping Nanoscale Absorption of Femtosecond Laser Pulses Using Plasma Explosion Imaging. *ACS Nano* **2014,** *8*, 8810-8818.
220. Matylitsky, V. V.; Dworak, L.; Breus, V. V.; Basché, T.; Wachtveitl, J., Ultrafast Charge Separation in Multiexcited CdSe Quantum Dots Mediated by Adsorbed Electron Acceptors. *J. Am. Chem. Soc.* **2009,** *131*, 2424-2425.
221. Harris, C.; Kamat, P. V., Photocatalysis with CdSe nanoparticles in confined media: mapping charge transfer events in the subpicosecond to second timescales. *ACS Nano* **2009,** *3*, 682-690.
222. Lindstrom, C. D.; Zhu, X.-Y., Photoinduced Electron Transfer at Molecule − Metal Interfaces. *Chem. Rev.* **2006,** *106*, 4281-4300.
223. Kim, H. J.; Hynes, J. T., Solvent Electronic Polarization in Electron-Transfer Processes. *J. Phys. Chem. C* **1990,** *94*, 2136-2140.
224. Kim, H. J.; Hynes, J. T., Equilibrium and nonequilibrium solvation and solute electronic structure . I . Formulation. *J. Chem. Phys.* **1990,** *5194*, 5194-5210.
225. Kim, H. J.; Hynes, J. T., Equilibrium and nonequilibrium solvation and solute electronic structure . II . Strong coupling limit. *J. Chem. Phys.* **1990,** *5211*, 5211-5223.

226. Kim, H. J.; Hynes, J. T., Equilibrium and nonequilibrium solvation and solute electronic structure . III . Quantum theory. *J. Chem. Phys.* **1992,** *5088*, 5088-5110.
227. Hynes, J. T.; Kim, H. J.; Mathis, J. R.; Timoneda, J. J., Solute Electronic Structure and Solvation in Chemical Reactions in Solution. *J. Molec. Liq.* **1993,** *57*, 53-73.
228. Maroncelli, M.; Macinnis, J.; Fleming, G. R., Polar Solvent Dynamics and Electron-Transfer Reactions. *Science* **1989,** *243*.
229. Barbara, P. F.; Walker, G. C.; Smith, T. P., Vibrational Modes and the Dynamic Solvent Effect in Electron and Proton Transfer. *Science* **1992,** *256*, 975 - 981.
230. Bae, S.; Kim, S.; Lee, S.; Choi, W., Dye decolorization test for the activity assessment of visible light photocatalysts: Realities and limitations. *Catalysis Today* **2014,** *224*, 21-28.